W&M ScholarWorks

Dissertations, Theses, and Masters Projects   Theses, Dissertations, & Master Projects

2000

Surface processing by RFI PECVD and RFI PSII

Lingling Wu
College of William & Mary - Arts & Sciences

Follow this and additional works at: https://scholarworks.wm.edu/etd

Part of the Condensed Matter Physics Commons, Materials Science and Engineering Commons, and the Plasma and Beam Physics Commons

INFORMATION TO USERS

This manuscript has been reproduced from the microfilm master. UMI films the text directly from the original or copy submitted. Thus, some thesis and dissertation copies are in typewriter face, while others may be from any type of computer printer.

The quality of this reproduction is dependent upon the quality of the copy submitted. Broken or indistinct print, colored or poor quality illustrations and photographs, print bleedthrough, substandard margins, and improper alignment can adversely affect reproduction.

In the unlikely event that the author did not send UMI a complete manuscript and there are missing pages, these will be noted. Also, if unauthorized copyright material had to be removed, a note will indicate the deletion.

Oversize materials (e.g., maps, drawings, charts) are reproduced by sectioning the original, beginning at the upper left-hand corner and continuing from left to right in equal sections with small overlaps.

Photographs included in the original manuscript have been reproduced xerographically in this copy. Higher quality 6" x 9" black and white photographic prints are available for any photographs or illustrations appearing in this copy for an additional charge. Contact UMI directly to order.

UMI®

SURFACE PROCESSING
BY RFI PECVD AND RFI PSII

A Dissertation

Presented to

The Faculty of the Department of Applied Science

The College of William and Mary in Virginia

In Partial Fulfillment

Of the Requirements for the Degree of

Doctor of Philosophy

by

Lingling Wu

October, 2000

UMI Number: 9999060

Copyright 2001 by
Wu, Lingling

All rights reserved.

UMI®

UMI Microform 9999060
Copyright 2001 by Bell & Howell Information and Learning Company.
All rights reserved. This microform edition is protected against
unauthorized copying under Title 17, United States Code.

APPROVAL SHEET

This dissertation is submitted in partital fulfillment of
the requirements for the degree of

Doctor of Philosophy

_____
Lingling Wu

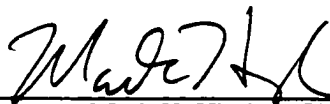Approved, October 2000

_____
Dennis M. Manos, Ph.D., Chair
Department of Applied Science

_____
Roy L. Champion, Ph.D.
Department of Physics

_____
H. Frederick Dylla, Ph.D.
Thomas Jefferson National Accelerator Facility

_____
Mark K. Hinders, Ph.D.
Department of Applied Science

Table of Contents

iv

v

Acknowledgments

I would like to thank Dr. Dennis Manos, for years of guidance and encouragement. I would also like to thank scientists and engineers of the FEL program at Thomas Jefferson National Accelerator Facility (TJNAF), especially Dr. Fred Dylla, Mr. Jock Fugitt and Mr. Richard Nelson, for their kind help with my experiments. Thanks to Dr. Charles Sinclair, Mr. Timothy Siggins, Mr. George Biallas of TJNAF, for their collaboration of FEL injection gun implants.

I wish to thank my committee members for their reading and criticism of this manuscript. They are Dr. Roy Champion, Dr. Fred Dylla, Dr. Mark Hinders, and Dr. Dennis Manos.

I would also like to express my appreciation to those individuals who wrote the many letters of recommendation for me during my job search, including Dr. Fred Dylla, and Dr. Brian Holloway. I am also grateful to Dr. Michael Kelley, who gave me valuable advice on job search and career.

I want to thank Dr. Larry Ludeking of Mission Research Corporation, for providing the code and training in the use of MAGIC.

Thanks to Mr. Richard Moore, formerly of Evans East, now of SUNY Albany, for careful assistance with some of the surface analysis. I am also grateful to Dr. David Cole of Evans East, for his help with SIMS analysis and with the data files.

Thanks to Dr. Hongjun Gao, formerly of Oak Ridge National Laboratory, now of Beijing Laboratory of Vacuum Physics, for performing TEM for us.

I want to thank Richard Proper, for helping setting up the lab and for help with the experiments. I also want to thank Jay Diggs and Amy Wilkerson, for their help, and for the time we spent together talking about wonderful things. Thanks to Dr. Xianmin Tang for the help with OES study. Thanks to Carol Kalil for her help with the AFM. I want to thank Dr. Edward Gillman of TJNAF, who has been a wonderful friend and who has helped me with XPS and AES experiments. I want to thank Casy Apeldoorn and Dave McCay of the TJNAF machine shop, who quickly turned so many of my designs into beautiful apparatus. I also want to thank Philip Adderley and Ralph Afanador of TJNAF, for cleaning large vacuum parts and for their help with vacuum systems. Thanks to Brandt Robertson of Old Dominion University, for performing SEM and surface profilometry measurements for me. I also want to thank Dr. George Loutts of Norfolk State University, for giving me unlimited access to the XRD apparatus. I want to thank Dr. James Terner at Virginia Commonwealth University, for his kind help with Raman measurements.

I want to thank Karen Berquist, for her help with my writing and for being a great friend. Thanks to Cindy Manos, for helping me when I hurt my back and was home alone. Thanks to Kathee, Bernadette, Paula, Dianne, and Sylvia, for taking good care of me. Thanks also to the many graduate students, with whom I have spent the last six years of my life. Thanks to Ingrid and Chris, for being such good friends for so many years.

viii

Finally, I want to express my most sincere appreciation to my family. Thanks to my dear grandmother, who has been watching over me in the heavens. Thanks to my mother, father, and brother, for believing in me and supporting my endeavors. I would especially thank my husband, Xiangyu Huang, who has witnessed me getting each and every degree, for years of understanding, help, and encouragement. Their love and support mean a great deal to me and I could not have done this without them.

List of Tables

x

List of Figures

xii

xiii

xiv

xvii

xviii

Abstract

An RFI plasma enhanced chemical vapor deposition (PECVD) system and a large-scale RF plasma source immersion ion implantation (PSII) system were designed and built to study two forms of 3-D surface processing, PECVD and PSII. Using the RFI PECVD system, Ti-6Al-4V substrates were coated with diamond-like carbon films with excellent tribological and optical properties. As an innovation, variable angle spectroscopic ellipsometry (VASE) was successfully applied for non-destructive, 3-D, large-area tribological coatings quality investigation.

Based on the experience with the RFI PECVD system, a large-scale RFICP source was designed and built for the PSII. Langmuir probe and optical emission spectroscopy studies indicated that the RFI source produced stable, uniform, and clean plasma. MAGIC code was for the first time used to model PSII process, addressing different target geometries and boundaries, materials, plasma parameters, illustrated sheath formation and evolution, field distribution, ion and electron trajectories, ion incident angles, and dose distributions, which are critical for PSII design and understanding.

The RF PSII system was developed into a versatile large-area, uniform, 3-D surface processing apparatus, capable of PSII, PVD, PECVD, and in situ surface cleaning and interface properties modification, for multilayer, multi-step, and high

performance surface engineering. Using the RFI PSII system, for the first time, PSII was studied as a mask-based surface layer conversion technique, for pattern writing by implantation as an alternative to current deposition-based and ink-based direct write technologies. It operates at low substrate temperature, keeps the original surface finish and dimensions, and avoids adhesion problem. A different operating mode of the RF source was discovered to perform biased sputtering of high purity quartz, which turned the RFI PSII system into a novel integrated RF PSII/PVD system for large-area, uniform, nitrogen-doped, and hydrogen-free SiO_2 films deposition at low substrate temperatures. Nitrogen-doped SiO_2 films with excellent optical properties were deposited on semiconductor, metal, and polymer substrates with excellent adhesion. Ellipsometry was used again for non-destructive SiO_2 coatings investigation. FEL test electrodes processed by PSII/PVD showed suppressed field emission. A group of transition metals and an FEL test electrode were also implanted by nitrogen using the PSII mode and analyzed.

SURFACE PROCESSING
BY RFI PECVD AND RFI PSII

Chapter 1

Introduction

1.1 Introduction to Surface Processing by RFI PECVD and RFI PSII

This thesis examines advances in two forms of surface processing. Surface processing has been playing an increasingly important role over the past decades, because of the importance of surface properties for the total performance of the material. In many applications and constructions, failure originates at the surface [1]. The applicability and commercial value of a material can be greatly enhanced by surface treatments. General examples include anti-reflective and anti-scratch coatings for optical components, impact and wear resistant coatings for cutting tools, bearings and gears, lubricating layers for moving mechanical parts, and protective layer for electronics devices. Special applications include surface processing of high voltage stainless steel electrode to suppress field emission and ensure reliable and consistent performance of electron guns, which is crucial for the operation of both the main accelerator ring and for the Free Electron Laser at Thomas Jefferson National Accelerator Facility (TJNAF) [2]. Another example is the oxynitridation of Si

2

substrates by rapid thermal oxidation in N_2O to produce a dielectric layer that significantly retards the boron diffusion, to improve the microelectronic device reliability [3].

High voltage photoelectron guns are used at Thomas Jefferson National Accelerator Facility for electron beam production. The Free Electron Laser at TJNAF is the brightest FEL in the world, with an average power output of 1700 watts, compared to a record of merely 10 watts before the FEL at TJNAF was built. A schematic of the FEL electron injection gun is shown in Fig. 1.1. A highly polished hollow stainless steel structure about 8 in. in diameter is used as the cathode, which supports the molybdenum base holding a GaAs wafer. A pulsed Laser is used to radiate the GaAs wafer for photoelectron generation. The cathode is usually biased to high potentials of up to 500 KV, yielding a field gradient of 3-6 MV/m. The photoelectrons are accelerated by the strong electric field and exit the anode aperture to form an electron beam.

Higher operating voltage is highly desirable for enhancing the photoelectron gun performance. Bunch charge and emittance are two important design parameters for an electron gun. The surface charge per unit area on the GaAs wafer is directly proportional to the electric field applied. For each Laser pulse, a small portion of the GaAs wafer is radiated and a small number of photoelectrons is generated [2]. The charge per bunch requirement for the FEL electron gun is 135 $pC/bunch$. High voltage is also necessary to achieve low electron beam emittance, which is determined by the size of the electron emitting area and by the solid angle subtended by the electron beam. The electron beam will expand due to the space charge effects. However, higher accelerating voltage will make
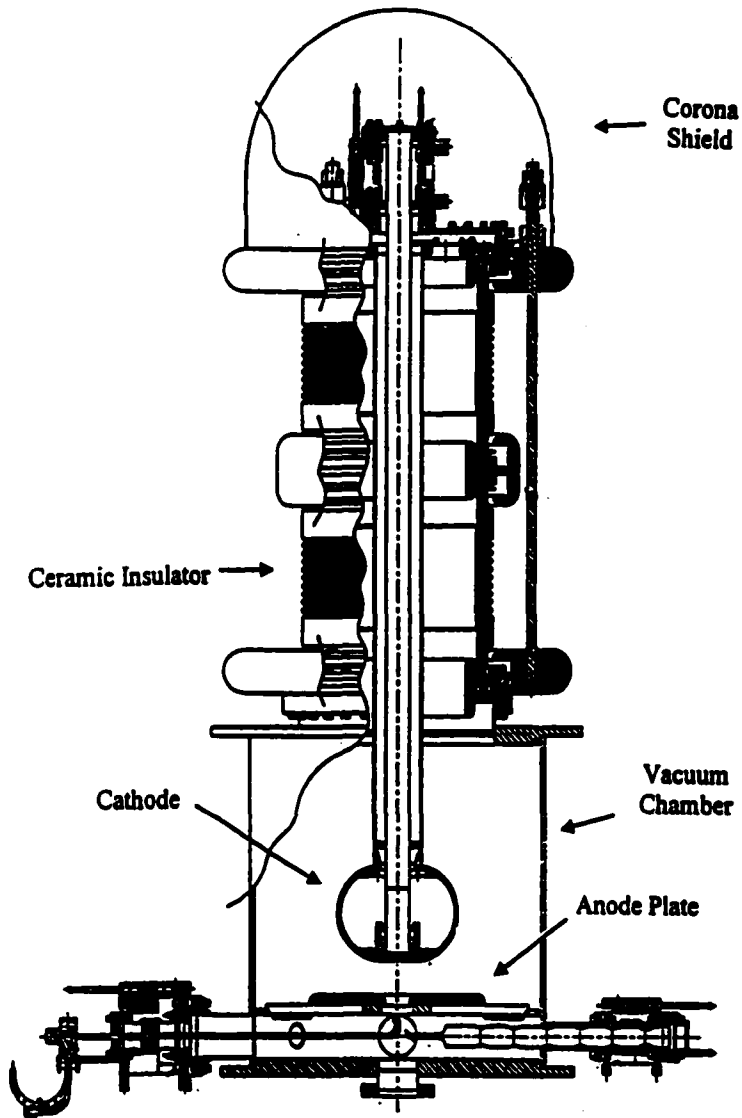
Figure 1.1. Free Electron Laser electron injection gun at Thomas Jefferson National Accelerator Facility.

the beam travel faster toward its final target, allowing less time for the beam to expand thus yielding a lower emittance.

Presently, the operating voltage of the electron guns at TJNAF is limited by field emission from the metal electrodes and the supporting structures. The same problem exists for other field particle accelerators, electron sources, and DC high voltage structures. As applied voltage increases, a small current begins to flow between electrodes, which usually precedes the formation of arcs. Arcs usually cause surface damage that further enhances field emission causing more arcs, resulting in lower operating field strength of the electron gun. The electron emission and ultimate breakdown voltage between these vacuum insulated metal electrodes is believed to be caused by reduction of local work function, or by the enhancement of local field strength as a result of surface imperfections, such as sharp points, inclusions, and foreign contaminants. Currently, extensive hand polishing is used to enhance electrode performance, requiring a surface finish of 9 μm to 1 μm. The polishing is very time consuming and difficult for these large 3-D structures. Even after extensive polishing, the performance of the electrode is unpredictable, with turn-on voltages varying by factors of 2 or more for similarly prepared electrodes. Previous study indicated that nitrogen ion implantation reduced field emission from 1 cm ID stainles steel test samples [2]. However, it is necessary that high voltage breakdown experiments be conducted on full-scale electrodes in the TJNAF test facility, because of the so-called "Total Voltage Effect" [2], and the non-linear relationship between breakdown field and gap voltage.

An important goal of this dissertation is to develop a large-scale, 3-D, uniform surface processing technique for these high voltage electrodes to suppress field emission. It is also

important that the process keeps the original target dimensions, without thermal distortion of the target or degradation of original surface finish.

Coating and ion implantation are two important types of surface processing techniques. Physical vapor deposition (PVD), chemical vapor deposition (CVD), solution and sol-gel techniques, and thermal spray processing are frequently used to produce coatings. PVD uses vapor to transport a material from a solid or liquid source onto a substrate to form coatings [4]. PVD methods provide mainly line-of-sight coverage and have difficulties coating 3-D objects with complex shapes. Solution and sol-gel processes can produce limited types of coating, although they are inexpensive and relatively fast to coat large or complex substrates. The thermal-spraying process is physically aggressive, and it is difficult to fine tune the film structure and composition. On the other hand, CVD processes rely on specific chemical reactions on or near the substrate surface to obtain desired film composition, thus allowing reproducible film composition and 3-D coverage of the target. Usually a higher substrate temperature is beneficial to promote chemical reactions on the surface, and to enhance the film deposition rate and the ability to coat complex shapes. Plasma enhanced chemical vapor deposition (PECVD) is widely used to produce high quality thin films at higher deposition rates, such as DLC films [5–7] and silicon nitride films [8, 9].

The ion implantation process is a low-temperature surface processing technique. Ions are accelerated into substrate surface to change its atomic composition and structure, thus changing the surface materials property. It causes minimal thermal distortion of the target, no degradation of surface finish, and no dimensional change of the work piece. Unlike thin film deposition processes, there is no bonding failure or surface layer delamination prob-

lem. Implanted species concentration and profile are easily controllable. Ion implantation is also a non-equilibrium process, producing new alloys not limited by classical thermodynamics and diffusion kinetics.

Plasma source immersion ion implantation (PSII) technique was developed for high-dose, three-dimensional, large-area surface processing, in order to overcome the line-of-sight problem and the limitation of beam current of traditional beam line implanters [10–12]. Instead of an ion beam, PSII uses a plasma of the species to be implanted as the ion source. The target is immersed in the plasma. By applying high voltage negative pulses to the target, positive ions in the plasma are accelerated and subsequently implanted into the substrate surface. All the surfaces of the target exposed to the plasma are implanted simultaneously. There is no need for target tilting or rotation. PSII is especially advantageous for large-area, uniform, three dimensional, and high-dose implantations.

PSII has been widely applied to materials processing. Different plasma sources have been used, including hot filament [2,11,13], cylindrical coil RF inductively coupled plasma [14], RF capacitively coupled plasma [11,15], microwave plasma [16], and glow discharge [11]. To realize PSII technique's potential of treating large work pieces, several large-scale PSII systems have also been built, including systems at Los Alamos National laboratory [15], Hughes Research Laboratories [13], and the University of Wisconsin [11]. However, none of these large-scale PSII systems takes advantages of the planar coil RF inductively coupled plasma (RFICP, here abbreviated to RFI) source, a source which is widely used to generate low-pressure, high-density discharges and which demonstrates the potential for large area processing and improved spatial uniformity [12, 17]. Since RF power is usually

coupled to the plasma inside the vacuum chamber through a quartz window, there are no electrical connections or supporting apparatus inside the chamber to take up extra space or complicate chamber geometry.

Rf inductively coupled plasma source has previously been cited in the literature for its potential for large-area processing and improved spatial uniformity [12, 17–20]. Inductively coupled plasma deposition (ICP) also has the advantage of independent control of the discharge power and substrate bias voltage, which is very important in controlling the incoming ion energy to the substrate [12, 17, 20]. ICP systems are also easy to implement.

RFI PECVD and large-scale RFI PSII were designed, built, and used as the surface processing tools for experiments presented in this dissertation. Both PECVD and PSII are non-line-of-sight surface treatment techniques. With the large-area, high density, uniform plasma generating capability of RFI source, large-area, uniform, 3-D surface processing were possible using RFI PECVD and RFI PSII.

1.2 Organization of the Dissertation

This dissertation presents the results of surface processing by RFI PECVD, large-scale RFI PSII, and large-scale RFI PSII/PVD. The RFI PECVD system is capable of large-area uniform diamond like carbon (DLC) films deposition. For the RFI PSII and RFI PSII/PVD work, a large-scale system was designed and built, capable of processing multiple small samples and large 3-D targets, such as the 8 in. i.d. electrode used for FEL electron injection gun.

To generate a large volume, uniform plasma in the system for 3-D processing, a large-scale planar RFI source was designed and built, which is believed to be one of the largest planar RFI sources ever built. The up-scaling of RFICP source was based on the successful operation of the 10 in. i.d. RFICP source designed for the PECVD system. The operation and characteristics of this RFI plasma source has been carefully studied by optical emission spectroscopy (OES) and Langmuir probe. These efforts have been made with the point of view that up-scaling should be included in process research to eliminate difficulties that result from unexpected behaviors in upscaling the smaller system [1]. In building the large-scale RFI, up-scaling caused special material problems, which required the adjustment of the original design and called for other techniques to ensure successful operation.

Previous study indicated that nitrogen ion implantation reduced field emission from 1 cm ID stainless steel test samples [2]. However, full-scale HV breakdown tests are necessary to ensure successful operation under higher voltages for FEL electron injection gun. The non-linear relationship between breakdown field and gap voltage, and the Total Voltage Effect, requires such extreme testing [2]. The large-scale RFI source for the PSII system makes it possible to perform 3-D uniform nitrogen ion implantation on actual FEL electrodes, for full size HV breakdown tests at TJNAF.

During the course of this work, MAGIC modeling was used for the first time to elucidate important PSII issues, such as sheath formation and evolution, field distribution, ion trajectories across the sheath, and dose distribution. MAGIC is an electromagnetic particle-in-cell (PIC), finite difference, time-domain code that solves Maxwell's equations

and the Lorentz force equations in 3-D space. This modeling was much more useful than simple 1-D or pseudo 2-D analytical results, made under a variety of assumptions and simplifications. It also permits direct comparison to alternative PIC modeling results of other groups. MAGIC was found to be more convenient than working with legacy plasma modeling codes or programming-restricted low-level PIC codes.

Pattern writing by implantation has also been studied as an alternative to current direct write technologies, taking advantage of the large-scale RFI PSII. Direct write technology is under intensive study as an approach to integrate 3-D mesoscopic electronic components in a conformal manner, at low-substrate temperatures, on a large variety of substrates. By integrating advanced electronics, functional devices, and active components into the substrate, one can lower the system weight and reduce cost [21]. Ultimately, machine and electronics can become one integrated system. Possible applications include miniature passive components for micro-satellites, munitions, toys, and wireless communications such as cell phones and GPS, embedded sensors for condition-based maintenance and for the medical industry. Large-scale PSII pattern writing is advantageous compared to deposition-based and ink-based direct write. It can produce features in a true conformal manner, at low temperature for a larger variety of substrates without adhesion problem or surface finish degradation.

In the course of our work, we discovered another operating mode of the RFI PSII, PSII/PVD. This mode yields a novel way to produce large-area, high quality SiO_2 films at low-temperatures on a large variety of substrates, with good adhesion. Because of the simultaneous PSII, spatial nitrogen incorporation into SiO_2 films can be controlled, which

is important for producing high quality oxynitrde multi-layers for microelectronics device manufacturing [22]. Because the processing gas is nitrogen, the chance of hydrogen incorporation into the SiO_2 films is greatly reduced. Hydrogen-free, low-temperature-deposited SiO_2 films are strongly recommended for insulating inter-layers in ULSIs and for gate insulators in thin-film transistors [23]. It is also convenient to use PSII at different operating voltages to perform in situ surface cleaning and interfacial property modification. A large FEL test electrode has also been processed by the PSII/PVD mode. Preliminary test results of the processed electrode in the TJNAF HV breakdown test facility showed much higher applied field gradients (exceeding 24 MV/m) and much smaller dark current.

Chapter 2 reports high quality DLC films RFI PECVD on Ti substrates for tribological applications. The deposition process did not require bond layer or surface pretreatment, yet yielded DLC films with excellent adhesion, which improved the substrate wear properties. For comparison, Ti/MoS_2 films were also deposited by magnetron sputtering PVD and tested along with DLC samples. As an innovation, ellipsometry was used to characterize tribological coatings. It is fast, convenient, and non-destructive compared to destructive and time-consuming mechanical tests. It also provides the advantage of yielding large-area, 3-D surfaces studying of coating quality.

Chapter 3 describes the design and characterization of a large-scale RFICP source, including dielectric window selection, rf antenna design and the effects of magnetic confinement. Langmuir probe studies of spatial plasma distribution and OES study of nitrogen plasma species are reported and are discussed in detail..

Chapter 4 presents MAGIC modeling of the PSII process. Modeling of selected geometries to study field distribution, ion trajectories, sheath formation, dose distribution are described in detail.

Chapter 5 reports pattern writing by implantation in the large-scale PSII system. Semiconductor and metal substrates were implanted through masks to study pattern transfer fidelity and lateral diffusion. Ellipsometry studies of implantation dose distribution is reported. Si gratings with 2 μm trenches were also implanted and investigated by TEM to study direct-write of small features. The results were also compared to predictions from MAGIC modeling.

Chapter 6 reports high-quality, nitrogen-doped SiO_2 films deposition by PSII/PVD. AES depth profiling was used to study the films on Si and Ti substrates. Optical properties of the SiO_2 films were studied by ellipsometry. An FEL test electrode was also processed by PSII/PVD to suppress field emission, yielding excellent preliminary results.

Chapter 7 describes high-dose nitrogen implantation of an FEL test electrode and of a group of planar transition metal samples, including Ti, Ta, Mo, Nb and stainless steel (SS). Depth profiles of concentrations, surface hardness studies, and target temperature calculations are reported. Ti and SS substrates are given more detailed attention because of their application as FEL HV electrodes.

Chapter 8 ends this dissertation with conclusions and suggestions for future work. Large-scale RFI PSII and PSII/PVD offers unique capabilities and many possibilities for large area surface processing. Recommendations and possible improvements are presented.

Each chapter also includes its own background literature reviews and comparisons to

previous studies.

Chapter 2

DLC and Ti/MoS$_2$Films Deposition on Ti Alloy for Tribological Applications

2.1   Introduction

In the course of this thesis, we designed and constructed an RF ICPECVD apparatus which

we used to create tribological coatings on Ti-based alloy substrates. We also created similar

coatings by sputter deposition, plasma spray, and sol-gel process, which were compared to

the RFI-produced coatings. The goal of this portion of the thesis was to reduce friction

in naval engine bearings. The design and operation experience of the 10 in. i.d. RFI was

also found valuable as a prototype for designing the large-scale RFI for the PSII system,

which is presented in Chapter 3. To characterize the DLC coatings, as an innovation, the

use of ellipsometry was developed to perform non-destructive assessment of 3-D large-

area tribological coatings. This technique was found valuable for PSII implantation dose

distribution study and non-destructive evaluation of coatings on PSII/PVD processed large

3-D FEL test electrode, as described in Chapter 5 and Chapter 6.

14

Titanium alloys are promising candidates for tribological applications because of their low density, high specific strength, high stiffness and high modulus. Titanium alloys rank ahead of conventional bearing steels when evaluated by the ASTM figure of merit (FOM) for materials in tribological applications. In addition to their resistance to compressive failure and their strength per unit weight, Ti alloys are resistant to most common forms of corrosion. However, Ti alloys have rather poor surface properties in other respects. While it is crucial for tribological materials to have low coefficients of friction and long endurance lifetimes, Ti alloys have high coefficients of friction and low resistance to wear. This is complicated by the fact that Ti alloys are not effectively lubricated by conventional liquid, greases, and solid coatings [24].

Plasma-sprayed Cu-Ni-In coatings have been used to protect against fretting damage on the pressure surfaces of Ti-6Al-4V alloy blade dovetails in gas turbine engines [25]. However, exposed surfaces showed moderate to severe signs of Cu-Ni-In delamination, surface crumbling, and tribo-oxidation. It is believed that failure occurs because of defects within the coating and surface embrittlement due to oxidation. In general, thermal-sprayed coatings have high surface roughness, high porosity, low thermal stability, and low reproducibility that may degrade their performance. These performance limitations demonstrate the need for alternative coatings for turbine engines. Since physical vapor deposition (PVD) and chemical vapor deposition (CVD) are capable of producing high-quality films with few defects, they were used as the deposition methods for this study.

Alternative coatings for Ti-6Al-4V should be dense, have good adhesion, oxidation resistance and low coefficient of friction. Furthermore, the coatings should have a hard

primary phase to provide wear resistance and load-bearing capability and a lubricating secondary phase to reduce the friction between the two contacting components if wear debris forms [25,26].

Two kinds of films have been studied as alternative coatings for Ti-6Al-4V surface: diamond like carbon (DLC) and Ti/MoS$_2$. Diamond-like carbon (DLC) and MoS$_2$ films have different wear and lubrication mechanisms. Diamond is naturally very hard and its friction is determined primarily by the elastic deformation of the contact region [26]. Thus it has very low coefficient of friction. On the other hand, MoS$_2$ has lamellar crystal structure. It is made of layers each of which comprises a plane of Mo atoms arranged in hexagonal array situated between two hexagonal layers of S atoms [27]. The attraction between layers is weak, so the interfacial shear strength is low, giving a low coefficient of friction [26]. However, the bonds between Mo and S atoms are covalent and strong, providing excellent load capacity.

The study of both films will be presented in the following sections.

2.2   PECVD DLC on Ti-6Al-4V

2.2.1   Introduction to DLC Films

Diamond is unique natural material with a combination of extreme properties. It is the hardest known material, having extremely low coefficient of friction (0.05) and low abrasion and wear. The surface of diamond is extremely stable and unreactive. Diamond has high thermal conductivity and heat capacity that are comparable to copper, yet low coefficient

of expansion. It is also transparent to visible and infrared radiations. Diamond is a wide-band-gap semiconductor, with a high breakdown electric field (4×10^6 to $2 \times 10^7 V cm^{-1}$), which is comparable to the breakdown field of $\sim 10^7 V cm^{-1}$ for SiO_2 [28,29].

Property	Description
Lattice constant	3.56725Å (Silicon is 5.4307Å)
Density	$3.515 kg m^{-3}$
Coefficient of expansion	8×10^{-7} (fused quartz is 2.5×10^{-7})
Thermal conductivity	$1.5 \times 10^4 W m^{-1} K^{-1}$ (copper is $4.2 \times 10^3 W m^{-1} K^{-1}$)
Heat capacity	$6.2 K J kg^{-1} K^{-1}$ (copper is $4.2 K J kg^{-1} K^{-1}$)
Thermal stability	Reacts with O_2 at $> 600\,°C$)
Young's Modulus	$1.054 \times 10^{12} N m^{-2}$ (drawn tungsten is $3.5 \times 10^{11} N m^{-2}$)
Knoop hardness	7000 (Si O_2 is 820)
Dielectric constant	5.7 (silicon is 11.9)
Band gap	$5.5 eV$ (silicon is $1.1 eV$)
Resistivity	$> 10^{18} \Omega m$, type IIa, $3.4 \times 10^{-5} \Omega m$, type IIb[b] (copper is $2 \times 10^{-8} \Omega m$)

([a]all properties are specified at 25°C unless otherwise stated.[b]Boron concentration is $2 \times 10^{27} m^{-3}$)

DLC films have been under intense investigation because of their valuable properties [30]. Although DLC films do not have all the qualities of single crystal diamond, they do exhibit some characteristics comparable to natural diamond. This makes them promising for applications such as wear resistance and impact resistance coatings for cutting tools and biomedical implants [31–33], bearings and gears, lubrication layers for moving parts, antireflective and protective coatings for optical components, protective layers for electronic devices, and heat sinks for high-temperature applications [34,35].

2.2.2   DLC Films Deposition by Thin Film Processing Techniques

Researchers have used chemical vapor deposition (CVD) [5, 36, 37], plasma-enhanced chemical vapor deposition (PECVD) [5–7], ion beam assisted deposition (IBAD) [38–40], magnetron sputtering [41, 42] and other novel methods such as laser ablation [43] and plasma source immersion ion implantation (PSII) [44] to deposit diamond-like carbon. Of the methods above, PECVD seems the most promising for depositing large-area, high-quality films at high deposition rates [12, 18, 19]

Radio-frequency inductively-coupled plasma-enhanced chemical-vapor-deposition (rf ICPECVD) was used in this work to deposit DLC films on Ti-6Al-4V substrates. Rf ICPECVD has previously been cited in the literature for its potential for large-area processing and improved spatial uniformity [12, 17–20]. Inductively coupled plasma deposition (ICP) also has the advantage of independent control of the discharge power and substrate bias voltage, which is very important in controlling the incoming ion energy to the substrate [12, 17, 20]. ICP systems are also easy to implement.

DLC coatings on Ti-6Al-4V have been studied previously by other groups, who used ion beam assisted deposition processes [38–40, 45]. Ion implantation gives better adhesion than other surface coating processes, since there is no abrupt interface to suffer debonding [31]. In two of the previous studies, a multi-layer coating with a nitrogen diffusion layer, using a thin Si film to serve as a bonding layer, was needed to improve the adhesion between the DLC film and the substrate [38, 39]. In the other studies, SiC was needed as bond layer between the DLC and the substrate to overcome delamination of directly deposited films [40]. Compared to ion beam assisted deposition techniques, rf ICPECVD is advanta-

geous because it does not require surface pretreatment (see below), it has large area coating capability, it is a relatively simple coating process, and it produces films with excellent adhesion. Most important, this coating method does not require a complicating bond layer step.

2.2.3   DLC Films Deposition by RFI PECVD

We designed and built a special apparatus to perform ICPECVD of DLC for this work. The system is shown schematically in Fig. 2.1. The top of the chamber is a 1.27×10^{-2} m thick quartz window. The rf antenna, which sits inside a steel cylinder for radiation shielding, rests on the window during deposition. Methane and hydrogen flow into the chamber through a side port. The distance between the heater stage and the quartz window can be adjusted. To protect the rubber O-ring seals on the top of the chamber when the substrate is heated, a water-cooled copper ring was added to the exterior seal edge.

For this study, three different substrates were coated at two different temperatures. The substrates used were Ti-6Al-4V blocks (0.00635 m×0.01016 m×0.01575 m), Ti-6Al-4V coupons (0.01875 m×0.01875 m×0.003 m), and Rene 80 blocks (0.00635 m×0.01016 m×0.01575 m). Our Rene 80 samples were nickel alloy containing 13.7-14.3% chromium, 4.8-5.2% titanium, 2.8-3.2% aluminum, 3.7-4.3% tungsten, 3.7-4.3% molybdenum, 9.0-10.0% cobalt, sampled from supplies used for turbine engine blades.

The surface finish of all substrates was 1.6 μm rms. All were coated without further mechanical polishing. To minimize variation, all samples were coated simultaneously, although the window-to-substrate distance varied slightly from the nominal 1.0×10^{-2} m
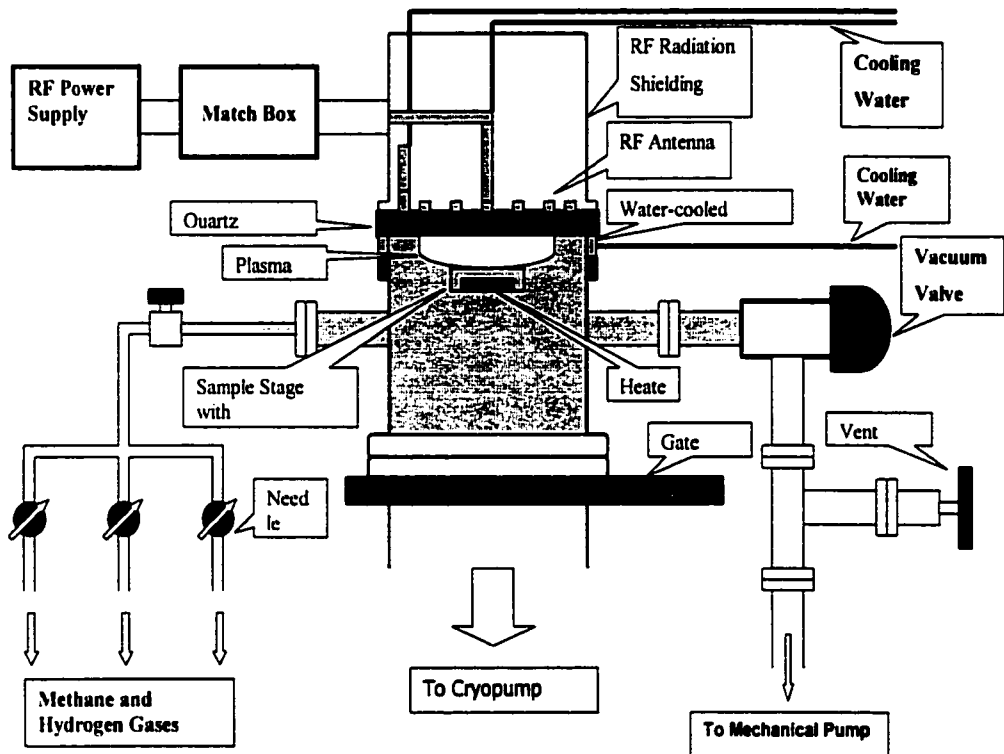
Figure 2.1. Planar coil rf inductively coupled plasma enhanced chemical vapor deposition (rf ICPECVD) system used to deposit DLC films reported in this dissertation. The rf frequency used was 13.56MHz.

because of the different sample thickness. The substrate temperature before turning on the plasma was ~800°C for the high-temperature DLC coatings. An rf power of 460 watts and a mixture of about 95%H$_2$, 5% methane at a pressure of 2.7 × 10^{-1}Pa were used. For the low-temperature DLC coatings, the substrate was heated to a temperature of ~400°C before turning on the plasma. The deposition times were approximately 8 hours in both cases.

2.3 PVD Ti/MoS$_2$ Films on Ti-6Al-4V

2.3.1 MoS$_2$ Films Deposition for Tribological Applications

MoS$_2$ is very effective as a solid lubricant [26,27,46] and it has been studied as lubricating coating on Ti-6Al-4V [24,47,48]. However, in the previous studies, described briefly below, ion implantation and bond layers were necessary to modify the Ti-6Al-4V substrate prior to MoS$_2$ sputtering coating in order to increase the adhesion strength of the MoS$_2$ film, and to increase the endurance lifetime [24]. Multi-layer coatings and various kinds of pretreatments complicate coating procedures, increase costs, and invite process variability. Mechanical polishing to remove surface oxides and improve surface finish [47,48] of Ti alloy parts is time consuming. In order to overcome these difficulties, in this work Ti/MoS$_2$ films were deposited on the Ti-6Al-4V substrates using a simple two-step magnetron sputtering process. While MoS$_2$ provides the lubrication, the existence of Ti in the coating is thought to improve the adhesion of the film to the substrate.

2.3.2   Ti/MoS₂ Films Deposition by Magnetron Sputtering PVD

A magnetron sputter deposition system was used to deposit the Ti/MoS$_2$ films for the study. A schematic of the system is shown in Fig. 2.2.

Argon plasma was used for all depositions. Ti/MoS$_2$ films were deposited at a pressure of 1.3×10^{-1} Pa - 6.7×10^{-1} Pa, at an argon flow rate of 0.5-1.0 Pa m^3/s, and a magnetron power of 100 watts. Typical sputter target bias was 400 volts dc. Two high-purity, pressed powder targets, comprised of 25%Ti/75%MoS$_2$ and 75%Ti/25%MoS$_2$, were used. The composition was varied to test the effect of Ti in the MoS$_2$ film.

In-situ surface cleaning to enhance adhesion was performed by running a DC glow discharge in the deposition chamber. The substrate was biased at -500 volts dc in a 1.33×10^1 Pa Ar/N$_2$ environment (5% nitrogen). A current density of 1.0×10^2 A/m^2 for 25 minutes was adequate for Ti-6Al-4V substrates. This step removes some of the native oxide and possibly produces a thin TiN$_x$ layer on the surface prior to deposition of the actual film, both of which improve adhesion. The pre-treatment process was required for good adhesion of Ti/MoS$_2$ coatings

2.4   Plasma Sprayed Cu-Ni-In Coating Preparation

Plasma-sprayed Cu-Ni-In coatings were deposited by an outside vendor [49] on Ti-6Al-4V substrates. The gases used in the plasma spray were nitrogen and hydrogen, with primary and secondary pressure both at 3.4×10^5 Pa. The flow pressure was 6.9×10^5 Pa. The spray distance was 6.35×10^{-2} m and the spray rate was 7.6×10^{-4} kg/second [25].
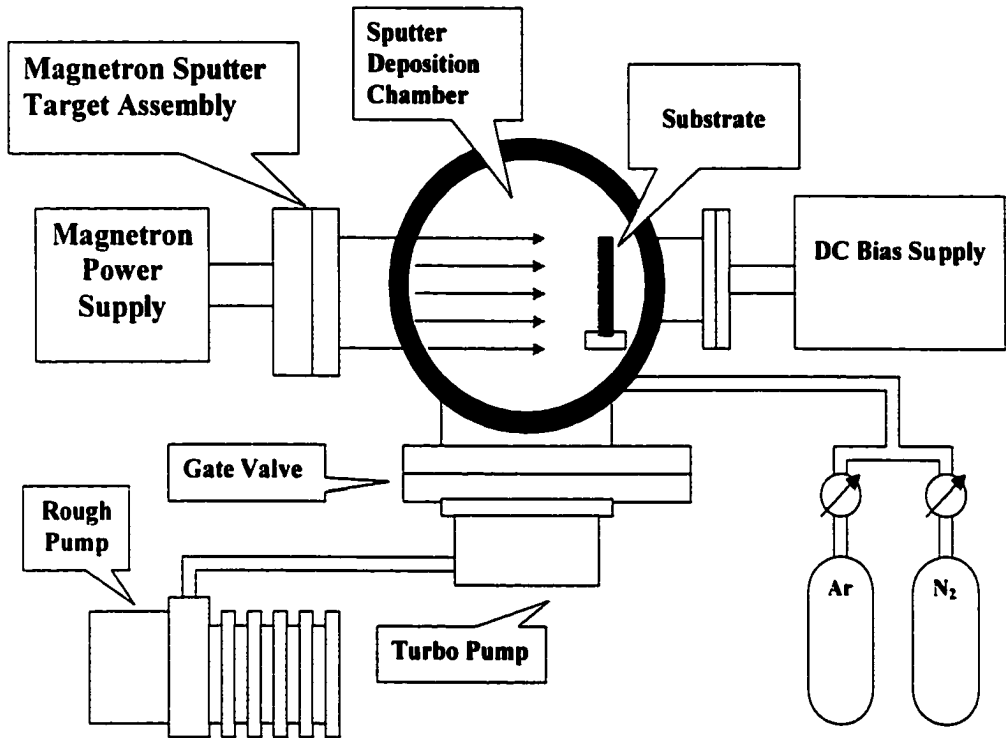
Figure 2.2. Magnetron sputtering deposition system used to coat Ti-6Al-4V substrates with 75%Ti/25%MoS$_2$ and 25%Ti/75%MoS$_2$ films.

2.5 DLC and Ti/MoS$_2$Films Characterization

2.5.1 Ellipsometry Study of DLC Films

In order to provide a rapid and practical assessment of film coating quality and to indicate whether further testing was warranted, we investigated the DLC films with optical methods. Ellipsometry provides a fast, convenient, and non-destructive quality assurance step prior to undertaking the more time-consuming and destructive mechanical analyses.

An M44 Variable Angle Spectroscopic Ellipsometer (J. A. Woollam Co. [50]) with WVASE32^{TM} software was used to study the thickness of the DLC films. The Cauchy Optical Model [51] was used to fit the experimental data. The method provides an accurate measurement of film thickness. Since the optical properties of diamond are well known, the comparison of the PECVD DLC on Ti-6Al-4V with diamond is a good indication of sp^3 content of the film. To our knowledge, this is the first time Ellipsometry has been used to study DLC film quality. We also correlated these measurements with interference color and the visible appearance of the films in an effort to provide a quick technical indication of thickness and smoothness. This sort of practical guide has been found to be of value to industrial practitioners [52, 53].

2.5.2 Hardness Test

Film hardness was tested using a Type M Shimadzu Micro Hardness tester. At least 10 indentation measurements were averaged for each sample. Tests were conducted for DLC

films of different thickness and Ti/MoS$_2$ films. If not noted otherwise, the load used was 2.5×10^{-2} kg.

2.5.3 Pull Test

Film adhesion tests were done with a commercial pull tester [54]. The test procedure was as follows: a hollow cylinder 2.8×10^{-3}m in diameter, filled with epoxy, was secured perpendicular to the face of the sample, using a fixture provided by the manufacture. The sample and stud fixture were heated to 150°C for one hour, then cooled to room temperature. The fixture was removed and the sample placed in the apparatus that pulled downward with a measured, increasing force while holding the sample stationary. The instrument records the highest value of force applied before failure. Microscopic examination of the delaminated areas was used to determine the actual contact areas, which were used to calculate the tensile pressure required to delaminate the film.

Since the pull test is destructive, only a small number of samples were tested.

2.5.4 SEM Study

Scanning electron microscopy (SEM) was used to study the surfaces of bare and coated Ti-6Al-4V substrates and the sample surfaces after pull tests and block-on-ring tests. All samples, with the exception of adhesion test specimens, were rinsed with ethanol prior to analysis to remove any surface contamination. SEM was used to confirm that all reported pull test samples failed at the film-substrate interface and not from epoxy failure. Pull test data was adjusted by calculating the actual pull-off areas of the coatings from the

SEM micrographs. SEM was also used to study the wear scars on the bare, PECVD DLC, magnetron sputtered $25\%Ti/75\%MoS_2$, and plasma-sprayed Cu-Ni-In coated Ti-6Al-4V blocks after the block-on-ring test.

2.5.5   Tribological Tests

Pin-on-disk Test

The friction and wear properties of the bare, plasma-sprayed Cu-Ni-In, and magnetron sputtered $25\%Ti/75\%MoS_2$ and $75\%Ti/25\%MoS_2$ coated Ti-6Al-4V coupons were tested (a suitable DLC sample was not available) using the pin-on-disk test (ASTM G99 procedure [55]). The normal force applied to the WC pin was 1 N. The disk rotated at 7.89×10^{-2}m/s. The tests were conducted at ambient temperatures without any lubrication. Plots of the coefficient of friction as a function of elapsed time were obtained for each specimen.

The wear tracks on the samples after pin-on-disk test were analyzed using profilometry. The wear track on the bare substrate was found to be $\sim\!6.5 \times 10^{-6}$m deep. The surface of the plasma-sprayed Cu-Ni-In was too rough to accurately measure the track depth, although a wear track was evident on the material. In contrast, the profiles of the $25\%Ti/75\%MoS_2$ and $75\%Ti/25\%MoS_2$ coatings did not show any detectable scarring, demonstrating improved wear properties compared to bare substrate or plasma-sprayed Cu-Ni-In coating. The lack of scarring on the Ti/MoS₂ and the rough surface of the Cu-Ni-In made it im-

possible to quantitatively calculate a volume loss as was done for the block-on-ring test below.

Block-on-ring Test

The friction and wear properties of the bare Ti-6Al-4V substrate, plasma-sprayed Cu-Ni-In, PECVD DLC, and magnetron sputtered 25%Ti/75%MoS$_2$ coatings were also evaluated using a block-on-ring test system (ASTM G77 procedure [56]). The 75%Ti/25%MoS$_2$ coated sample was not available for this test. The frictional force required to keep the block in place was continuously measured during the test with a load cell. The substrate block dimensions were 0.01575 m×0.01016 m×0.00635 m. The 52100 steel ring (0.0625 m OD, and 0.0588 m ID) with a surface roughness of 2.2 × 10^{-7} m was heat-treated to a hardness of 62 C Rockwell and surface finish of 6-12 rms. The rotation speed of the ring was 109 rpm. A load of 8.72 N was applied to the surface of the steel ring through a line contact of 3 × 10^{-3}m. All tests were conducted at ambient temperatures without lubrication. For accurate sample comparisons, each sample was tested for the same period of time under the same conditions. The wear loss was reported as the volume loss in cubic millimeters, calculated from the width of the block scar after the test. Mass loss data were obtained from the pre- and post-test weights of the blocks and rings.

2.6 Characterization Results and Discussion

Optical measurements of the PECVD DLC films on both Ti-6Al-4V and Rene 80 substrates show that they are highly transparent. When viewed under fluorescent room lights, the films

show bright interference patterns that change with different viewing angles. Fig. 2.3 shows one typical set of such measurements, yielding a value of n around 1.9 (typical index of refraction of single crystal diamond is 2.42 at 5890 Å), and a small extinction coefficient (typically k<0.10), as shown in Fig. 2.4.

Ellipsometry indicates that DLC deposition yields smooth surfaces. This is confirmed by SEM studies showing that the DLC (Fig. 2.5) is much smoother than the magnetron sputtered Ti/MoS$_2$ or the plasma sprayed Cu-Ni-In (Fig. 2.6 and Fig. 2.7).

Table 2.1 shows pull test results for PECVD DLC, Ti/MoS$_2$, and Cu-Ni-In coated Ti-6Al-4V samples. The values in the table were calculated using accurate pull-off areas measured from SEM photos, such as those shown in Fig. 2.8 and Fig. 2.9. The tensile failure force for PECVD DLC on Ti-6Al-4V coupon was found to be 1.1×10^2MPa, indicating a good bond between the DLC film and the substrate. The type of bonding between the DLC film and the substrate determines the adhesion. DLC films deposited on transition metals such as Ni, Fe, and Co usually result in the formation of interposed graphite layers causing poor adhesion [57]. It is believed that the excellent adhesion of the directly deposited DLC film on Ti-6Al-4V can be attributed to the high hydrogen concentration (95%) in the rf ICP. Adding a large percentage of hydrogen to the hydrocarbon gas feed previously has been found to be beneficial in PECVD of DLC on various kinds of substrates by aiding nucleation and growth [34], and reducing surface oxides allowing carbon to react with the metal [36,37]. It has also been found that carbide formation facilitates diamond growth [33,34,58–60].

PECVD DLC thin film coated samples exhibited higher hardness than the bare Ti-6Al-4V and Rene 80 substrates. Table 2.2 shows the hardness test results for PECVD DLC and Ti/MoS$_2$ coated samples. The variability of the results can be attributed in part to the surface conditions of the substrates; the relatively rough 1.6 μm rms as-received substrate surfaces were not polished. Since the substrates are much softer than the DLC films, the Vickers test method criteria for film thickness to indentation depth were not rigorously satisfied for these thin layers. The general problem of measuring the hardness of ultra-thin, very hard layers over soft substrate has been discussed in reference [61]. Our measurements can show qualitatively that the coated samples are indeed harder (probably much harder) than the bare samples. The data shows that films with larger ratios of thickness to indentation depth yield larger hardness values, confirming this qualitative result.

Generated and Experimental Data
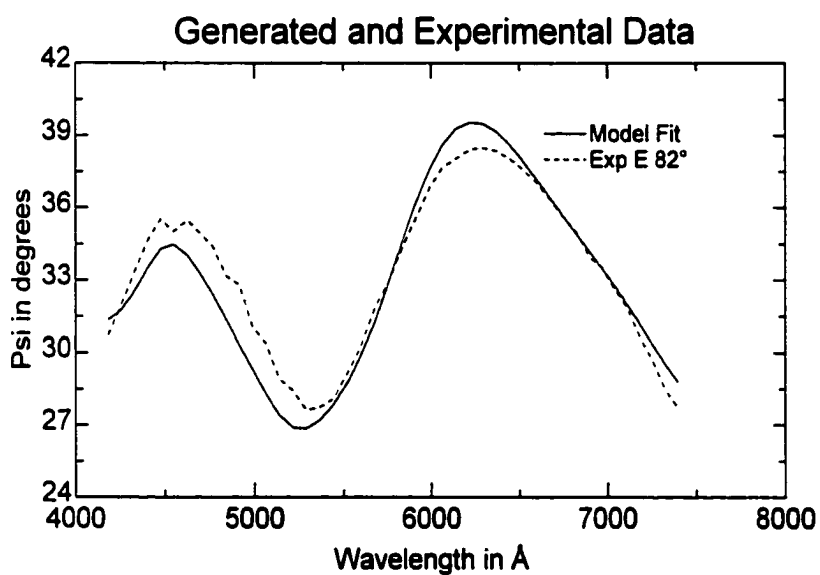
Figure 2.3. Ellipsometry study of PECVD DLC film on Ti-6Al-4V substrate using J. A. Woollam M44 variable angle spectroscopic ellipsometer with WVASE32^{TM} software. Cauchy Optical Model was used to fit the experimental data. Shown is a typical set of ellipsometry measurements (dashed) and model fitting results (solid) of PECVD DLC films on Ti-6Al-4V substrate.
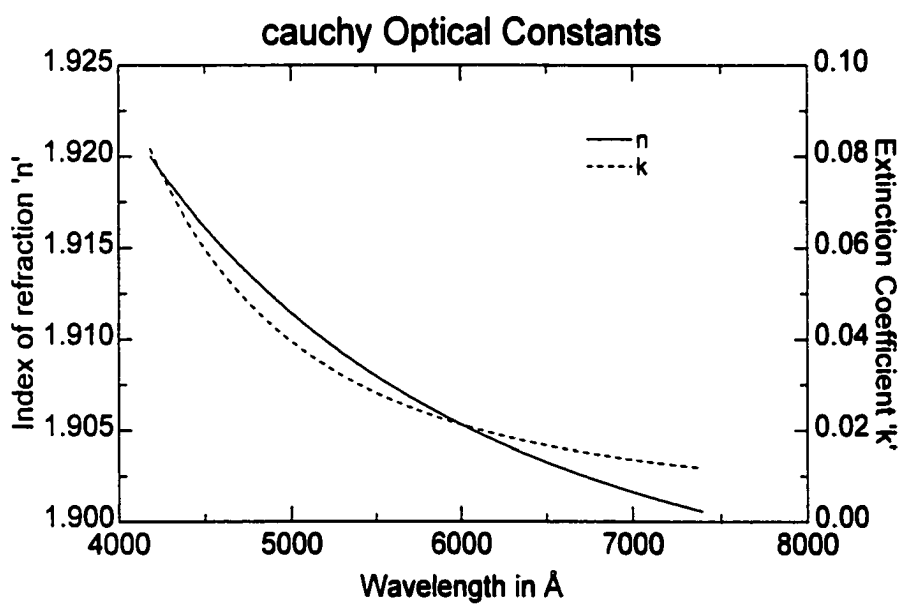
Figure 2.4. Real and complex index of refraction versus wavelength extracted from Ellipsometry data modeling. The best-fit thickness is 4230±60 angstroms. Typical index of refraction of single crystal diamond is 2.42 at 5890 angstroms.
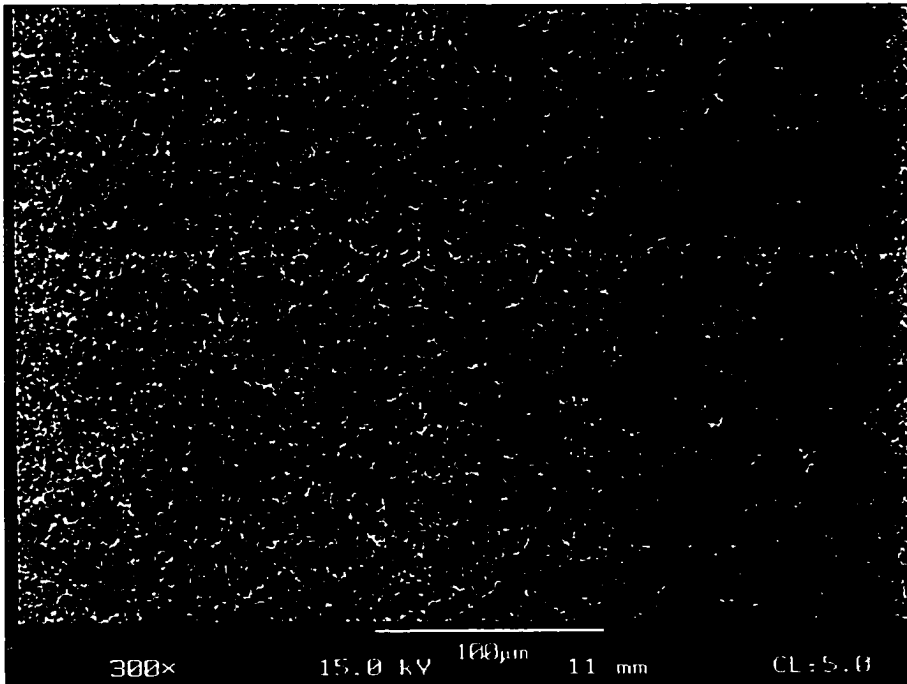
Figure 2.5. SEM picture of PECVD DLC coated Ti-6Al-4V substrate.
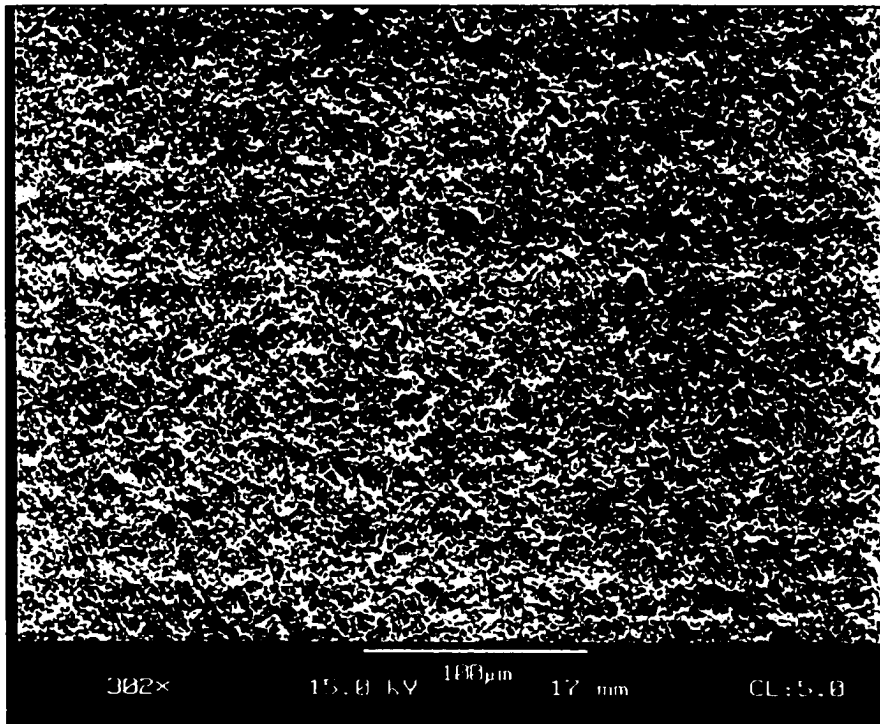
Figure 2.6. SEM picture of 25%Ti/75%MoS$_2$ coated Ti-6Al-4V substrate.
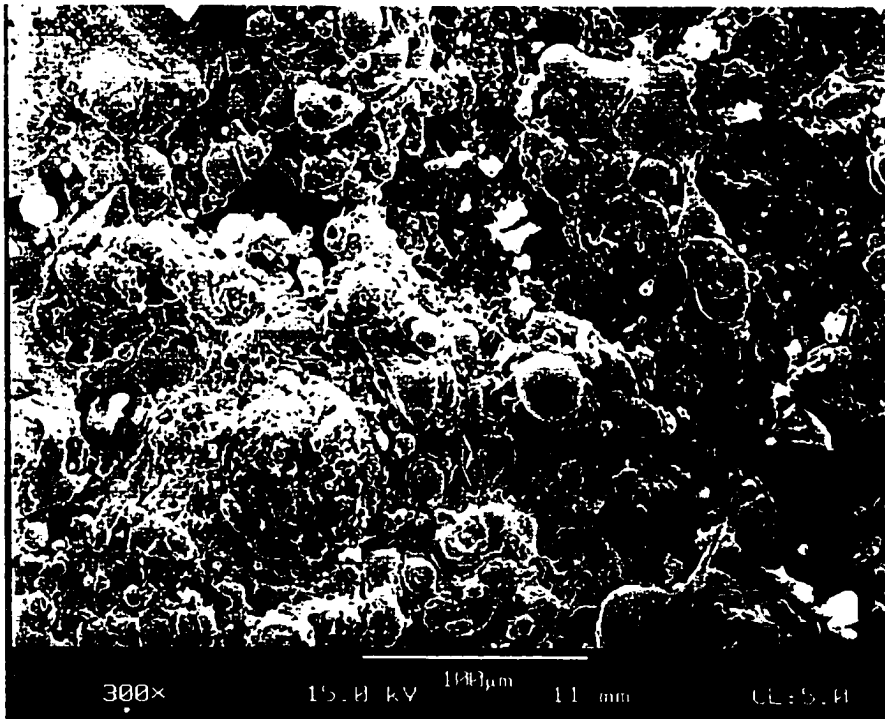
Figure 2.7. SEM picture of plasma-sprayed Cu-Ni-In coated Ti-6Al-4V substrate.
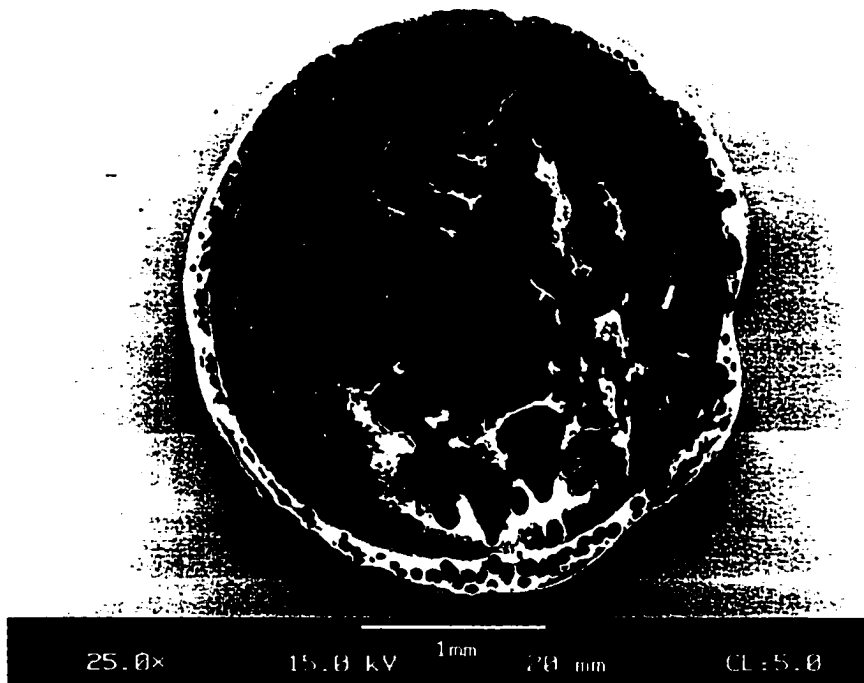
Figure 2.8. SEM study of PECVD DLC coated Ti-6Al-4V substrate surface after pull test.

Sample Name	Adhesion Strength
Plasma-sprayed Cu-Ni-In	2.7×10^1 MPa
High-temperature PECVD DLC	1.1×10^2 MPa
75%Ti/25%MoS$_2$	7.6×10^1 MPa
25%Ti/75%MoS$_2$	7.7×10^1 MPa
Ti-6Al-4V with 30-minute run of 75%Ti/25%MoS$_2$ coating	8.5×10^1 MPa
Ti-6Al-4V with 2-hour run of 75%Ti/25%MoS$_2$ coating	7.9×10^1 MPa

Table 2.1. Pull test results obtained using Sebastian IV

Mass loss data and wear loss data from block-on-ring tests for bare, magnetron sputtered 25%Ti/75%MoS$_2$, PECVD DLC, and plasma sprayed Cu-Ni-In coated Ti-6Al-4V samples are shown in Fig. 2.10 and Fig. 2.11. PECVD DLC coated block has less wear loss and mass loss than the bare Ti-6Al-4V substrate.

Magnetron sputtered Ti/MoS$_2$ films, like the DLC films, also have much smoother and more uniform surfaces compared to the rough, porous surface of the plasma-sprayed Cu-Ni-In coated substrate, as seen in Fig. 2.6 and Fig. 2.7. The hardness of 25%Ti/75%MoS$_2$ and 75%Ti/25%MoS$_2$ coated samples is higher than that of the bare substrate (Table 2.2).
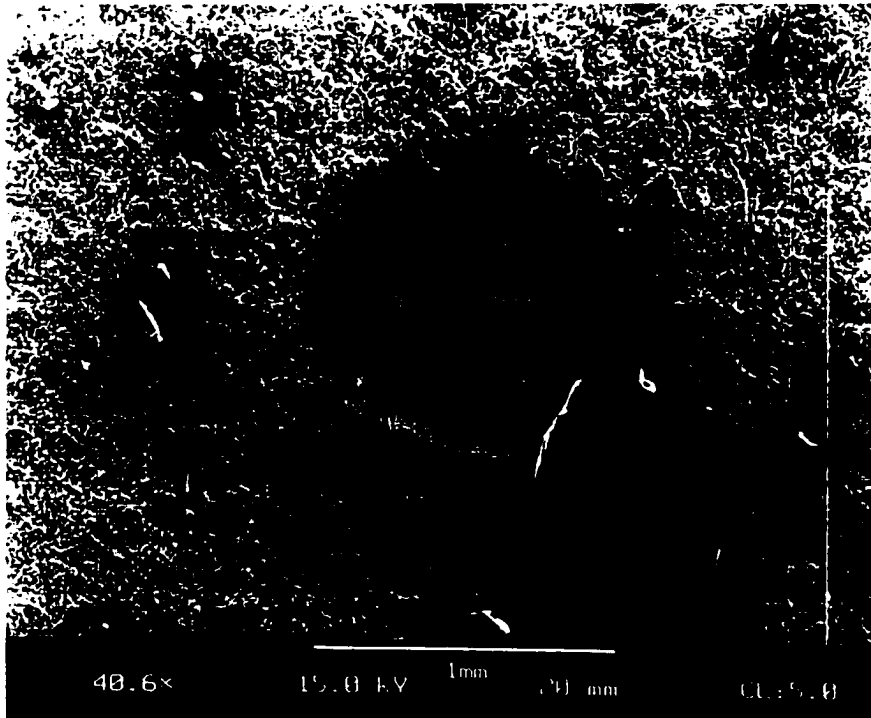
Figure 2.9. SEM study of plasma-sprayed Cu-Ni-In coated Ti-6Al-4V substrate surface after pull test.
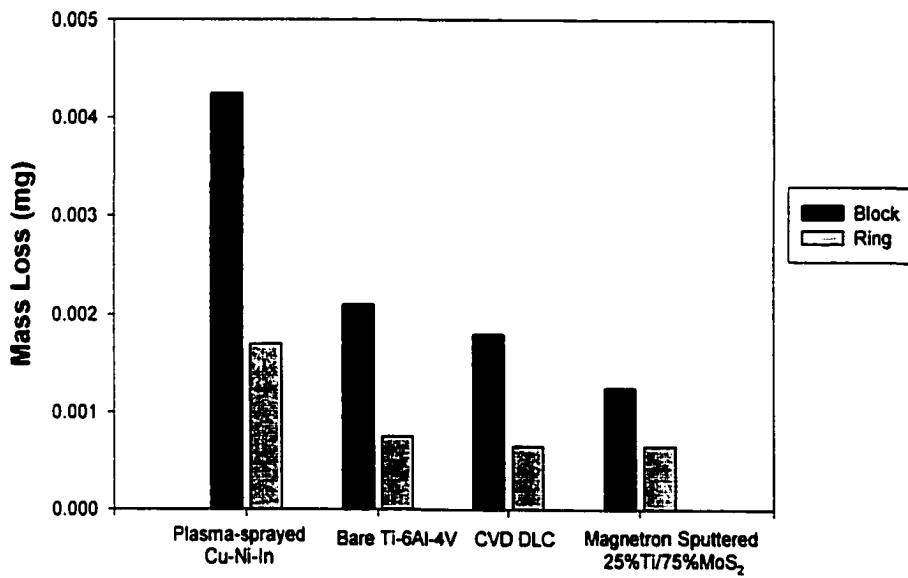
Figure 2.10. Mass loss data for the bare and coated Ti-6AL-4V blocks obtained from block-on-ring tests.
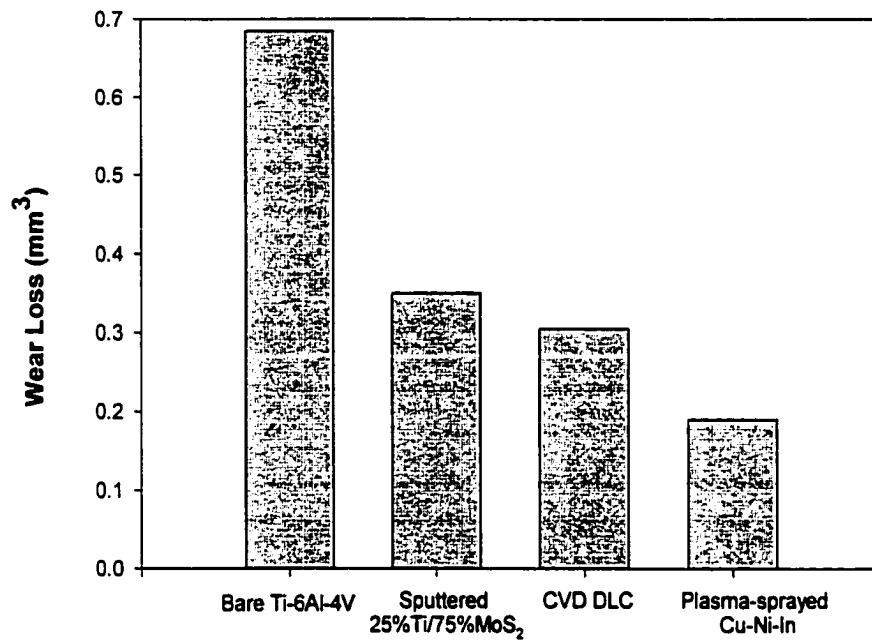
Figure 2.11. Wear loss data for the bare and coated blocks obtained from block-on-ring tests.

Bare substrate hardness (MPa)	Film name	Area color & Thickness (Å)	Hardness Value (MPa)
3500 ± 400 (Ti-6Al-4V coupon)	Low-temperature DLC	6250 ± 120 Red	6300 ± 1200
		5280 ± 120 Green	6800 ± 1600
		2760 ± 20 Sage	5100 ± 900
3400 ± 400 (Ti-6Al-4V block)	Low-temperature DLC	9750 ± 60 Red	4800 ± 800
		8550 ± 70 Green	4300 ± 600
6400 ± 2000 (Rene 80 block)	Low-temperature DLC	7690 ± 310 Red	7600 ± 1900
		13740 ± 70 Green	8700 ± 1200
3500 ± 400 (Ti-6Al-4V coupon)	High-temperature DLC	3160 ± 30 Green	6500 ± 1600
		4230 ± 60 Purple	7400 ± 2200
3400 ± 400 (Ti-6Al-4V block)	High-temperature DLC	5360 ± 50 Yellow	4900 ± 700
		5720 ± 50 Purple red	6200 ± 900
3500 ± 400 Ti-6Al-4V coupon	25%Ti/75%MoS$_2$		4100 ± 100
3500 ± 400 Ti-6Al-4V coupon	75%Ti/25%MoS$_2$		4900 ± 300
3500 ± 400 Ti-6Al-4V coupon	Cu-Ni-In		4000 ± 1600

Table 2.2. Hardness test results obtained using a Type M Shimadzu Micro hardness Tester

With added Ti, the Ti/MoS$_2$ films retained the good lubrication properties and load-bearing ability of MoS$_2$, with the advantage of improved adhesion. The pull test data in Table 2.1 show that magnetron sputtered Ti/MoS$_2$ coatings have much better adhesion ($\times 3$) than the plasma-sprayed Cu-Ni-In. The film adhesion was found to be nearly independent of film thickness in these runs, yielding similar values over a factor of four in deposition time, as seen in Table 2.1. Because of the persistent presence of surface absorbed oxygen and the difficult de-convolution of the Ti/TiO$_2$ overlap in our XPS studies, reliable quantitative data on Ti concentration in the films could not be extracted. We believe that the percentages of Ti in the films for our two choices of target are similar. This implies selective sputtering of the target must have occurred.
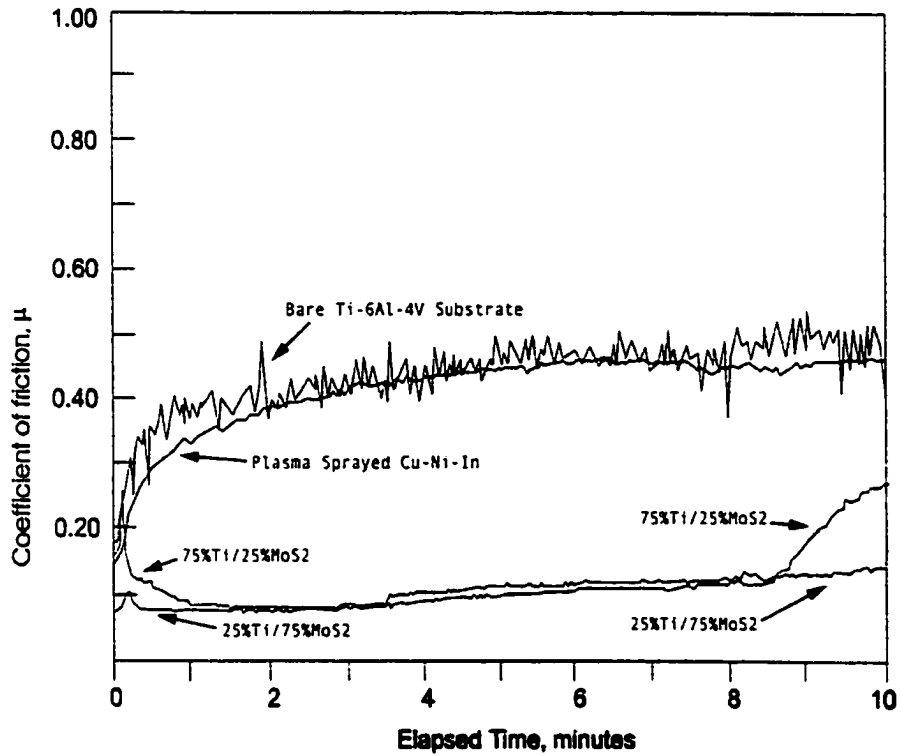
Figure 2.12. Coefficient of friction data for the bare, plasma-sprayed Cu-Ni-In, and magnetron sputtered 25%Ti/75%MoS$_2$ and 75%Ti/25%MoS$_2$ coated Ti-6Al-4V substrates.

Pin-on-disk test results indicate that the Ti/MoS$_2$ coated samples have better wear

properties than both plasma-sprayed Cu-Ni-In coated and bare Ti-6AL-4V substrates. As

shown in Fig. 2.12, the plasma-sprayed Cu-Ni-In coating, in current use to improve fret-

ting and wear properties of Ti-6Al-4V for turbine engine applications, has frictional prop-

erties very similar to the bare substrate. On the other hand, both Ti/MoS$_2$ coatings have

lower coefficients of friction than the Cu-Ni-In coating, with the 25%Ti/75%MoS$_2$ coat-

ing having the lowest coefficient of all samples tested. There was no detectable scarring

on either the 25%Ti/75%MoS$_2$ or 75%Ti/25%MoS$_2$ coated samples after pin-on-disk test

compared to the 6.5×10^{-6}m wear track depth on the bare substrate by profilometry and

the comparable wear track on the plasma-sprayed Cu-Ni-In. Block-on-ring tests show that

25%Ti/75%MoS$_2$ coated sample has lower wear loss and mass loss than the bare substrate

(Fig. 2.10 & Fig. 2.11). We found the apparent disagreement in predicting performance for

Cu-Ni-In between two standard test methods represented in Fig. 2.10 and Fig. 2.11 some-

what puzzling. The wear loss for this coating would indicate that it is superior, whereas the

total mass loss would indicate that it is inferior.

The SEM study of the details of the wear scars from block-on-ring tests, revealed that

wear loss is not a good criterion for comparing wear properties of Cu-Ni-In coated sample

with other samples (Fig. 2.13, Fig. 2.14, Fig. 2.15, and Fig. 2.16). The apparent low

wear loss of plasma sprayed Cu-Ni-In resulted from the low wear scar width. However, the

width of the wear track does not give a full indication of potential service life. The plasma-

sprayed Cu-Ni-In coating, shown in Fig. 2.16, did not show either parallel scratch lines
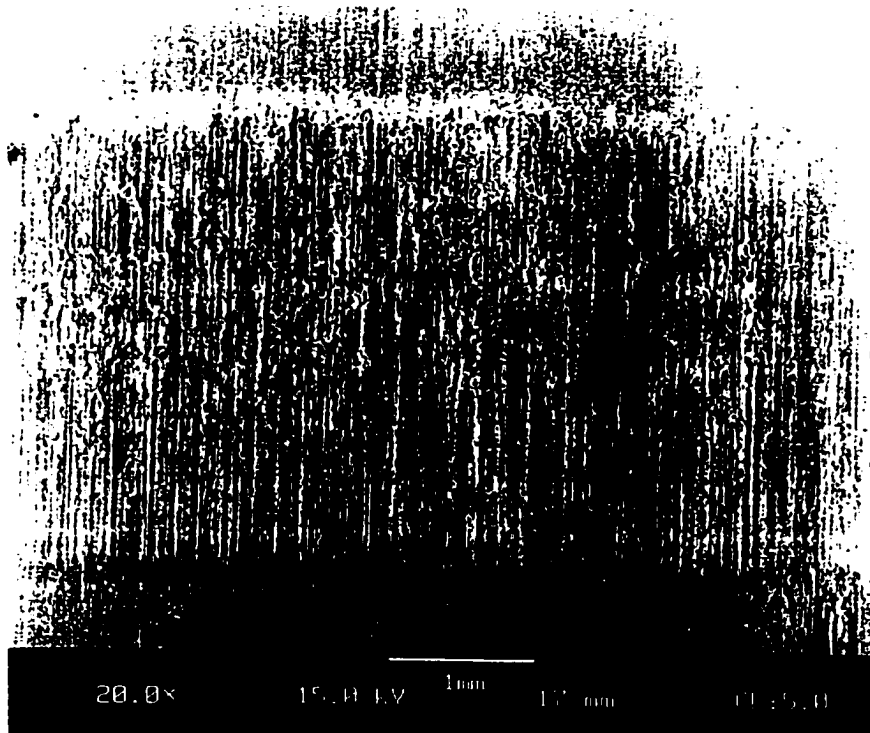
Figure 2.13. SEM study of wear scar on the bare Ti-6Al-4V substrate after block-on-ring test.
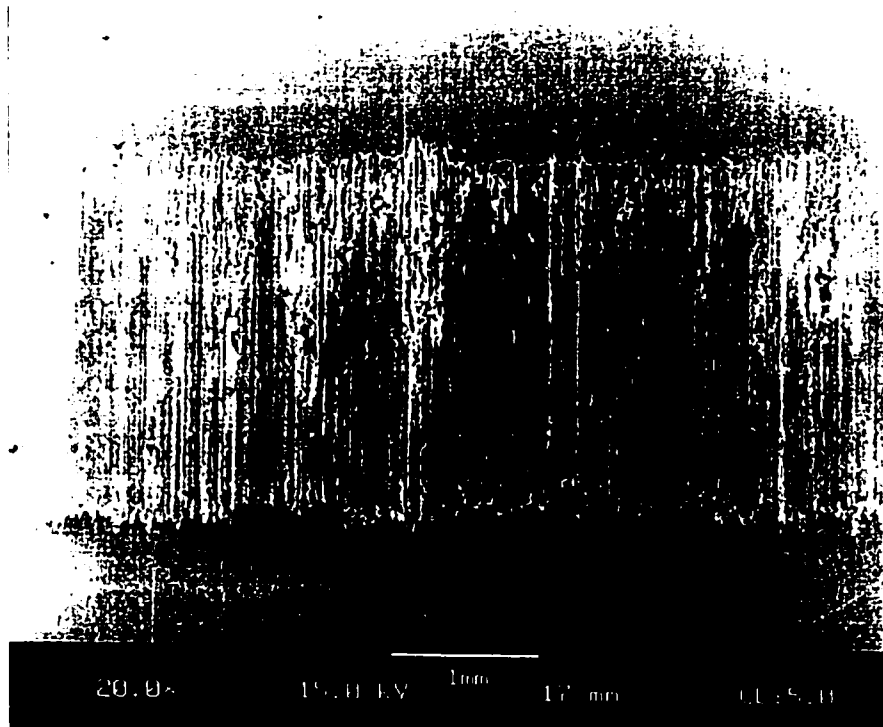
Figure 2.14. SEM study of PECVD DLC coated Ti-6Al-4V substrate after block-on-ring test.
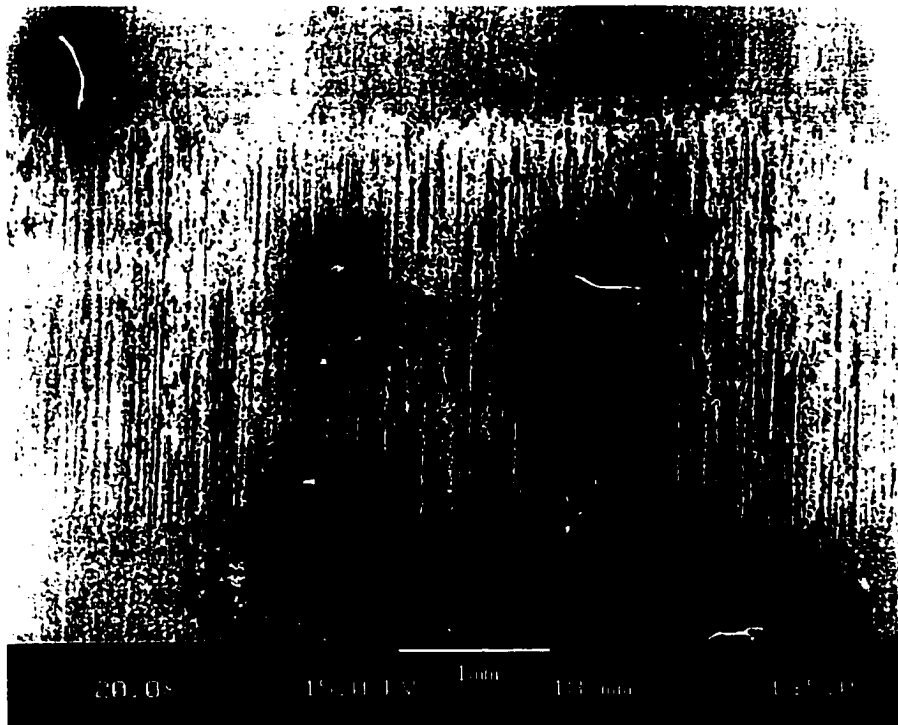
Figure 2.15. SEM study of wear scar on 25%Ti/75%MoS$_2$ coated Ti-6Al-4V substrate.
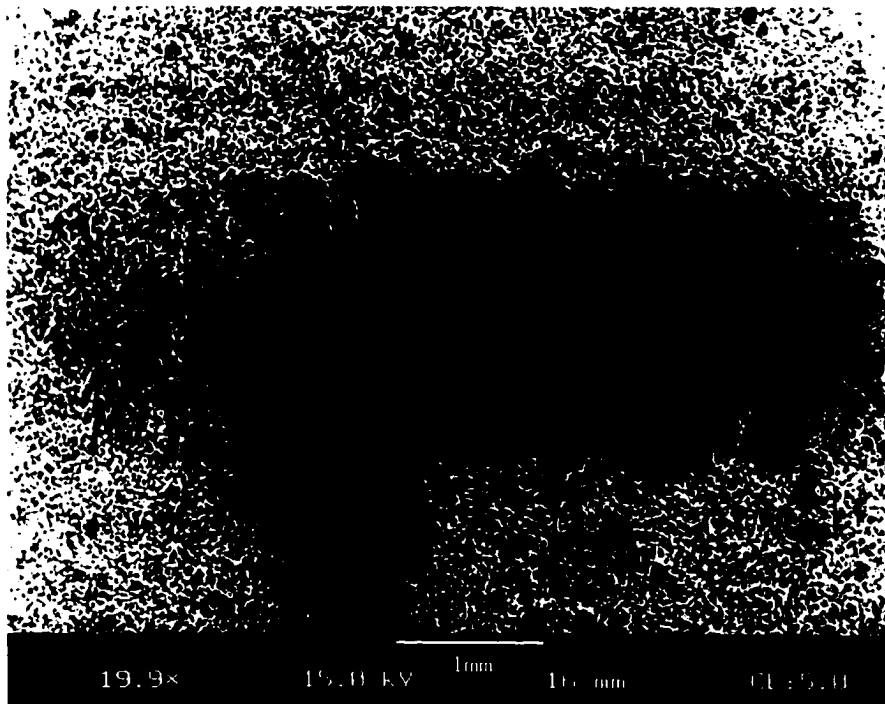
Figure 2.16. SEM study of wear scar on plasma-sprayed Cu-Ni-In coated Ti-6Al-4V substrate after block-on-ring test.

or clear wear tracks as the other samples did. The wear track was much deeper than the scars for all other samples and the damage extended beyond the nominal contact area in an irregular pattern. It appears that the plasma-sprayed Cu-Ni-In coating, which is both softer and less well-adhered than PECVD DLC and Ti/MoS$_2$ coatings, crumbled and detached under load. Since the coating is non-uniform, and contains numerous particulates, the coating delaminates irregularly near the wear track and the grit may further act to abrade the coating. Thus ASTM wear loss calculated from the wear scar width is not a good measure of the wear properties of plasma-sprayed Cu-Ni-In coatings. Actual mass loss corresponds well with the full SEM analysis. The high mass loss of the test ring is likely to be the result of excessive wear caused by the abrasive coating debris.

2.7 Summary and Conclusion

Ti-6AL-4V substrates were coated with DLC films (without surface pretreatment) and with Ti/MoS$_2$ films (with only a simple surface pre-cleaning). Both kinds of films exhibited much better tribological properties than the plasma-sprayed Cu-Ni-In coating that is currently used to protect Ti-6Al-4V against fretting and wear in turbine engine applications.

Variable angle spectroscopic ellipsometry was used to measure optical properties and thickness of the PECVD DLC films. The optical properties of DLC film helped to quickly identify the film and to indicate whether further destructive and time-consuming tests were warranted. These measurements were also correlated with interference color and visible appearance of the films to provide a quick assessment of thickness and smoothness. El-

lipsometry results showed that the DLC coatings were usually several thousand angstroms thick. It was also noted that the thickness values directly corresponded with hardness values, but not with adhesion.

DLC and magnetron sputtered 25%Ti/75%MoS$_2$ showed less wear and mass losses than the bare substrates after block-on-ring tests (ASTM G77 procedure [56]) in agreement with SEM studies. In contrast, the wear scar of the plasma-sprayed Cu-Ni-In coating showed irregular crumbling and detachment of the coating in and around the contact area, indicating poor wear resistance. Pin-on-disk friction tests were performed on bare substrate and 25%Ti/75%MoS$_2$, 75%Ti/25%MoS$_2$, and plasma-sprayed Cu-Ni-In coated substrates. These tests indicated that the Cu-Ni-In coated substrate and the bare substrate have very similar friction properties. Both Ti/MoS$_2$ coatings have better lubrication properties than the bare and Cu-Ni-In coated substrates, with the 25%Ti/75% MoS$_2$ coating having the lowest coefficient of friction of all the samples tested by pin-on-disk method (ASTM G99 procedure [55]).

Results of micro-indentation tests indicate that the DLC and Ti/MoS$_2$ coated samples have greater hardness than both the Cu-Ni-In coated and bare substrates. Pull tests showed that plasma-sprayed Cu-Ni-In coating has very poor adhesion (2.7×10^1MPa), compared to PECVD DLC (1.1×10^2 MPa). The value is 7.6×10^1MPa for 75%Ti/25%MoS2 and 7.7×10^1MPa for 25%Ti/75%MoS$_2$. Increased adhesion between MoS$_2$ films and the Ti-6Al-4V substrates may increase the endurance lifetime of the coatings [24]. The Ti/MoS$_2$ coatings have exhibited excellent adhesion and improved wear properties as tribological coatings on Ti-6Al-4V substrates. Under investigation by SEM it was found that DLC and

Ti/MoS$_2$ films look very smooth and uniform. On the other hand, the Cu-Ni-In coatings were very porous, rough and non-uniform.

Chapter 3

Design and Characterization of Large-Scale RF ICP Source

3.1 Introduction

Prior operation of the PSII system at the College of William and Mary with hot filament and DC glow discharge plasmas resulted in ion density estimated to be in the low $10^9/cm^3$ range [2], in agreement with values previously reported in other large implantation systems [13, 15]. Such low values of n_i made it difficult to produce the desired pulse shape and to control their temporal profile. The average current per pulse was lower than that designed for the pulse forming network (PFN). Though higher densities in the filament driven source were achieved by increasing the filament temperature and bias, this led to shortened filament life and the possibility of contamination of work pieces. Similarly, sputtered contaminants made it difficult to increase density in a dc glow by raising voltage. The requirement of long mean-free-path for the implanted ions eliminated pressure control of n_i as an option. In addition, both filament and dc glow discharge plasmas demonstrated large non-uniformity over the large radial and vertical dimensions of this chamber. In some

50

of the applications, such as implanting large (~30cm), shaped, highly polished objects to alter electrical properties, such non-uniformity is unacceptable. Although some effort was made to improve spatial uniformity, such as multiple hot filaments on the supporting plate at the bottom of the chamber (Fig. 3.1), its effects were not satisfactory.

To overcome these difficulties, as part of this thesis, a large RF inductively coupled plasma (RFICP or RFI) source was designed and built. With a 0.43 m in diameter RF antenna sitting on a 0.57 m in diameter quartz window, stable RFI plasmas can be generated in the chamber.

3.2 RF ICP Source

Early inductive discharges had cylindrical configurations with coils wound around evacuated tubes [12]. A ring-shaped plasma resulted because of the limited skin depth of the exciting field [17]. There was also controversy about whether these coils were capacitively driven or inductively driven. Further studies recognized that the discharge was capacitively driven at low plasma densities and switched to operate in an inductive mode at higher densities. The planar coil configuration was developed in the late 1980s with the intent of producing high-density low-pressure plasma for materials processing ($p < 50 \ mTorr$) in low aspect ratio geometries ($l/R \leq 1$ for a cylindrical chamber). Inductive discharges for materials processing are referred to as TCP (transformer-coupled plasma), ICP (inductively coupled plasma), or RFI (RF inductively plasma) [12].
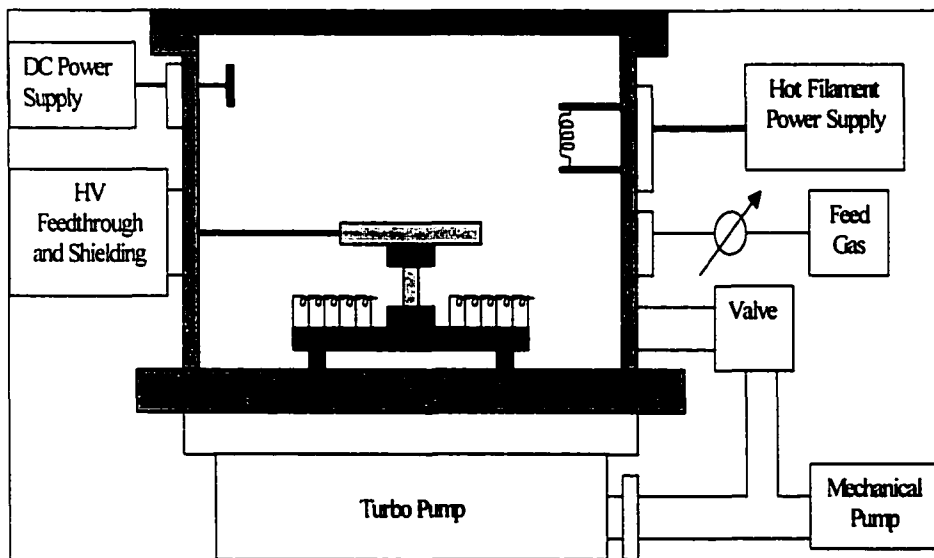
Figure 3.1. Hot filaments and DC glow discharge plasma source used for the CWM PSII.
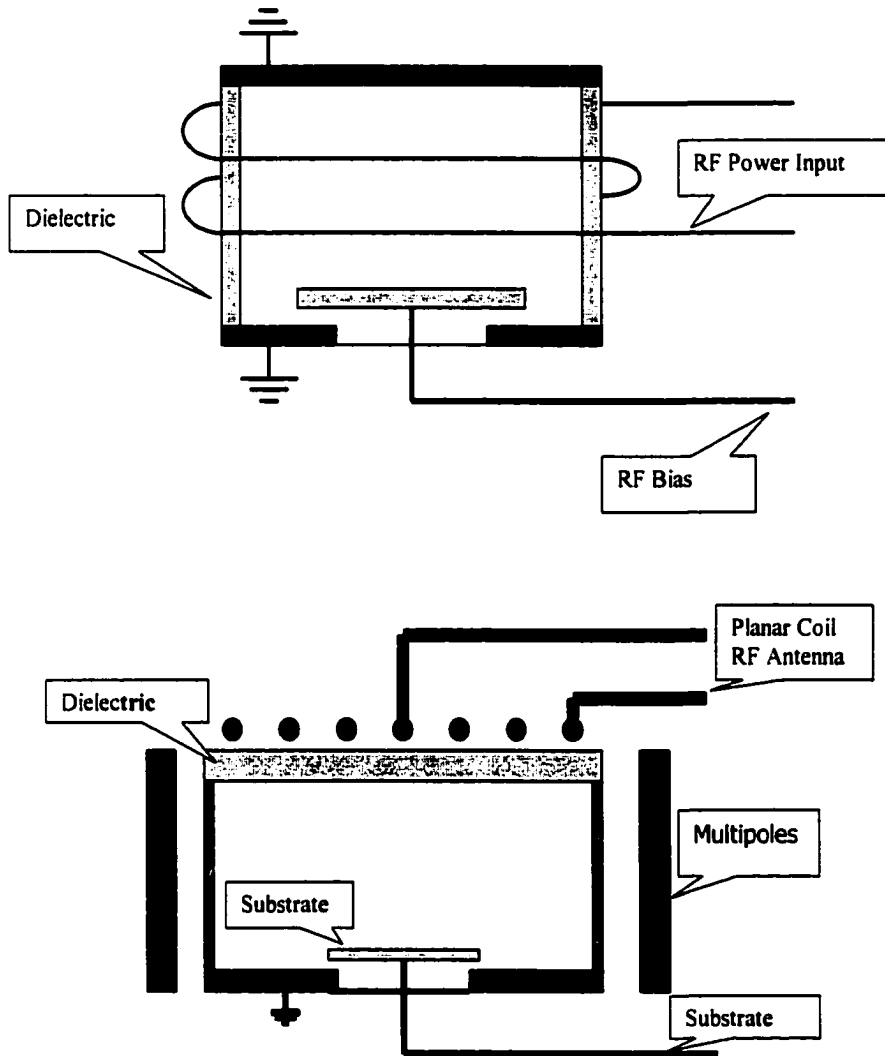
Figure 3.2. Inductively driven sources in cylindrical and planar geometries.

The schematics of inductively coupled plasma sources with cylindrical and planar geometries [12] are shown in Fig. 3.2. Both the helical and planar coils act as inductive elements in the circuit, which typically consists of additional tunable capacitors to match the coils to a 50Ω rf power supply. The dots in the planar geometry represent the cross-sections of the planar rf antenna. Because of the plasma non-uniformity caused by the skin depth of rf radiation, the cylindrical coil geometry produces strong radial variation in the chamber, which is not good for uniform materials processing [12, 18]. On the other hand, the planar geometry has been found to be able to generate uniform plasmas over large planar areas [12, 17]. For a planar geometry, the planar spiral coil is separated from the vacuum chamber by a dielectric window, which provides rf energy coupling and vacuum seal. Magnetic multipoles are often added to confine the plasma, improve the plasma radial uniformity, and raise the ion plasma density. ICP also allows for independent control of the ion/radical flux and ion bombarding energy by biasing the substrate with a second rf power supply. For most of studies, simple spiral coils have been used to generate uniform plasmas [18]. More elaborate shapes have also been studied to change radial distribution of the peak electron density [19].

3.3 Large-scale RF ICP Design and Building

3.3.1 Dielectric Window

A large rf coil was chosen to achieve large-area uniform plasma generation. Thus it is necessary to use large dielectric window for rf coupling. For our 0.61 m ID chamber, it

was possible to open a 0.44 m in diameter hole on the top flange, leaving enough space on

the flange to cut grooves for a double set of O-rings. It was decided that the appropriate

window size was 0.57 m in diameter, so that the quartz window can sit upon the two O-

rings to make the vacuum seal with a pumpable interspace between the O-rings. Such

an arrangement greatly reduces the permeation of air and water and thereby improves the

cleanliness of the process. The quartz plate is simply supported along its contour by the

O-rings, pressing down by atmosphere pressure when the system is pumped, without any

clamping or extra weight.

It is important to calculate the safe thickness for such a large quartz window to be

strong enough to stand the pressure difference without breaking. Fused quartz has the

following typical mechanical parameters [29]:

Tensile strength	$7,000\ psi$
Poisson's Ratio	0.16
Compressive Strength	$> 160,000\ psi$
Rigidity Modulus	$4.5 \times 10^6\ psi$
Young's Modulus	$10.4 \times 10^6\ psi$
Bulk Modulus	$5.3 \times 10^6\ psi$

To estimate the stress on a 0.57 m plate exerted by 1 atm of air pressure, the following

calculations were made [62].

Fig. 3.3 shows the coordinate systems for a plate. The useful results for our consid-

erations are as follows:

The load and the supporting reactions are assumed to be normal to the middle plane

of the plate. The bending moments in the plate per unit length of the cross section can be
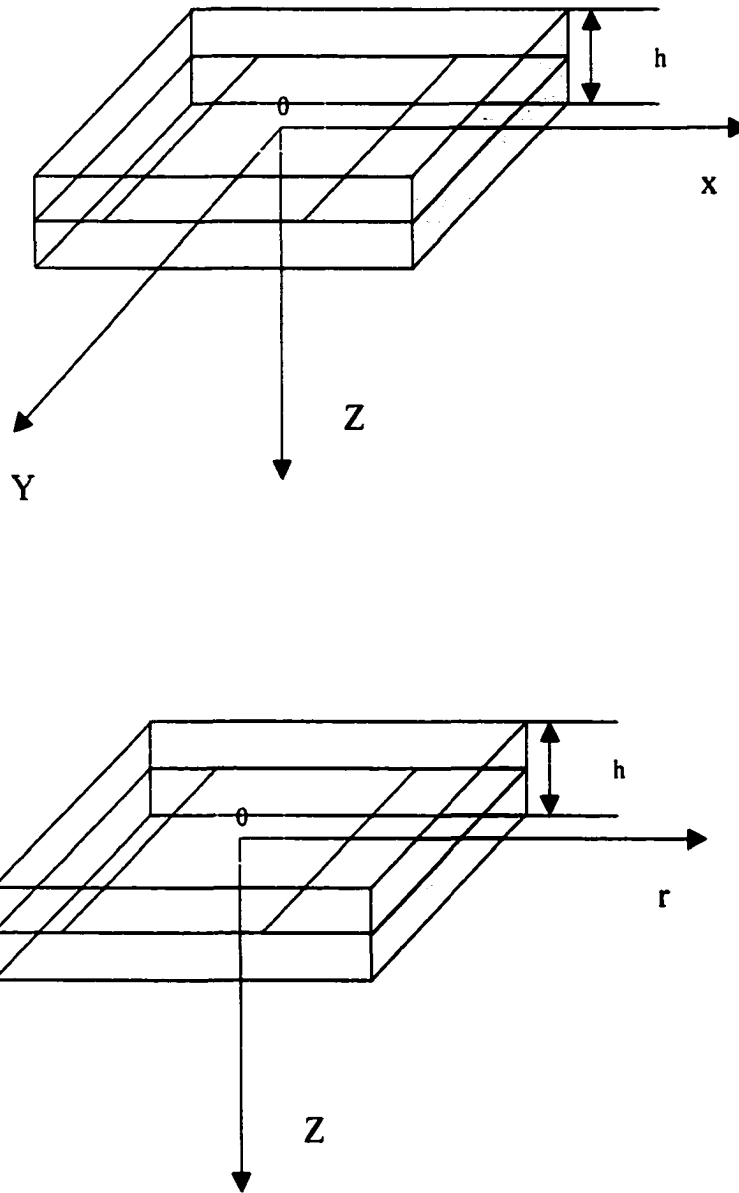
Figure 3.3. Coordinate systems for a plate.

defined as:

$$M_1 = \int_{-\frac{h}{2}}^{+\frac{h}{2}} X_x z dz \qquad \text{(Eq. 3.1)}$$

$$M_2 = \int_{-\frac{h}{2}}^{+\frac{h}{2}} Y_y z dz \qquad \text{(Eq. 3.2)}$$

X_x and Y_y are normal stresses.

Using a cylindrical coordinate system for a round plate that is simply supported along its contour, the displacement of any point on the middle plane w can be calculated by:

$$w = \frac{q}{64D}[(a^2 - r^2)^2 + \frac{4a^2(a^2 - r^2)}{1 + \sigma}] \qquad \text{(Eq. 3.3)}$$

and

$$M_1 = \frac{q}{16}[a^2(3 + \sigma) - r^2(3 + \sigma)] \qquad \text{(Eq. 3.4)}$$

$$M_2 = \frac{q}{16}[a^2(3 + \sigma) - r^2(1 + 3\sigma)] \qquad \text{(Eq. 3.5)}$$

q =pressure, a =radius of plate, r =the radius of point of interest, σ is the Poisson's ratio, which is 0.16 for fused quartz.

For a 0.57 m dielectric plate, considering the center of the plate, where $r = 0$,

$$M_1 = \frac{1.013 \times 10^5}{16}[0.285^2 \times (3 + 0.16) - 0 \times (3 + 0.16)] = 1.625 \times 10^3 \text{ N.} \quad \text{(Eq. 3.6)}$$

Where air pressure $q = 1.013 \times 10^5$ *Pascal*, and $\sigma = 0.16$.

The maximum of σ_{rr} is found at the center of the plate:

$$\sigma_{max} = \frac{3}{8}(3 + \sigma)q(\frac{a}{h})^2 \qquad \text{(Eq. 3.7)}$$

Considering the tensile strength of quartz, which is 4.827×10^7 *Pascal* (7000*psi*), $h_{\min} = 1.42$ cm (0.560 in.).

It was concluded that for the diameter of our dielectric window, it is better to choose 0.0254 m (1 inch) thick quartz to have enough safety margin.

3.3.2   RF Antenna

Usually a capacitive network is required to match an rf inductive coil, to produce a resistive 50Ω load to the rf power supply. The typical setup, shown in Fig. 3.4, consists of two capacitors, one in series and one in parallel with the rf coil. The plasma usually acts as a resistive load in the matching circuit

The admittance, looking to the right, at the terminals $A - A'$ is [12]

$$Y_A \equiv G_A + jB_A = \frac{1}{R_s + j(X_1 + X_s)} \qquad \text{(Eq. 3.8)}$$

Where $G_A = \frac{R_s}{R_s^2 + (X_1 + X_x)^2}$ and $B_A = -\frac{X_1 + X_s}{R_s^2 + (X_1 + X_s)^2}$.

At matched conditions,

$$G_A = \frac{1}{R_T} = 1/50\Omega \qquad \text{(Eq. 3.9)}$$

$$B_A + \omega C_2 = 0 \qquad \text{(Eq. 3.10)}$$

so that there is maximum power transfer from the power supply and the matching circuit behaves as a 50Ω resistive load to the power supply.

It is necessary to consider the tuning range of the available capacitors, the inductance of the rf antenna, and the load behavior of the plasma, so that match can be achieved.
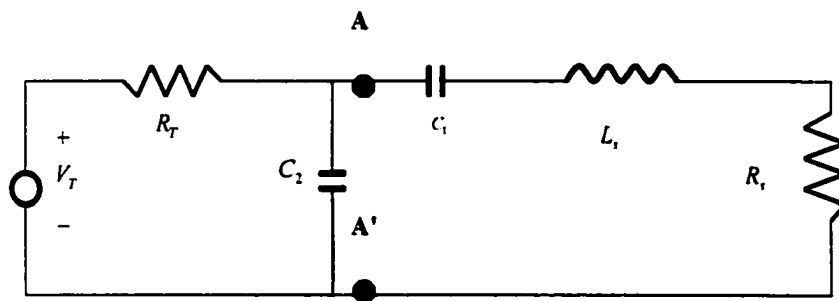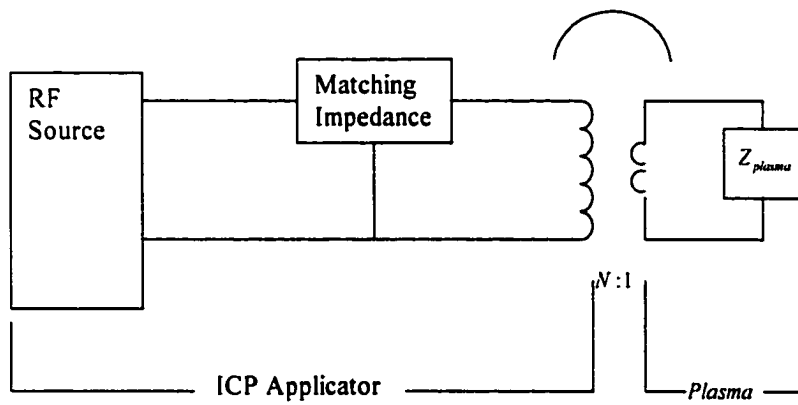
Figure 3.4. Impedance matching circuits for inductively coupled plasma

The inductance of a spiral coil can be estimated from

$$L = \frac{B^2 N^2}{8B + 11C} \mu H \qquad \text{(Eq. 3.11)}$$

where B =radius (inches), N =number of turns, C =thickness of spiral coil (inches)

Using this equation, it was calculated that for a 3 turn coil 8 inches in diameter, $L \cong 8.63 \, \mu H$.

A three-turn rf spiral coil was made for our RFI source using quarter-inch copper tube. The coil is cooled by water when operating. The two capacitors used are Jennings vacuum tunable capacitors, each with an adjustable range of 20 pF - 320 pF.

3.3.3   RF Inductive Mode Versus Capacitive Mode

To achieve ion distributions that are closer to monoenergetic, plasma source immersed ion implantation is usually operated in the sub-mTorr regime, where the plasma ion density is substantially lower than for plasmas operated at higher gas pressures.

It has been found that an RFICP discharge at low pressures has a capacitively coupled component, causing sputtering damage to the dielectric window and contamination to the processing target [12, 63]. Sugai et al. studied the electrostatic or capacitive coupling of an rf antenna to inductive plasmas [64]. They found that capacitive coupling plays an important role not only in the discharge mechanism but also in impurity release from materials around the antenna. Since the inductive coil is driven in an electrical resonance condition, it is expected that high potentials exist on the coil. Such rf potentials will lead to capacitive coupling to the discharge in the chamber, which is characterized by high negative

voltages between the dielectric window and the grounded wall. Ions are accelerated across the sheath and hit the dielectric window at high energies, causing sputtering of the window [17]. It has been observed that weak capacitively coupled discharges often co-exist with inductively coupled plasma sources at low absorbed powers. Since high potentials exist on the inductive couplers, it is doubtful that any ICP is entirely inductively coupled [17].

A Faraday shield is usually used to reduce the capacitive coupling [17, 65, 66]. Such shields are often made of a metal sheet or tube with cut slits, which shorts the capacitive fields and allows primarily the inductive excitation of the discharge. The Faraday shield used in our PSII system is shown in Fig. 3.5. The slits prevent secondary rf current from flowing through the shielding metal sheet, otherwise the metal sheet would act as a short-circuited secondary winding to the primary coil, preventing the inductive field from reaching the discharge inside the chamber.

3.3.4   Magnetic Confinement

Magnetic multipoles were placed around our implantation chamber to improve spatial plasma density distribution. Each row of magnets consists of a series of strong rare earth magnets arranged in alternating N-S directions. Each of the magnets is 1 inch by 1 inch, 1/2 inch thick. The magnetic field perpendicular to the square surface is 6800 Gauss. The alternating magnets provide a line cusp near the chamber wall, preventing plasma loss, increasing the plasma density, and improving spatial plasma uniformity [12, 67].

External magnetic fields have also been found to improve the stability of low pressure operation of RF ICP [68]. Power transfer efficiency generally decreases with decreasing
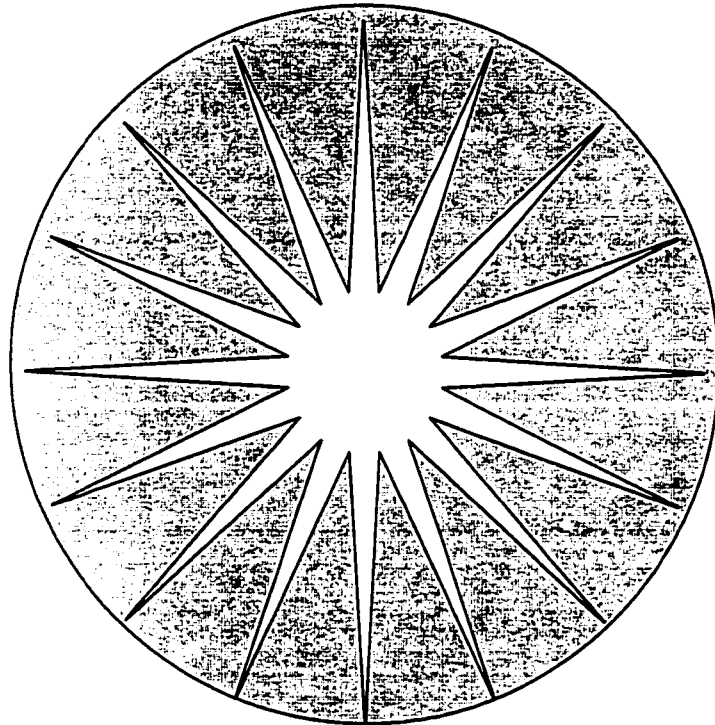
Figure 3.5. The Faraday shield made for the PSII system.

operation pressure. The magnetic field increases the electron density by decreasing the radial transport of electrons, which helps to improve power transfer efficiency. A more stable discharge is possible due to increased plasma electrical conductivity.

3.4 Characterization of RF ICP

The ICP source is shown in Fig. 3.6. The Faraday shield is separated from direct contact to the coil by a 0.0254 m thick 0.57 m in diameter quartz plate. The shield is grounded at two (or more) places on the circumference. The quartz window for making the vacuum seal is 0.0254 m thick and 0.57 m in diameter. Permanent magnets are placed around the chamber wall near the rf coil end. Processing gases are fed through the side port. The system is pumped by a turbo molecular pump and mechanical pump (see chapter 7 on surface processing by large-scale PSII).

3.4.1 Langmuir Probe Measurement

A Langmuir probe was used to characterize the ion plasma density and the radial density distribution in the cylindrical chamber before and after applying the permanent magnets around the chamber. Limited by the configuration of available ports, the Langmuir probe was mounted through a port in the middle of the chamber on a motion feedthrough about 23 cm below the quartz window. The probe can be moved to different radial positions in the chamber. The probe was connected to a bipolar power supply (Kepco), which was remote-controlled by a computer, to provide bias voltages within a desirable range having pre-programmed increments. The bias voltage and current through the probe were measured by
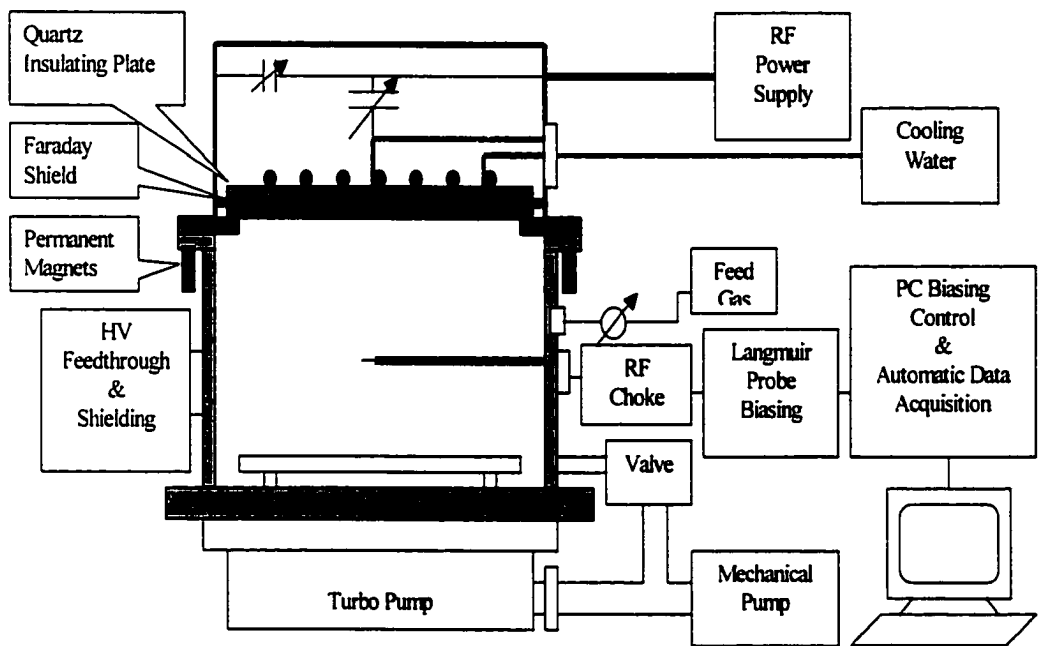
Figure 3.6. CWM RFI PSII system, showing the Langmuir probe for measurement of plasma density profiles

two multimeters, interfaced to a computer by GPIB board. Each run of the data acquisition

program collects a complete I-V curve and automatically saves the data in a file.

For the plasmas run at sub-mTorr to several mTorr pressure, collisionless sheath con-

dition can be assumed. Thus a cylindrical probe was constructed and the following equation

was used to calculate ion plasma density [69, 70].

$$I = 2en_s ad(\frac{2e \mid \Phi_P - V_B \mid}{m})^{1/2} \qquad \text{(Eq. 3.12)}$$

where e is electron charge, n_s is the density of the electrons or ions, a is the radius of

the cylindrical probe, d is the length of the probe, m is the mass of the ions or electrons

collected. V_B is the probe bias voltage and I is the ion or electron saturation current.

Fig. 3.7 shows the ion plasma density at the center of the chamber under different rf

power and pressure without magnetic confinement. Fig. 3.8 shows the radial plasma ion

density distribution at 1200 w rf power and 5×10^{-4} mTorr nitrogen gas pressure without

magnetic confinement. It is apparent that the radial ion density distribution is approxi-

mately parabolic, as expected from unhindered diffusion within cylindrical geometry.

The radial distribution of ion plasma density with magnetic confinement is shown

Fig. 3.9. The ion density for different rf power and nitrogen gas pressure with magnetic

confinement is shown in Fig. 3.10. Compared to Fig. 3.8, the radial distribution of ion

plasma density is more uniform throughout the chamber, which is very important for large

area uniform implantations. The multi-cusp magnetic field added to the drift region at the

perimeter of the chamber provides a confinement field, which improves the spatial uni-

formity and increased the total ion density in the implantation chamber, allowing faster
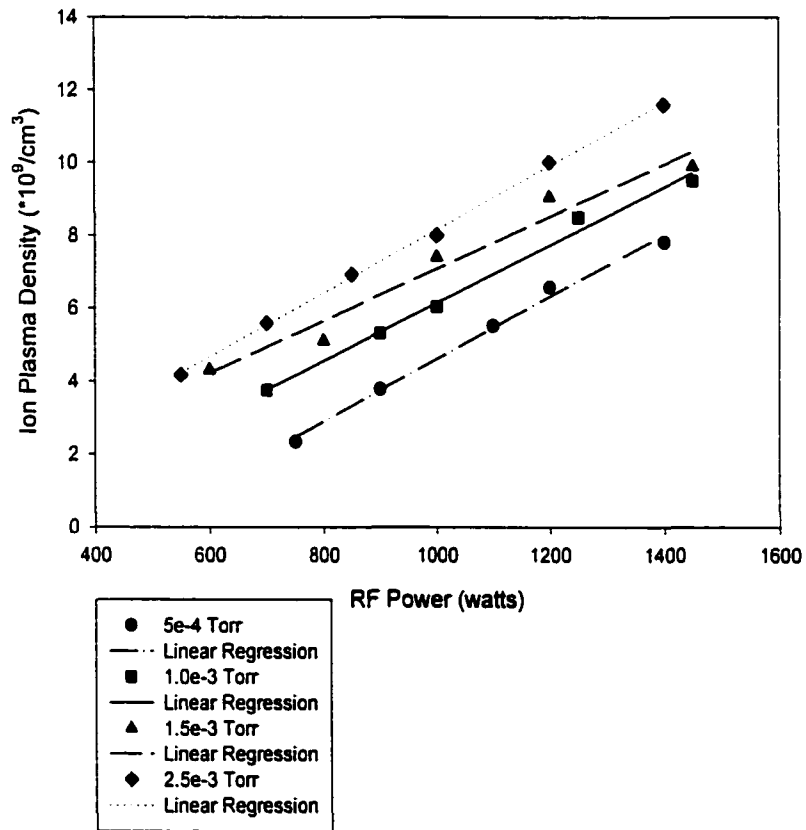
Figure 3.7. Measured ion plasma density for different rf power and nitrogen gas pressure without magnetic confinement. The probe was positioned 23 cm below the dielectric window.
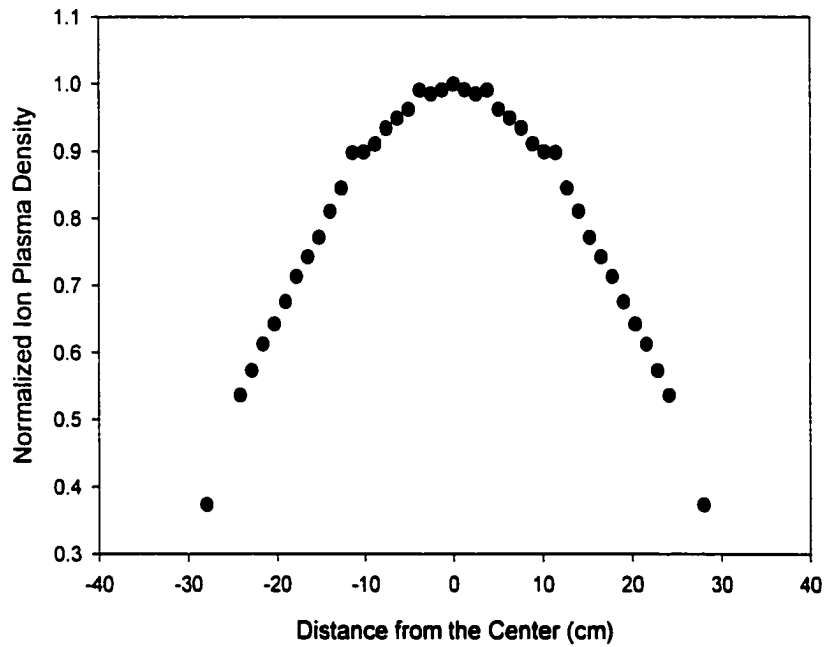
Figure 3.8. Radial ion plasma density distribution for nitrogen plasma at 1200 watts rf power and 5×10^{-4} Torr without magnetic confinement. The probe was positioned 23 cm below the dielectric window.
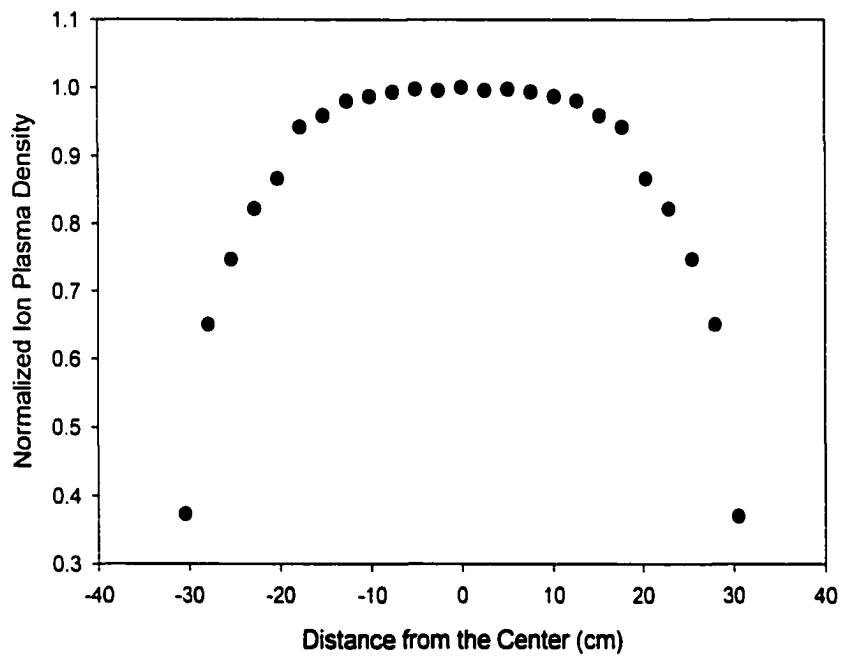
Figure 3.9. Radial ion plasma density distribution for nitrogen plasma at 1200 watts rf power and 5×10^{-4} Torr with magnetic confinement. The probe was positioned 23 cm below the dielectric window.

processing times for PSII. This result is also in agreement with previous studies [71], performed in smaller chambers.

The peak values of the ion plasma densities with and without magnetic confinement are similar for different rf powers and gas pressures. However, as shown in Fig. 3.9, magnetic confinement increased plasma uniformity and conductivity, and thus improved rf coupling efficiency [67,68].

It is also interesting to note that the rf inductively coupled plasma densities at the same powers and gas pressures are very similar to that with some degree of capacitive coupling (Fig. 3.11). It can be explained partly by the fact that with the addition of a Faraday shield and a second insulating dielectric window, the distance from the inductive coil to the plasma is more than doubled. This results from the need to use the Faraday shield to ground the high voltage on the inductive coil, which makes it necessary to introduce a second quartz plate to separate the metal shield from the inductive coil. As the distance between the coil and the plasma is increased, the mutual inductance between the coil and the plasma decreases. The increased distance thus requires a larger inductive current in the coil to sustain the discharge in the chamber. Another factor that influences coupling efficiency is gas pressure. Low electron-neutral collision frequency for low pressure plasma causes decreased plasma conductivity [67]. To maintain the same rf power absorption at low pressures, the coil current has to be higher to increase the inducted electrical field in the plasma. Since more power is dumped on the inductive coil and the capacitors at higher current, the power transfer efficiency is decreased.

Nitrogen Ion Plasma Density
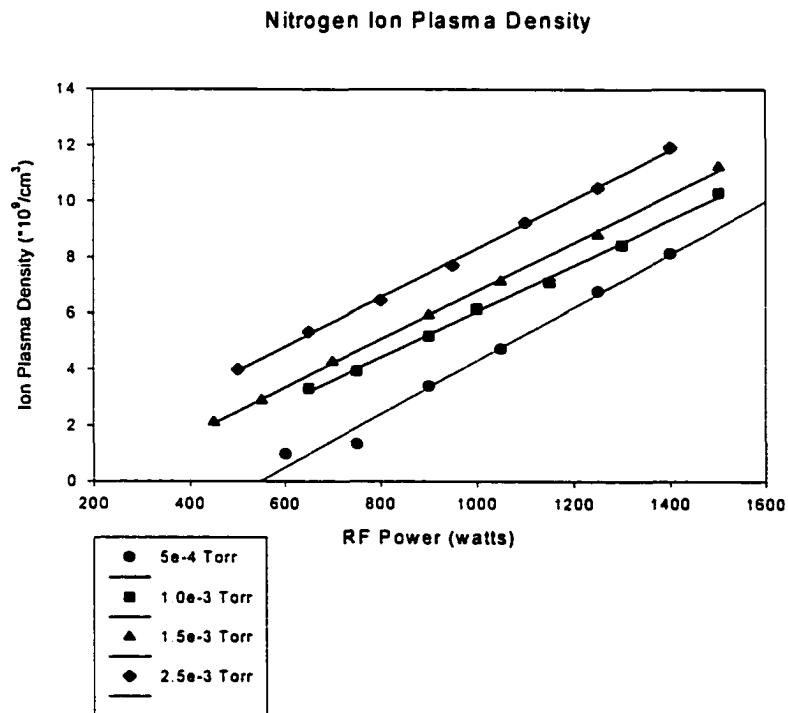
Figure 3.10. Ion plasma density for different rf power and nitrogen gas pressure with the magnetic congfinement.

Ion density versus RF power and Nitrogen pressure
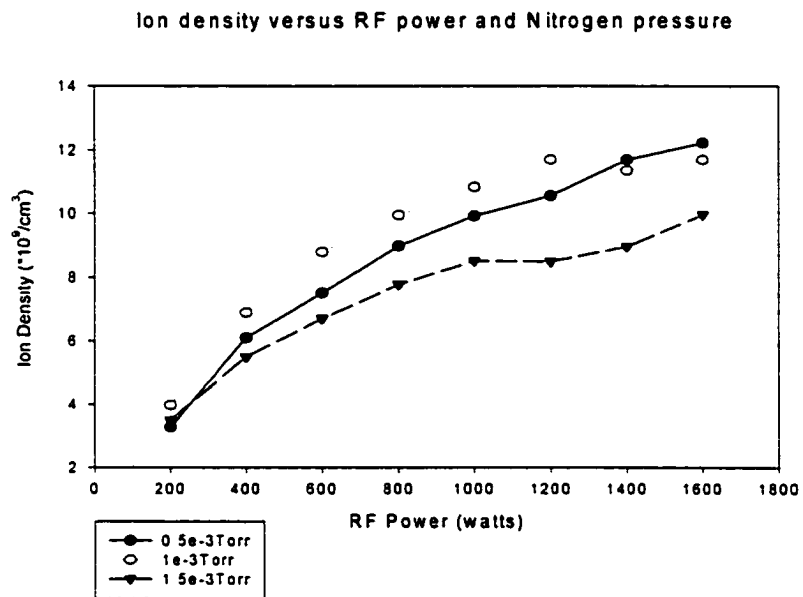
Figure 3.11. Ion plasma density obtained without magnetic confinement and Faraday shield for nitrogen plasma at differnt pressure and rf power. The probe was positioned 23 cm below the quartz window.

With the Faraday shield, the capacitive coupling fraction of our RFICP source is insignificant. This has been confirmed by surface analysis of implanted samples prepared using very long implantation times (see Chapter 7 on PSII of metals and semiconductor substrates). Previous studies also found that thick dielectric windows help to reduce the capacitive coupling between the coil and the plasma [17].

To initiate the discharge in the present RFICP system with large coil to plasma distance, hot filament and DC glow discharges are used. These discharges provide electrons and ions required. Typically, a filament voltage of $4V$ and current of $1.5A$, a bias voltage of $100V$ was enough to start the ICP discharge. Once the plasma is ignited, the hot filament and DC bias are not necessary to sustain the discharge.

3.4.2   Optical Emission Spectroscopy

It is important to understand the composition of the plasma in order to control the incoming ion energy and to determine proper dose for plasma source ion implantations. Atomic and molecular spectroscopy, which helped the development of quantum mechanics and the understanding of structure of matter, can provide such information [72, 73]. By studying spectra, and by measuring transition probabilities, we can chart the energy levels. This information can be used to identify species in the system. Depending on the energy, or wavelength of the radiation from the transitions, different experimental techniques are used, such as XPS, AES, x-ray spectroscopy, optical emission spectroscopy (OES), Raman, and FTIR.

Optical emission spectroscopy usually provides information about molecular vibrations, and the transitions between outer orbitals of atoms. It has been widely applied to the study of plasmas as an non-intrusive evaluation method. Spatially resolved OES has been used to study the different spatial distributions of various species in dc-magnetron sputtering discharges [74]. OES was also used to study the nitrogen species in the plasma used to perform surface nitriding of metal targets, in order to adjust the operation parameters and enhance the nitriding efficiency [75]. It was also used to study the influence of hydrogen on the density of molecular ions in dc and dc-pulse glow discharges [76].

In our work, nitrogen plasma optical emission spectroscopy was performed using a spectrometer equipped with 256×1024 CCD camera as a detector. Spectra were obtained through a 6-inch view port located 25.3 cm below the dielectric window. Three different gratings were used (300, 600, and 1200 grooves/mm) for survey scans and for detailed studies. The entrance slit was set to 6 μm for all the measurements, yielding a resolution full width at half maximum of 2 Å. The wavelength calibration of the gratings and the spectrograph were done using a mercury calibration lamp.

A typical spectra for the nitrogen plasma taken for 500 nm to 1000 nm range is shown in Fig. 3.12. An enlarged portion for 550 nm to 700 nm range is shown in Fig. 3.13. The prominent band structures appearing in this range belong to the first positive system $(B^3\Pi_g - A^3\Sigma_u^+)$ of neutral nitrogen molecules [77]. Table 3.1 below shows the respective initial and final vibrational states for the bands identified in Fig. 3.12 and Fig. 3.13.
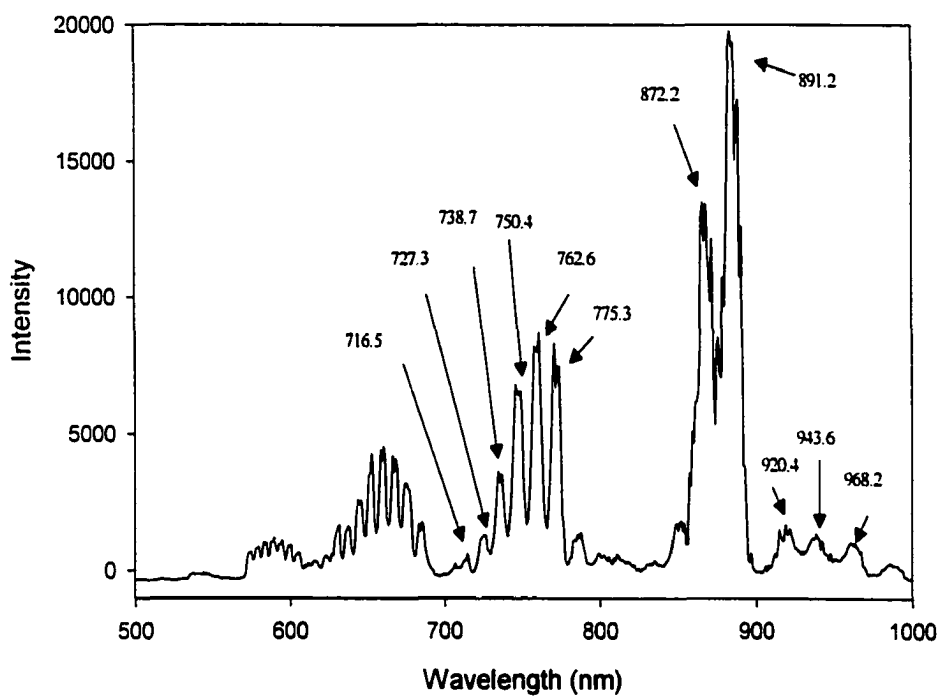
Figure 3.12. Optical emission spectrum taken from 500 nm to 1000 nm for nitrogen plasma of 2.5 × 10^{-3} Torr and rf power of 1200 watts. The prominent bands are identified to be belonging to the first positive system of neutral nitrogen molecules.

λ (nm)	v′	v″	λ (nm)	v′	v″
968.2	3	3	670.5	5	2
943.6	4	4	662.4	6	3
920.4	5	5	654.5	7	4
891.2	1	0	646.9	8	5
872.2	2	1	639.5	9	6
775.3	2	0	632.3	10	7
762.6	3	1	607.0	6	2
750.4	4	2	601.4	7	3
738.7	5	3	595.9	8	4
727.3	6	4	590.6	9	5
716.5	7	5	585.4	10	6
687.5	3	0	580.4	11	7
678.9	4	1	575.5	12	8

Table 3.1. The vibrational bands identified for the first positive system of excited nitrogen molecule [R. W. B. Pearse and A. G. Gaydon, The Identification of Molecular Spectra, Chapman and Hall, 1976]
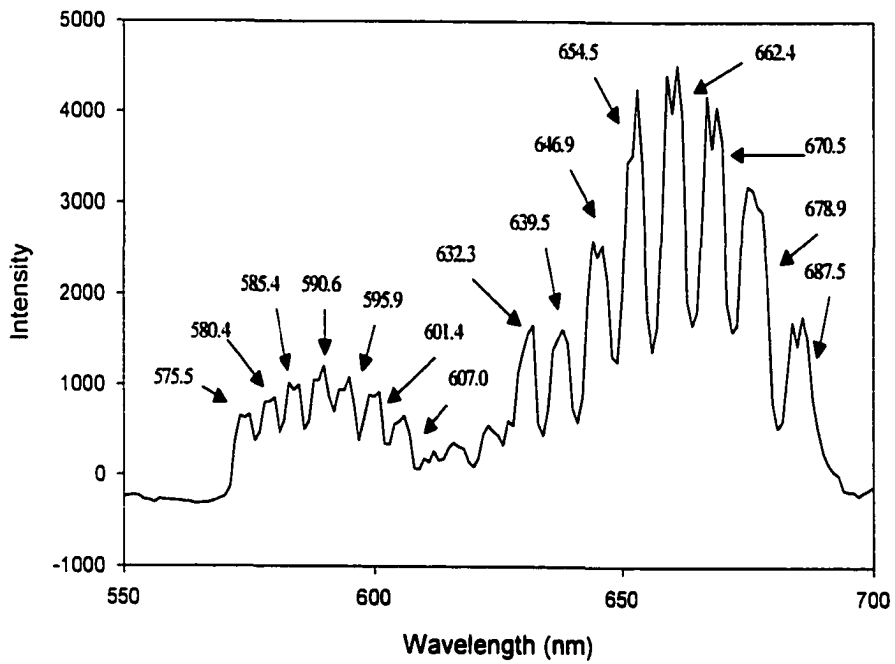
Figure 3.13. Optical emission spectrum for nitrogen plasma from 550 nm to 700 nm.

The N_2 second positive system ($C^3\Pi_u - B^3\Pi_g$) [77] was also detected and is shown in Fig. 3.14. The identified bands and the respective initial and final vibrational bands are shown in Table 3.2. There are several strong lines that do not belong to the second positive system. Detailed study around the 400 nm range reveals that these bands are from the first negative system ($B^2\Sigma_u^+ - X^2\Sigma_g^+$) of N_2^+, as shown in Fig. 3.15. Detailed study was also carried out around 740 nm. Atomic lines of atomic nitrogen were detected. A typical spectrum is shown in Fig. 3.16. The four strong, known N-atom lines identified are at 746.8 nm, 744.2 nm, 742.3 nm, and 740.6 nm.

OES results show that the dominant species in the large-scale RFI are excited nitrogen molecules, singly ionized nitrogen molecules, and atomic nitrogen. Lines for singly ionized nitrogen atoms were not detected in this study. A previous study used the N-atom 869 nm line for analysis of a high density nitrogen plasma [78]. The 869 nm line was not usable in this study due to strong presence of the overlapping band at 872.2 nm from the N_2 first positive system.

The degree of dissociation is directly dependent on the input power density. Blant and coworkers have reported that in very high density RFI plasmas in nitrogen, the dominant features belong to atomic nitrogen [78]. That study used a helical coil to surround a small discharge tube, 25 mm ID having a volume of 45 cm^3. The resulting rf power density in that tube was 13.3 $W\,cm^{-3}$. By contrast, the volume of our large PSII chamber is 0.149 m^3. With an rf power input of 1200 W, the rf power density is only 8.05×10^{-3} W / cm^3, more than three orders lower. In addition to the power density difference, helical and planar coil rf discharge have different spatial distributions. The electron energy distribution function

λ	v'	v''	λ	v'	v''
420.1	2	6	367.2	3	5
405.9	0	3	357.7	0	1
399.8	1	4	353.7	1	2
394.3	2	5	350.1	2	3
389.5	3	6	337.1	0	0
380.5	0	2	315.9	1	0
375.5	1	3	313.6	2	1
371.1	2	4	311.7	3	2

Table 3.2. The initial and final states of the vibrational bands identified for the second positive system of excited nitrogen molecule [R. W. B. Pearse and A. G. Gaydon, The Identification of Molecular Spectra, Chapman and Hall, 1976]

is very different in a small diameter discharge tube, in which diffusion to the wall is an important electron energy loss mechanism. In a large-volume chamber, such as the one used for the large-scale PSII, electron-ion recombination is much more important [76].

It is important to note that no SiO, SiO^+ or SiO_2 lines were detected, indicating that any sputtered contaminants from the quartz window were below the sensitivity of the spectrometer used. This was also confirmed by AES results of the implanted samples (see Chapter 7 on ion implantation by large scale RFI PSII), which showed no SiO_2 contamination.

3.4.3 Consideration of Sheath Size and Arcing for Plasma Source Immersion Ion Implantation

With the obtained experimental values of ion plasma density, the sheath size for plasma source immersion ion implantation was calculated for experiment design. Assuming that $n_i = 1 \times 10^{10}/cm^3$, the ion matrix sheath width can be calculated for a planar geometry by
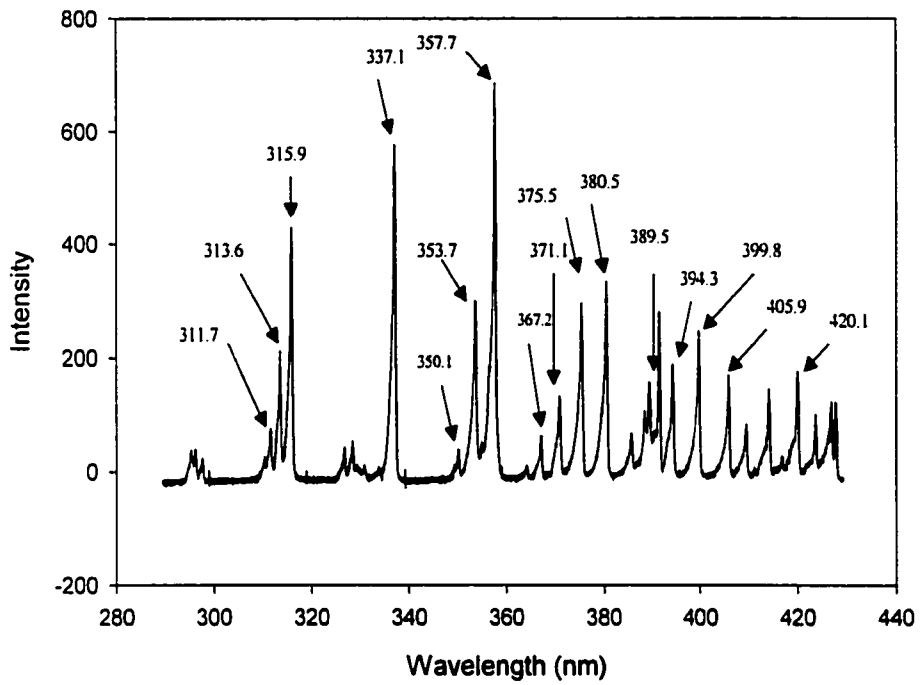
Figure 3.14. Second positive system for neutral nitrogen molecules detected from nitrogen plasma of 2.5×10^{-3} Torr and 1200 watts
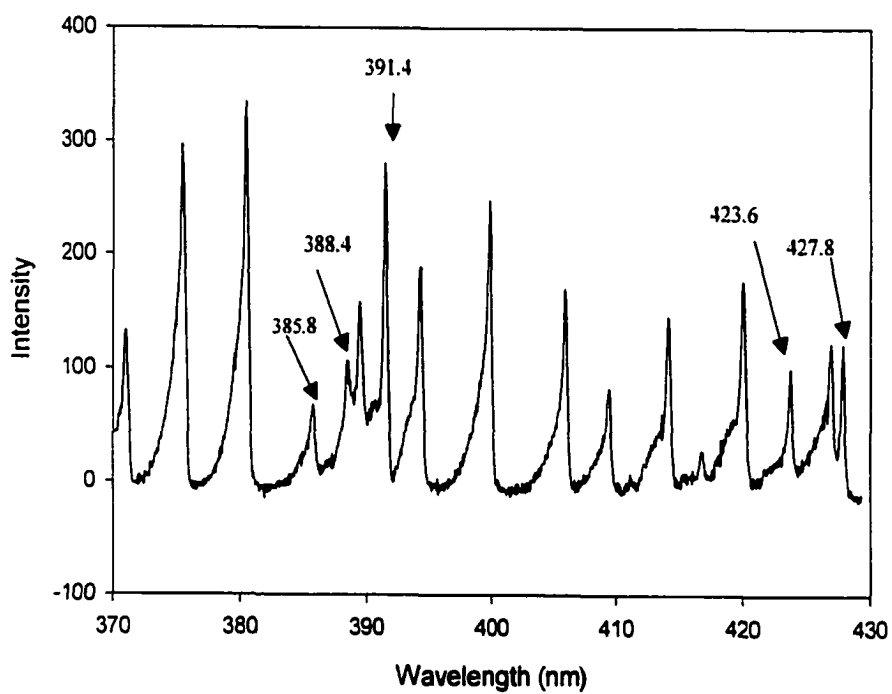
Figure 3.15. Identified bands for N_2^+ first negative system.
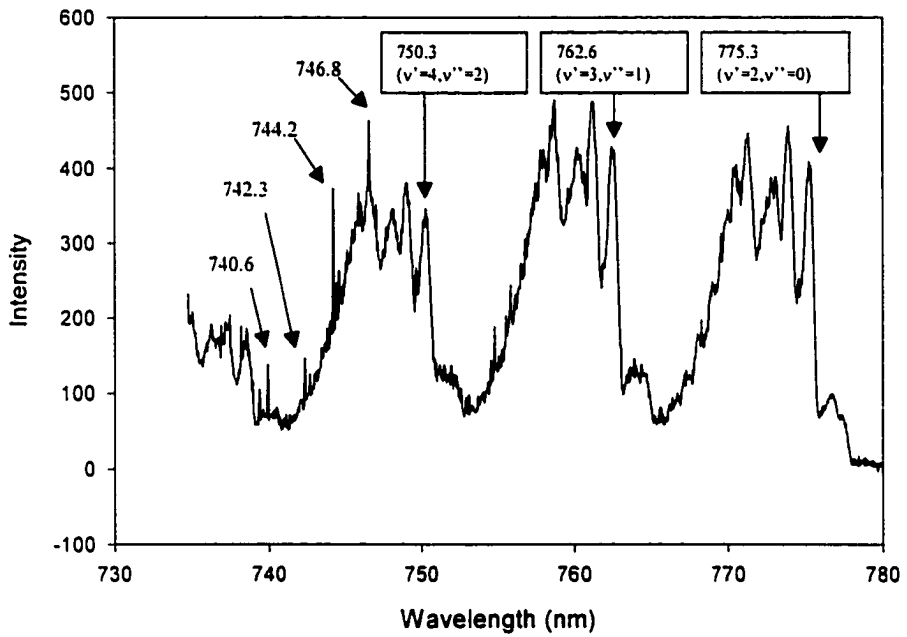
Figure 3.16. Sharp atomic lines from N^+ detected from a 2.5×10^{-3} Torr and 1200 watts nitrogen plasma. The vibrational bands of nitrogen first positive system are also labeled.

solving Poisson's equation, to yield:

$$s_0 = (\frac{2\epsilon_0 V_0}{e n_0})^{1/2} \qquad \text{(Eq. 3.13)}$$

It was found that $s_0 = 0.0182$ m for $V_0 = 30$ KV, $s_0 = 0.0235$ m for $V_0 = 50$ KV, and $S_0 = 0.0333$ m for $V_0 = 100$ KV, all insignificant compared to the target and chamber size used for our PSII system.

Understanding the temporal and spatial evolution of plasma sheath around real 3-D targets during PSII requires computer simulation solving Maxwell's equations and/or Poisson's equations (see Chapter 4 on MAGIC simulation). Sheridan et al. solved Poisson's equation numerically to calculate the expansion of the ion matrix sheath around a square bar [79]. A more comprehensive treatment has also been accomplished using a 2-D PIC simulation [80], for time-dependent sheath formation, depletion of the initial ion matrix, and for the expansion of the sheath into the ambient plasma. Such simulations are time-consuming and complicated, so for simple estimates for experiment design, 1-D analytical results are still widely used. The sheath width at the end of each pulse is an important factor for uniform ion implantation. During implantation, ion current depletion can be caused by overlapping of sheaths when multiple targets are installed, or by the sheath edge reaching the chamber wall. The calculations below can provide important parameters when large three-dimensional targets or multiple targets need to be implanted. The implantation chamber must be larger than the sum of the 3-D target size plus twice the maximum sheath width that develops within the applied pulse width. The distance between small samples should be larger than twice the maximum sheath width. Note, however, that a large chamber

is not always desirable because it requires more power input to maintain a plasma. As the

ions in the sheath are implanted, the sheath recedes and more ions are recovered from the

moving sheath edge. It was found that the sheath velocity for a planar target geometry can

be calculated by [12,81]

$$\frac{ds}{dt} = \frac{2}{9}\frac{s_0^2 u_0}{s^2} - u_B \qquad \text{(Eq. 3.14)}$$

where $u_0 = (\frac{2eV_0}{M})^{1/2}$ is the characteristic ion velocity and $u_B = (\frac{eT_e}{M})^{1/2}$ is the Bohm

(ion sound) speed. For the following calculations, T_e was chosen to be 4 eV, since the

electron temperature in most discharges is clamped in the range of $2 - 5$ eV by particle

balance [12].

Solving the above equation numerically for $V_0 = 100$ KV, the sheath edge position

in meters versus time in seconds is shown in Fig. 3.17. The steady-state sheath width was

found to be 0.234 m. It is 0.139 m for 50 KV and 0.095 m for 30 KV.

From the plot, we see that the sheath width is 0.19 m at $t = 20$ μs, which is the width

of the high voltage pulse used for the CWM PSII. Frequently, implantation voltages of 20

to 50 KV are used. Calculation shows that at $t = 20$ μs, $s = 0.12$ m for $V_0 = 50$ KV,

$s = 0.09$ m for $V_0 = 30$ KV. The implantation pulse width is usually adjusted to be shorter

than the time required for the sheath to reach the steady state Child law sheath thickness.

The sheath velocity was also calculated for 100 KV pulse and nitrogen ion plasma

density of $1 \times 10^{10}/cm^3$. As shown in Fig. 3.18, the sheath velocity decreases dramatically

with time, falling to near zero velocity around 60 μs, when the steady sheath width is
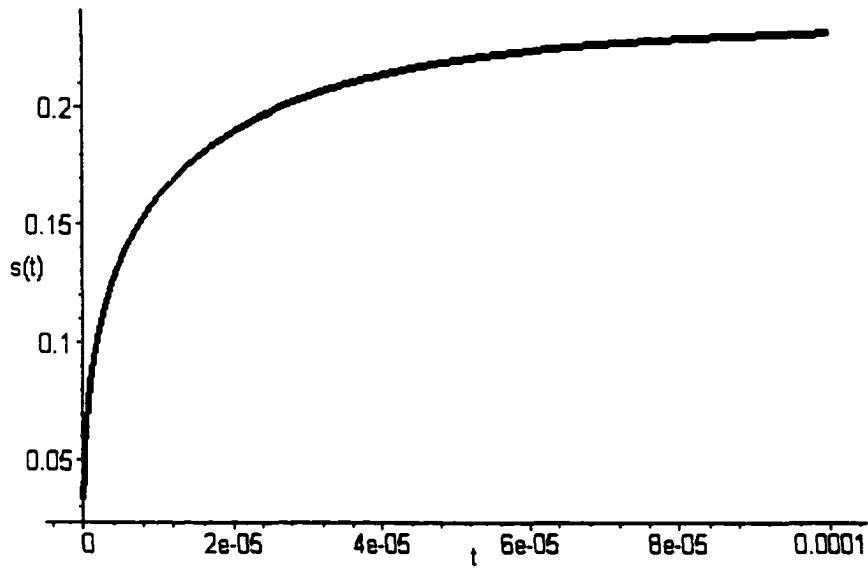
Figure 3.17. Sheath position as a function of time for plasma ion density of $1 \times 10^{10}/cm^3$. The electron temperature is 4 eV and the applied pulse voltage was 100 KV.

approached. Fig. 3.19 shows sheath velocity for the 20 μs to 200 μs range, calculated with the same parameters as used for Fig. 3.18.

Collisionless sheath conditions require the mean free path to be longer than the sheath width. Otherwise, the ions collide within the sheath, leading to reduced implantation energies and a broadened angular distribution of incoming ions, affecting the implantation over surface topography. The mean free path, λ, relates to the pressure by the expression $p \times \lambda = const$, where the constant is 6.1×10^{-3} Pa $\cdot$ m for nitrogen [81]. This condition gives a upper limit for the implantation pressure.

For a given implantation voltage, there is also an upper limit for the plasma density, relating to the maximum electrical field in the ion matrix sheath by [12, 81]:

$$E_{\max} = \left| \left(\frac{dV}{dx} \right)_{x=0} \right| = \sqrt{\frac{2V_0 e n_0}{\epsilon_0}} \qquad \text{(Eq. 3.15)}$$

The maximum electric field in the ion matrix sheath can not exceed a limit, which depends on the materials, the working gas, and a number of other factors, otherwise, arcing will occur. Arcing is highly undesirable for implantations on polished FEL electrode or on sensitive substrates. This upper limit is approximately 10 KV/mm for gas pressure lower than 1 Pa, although it also depends on the specific geometry and surface properties [81]. For the ion implantation process, this maximum field strength is reached at the beginning of each pulse, when the sheath is narrowest. Using the above equation, for a 100 KV pulse and for an ion plasma density of $10^{16}/m^3$, we calculate $E_{\max} = 6.01$ KV/mm, lower than the limit for arcing to occur. However, higher ion plasma density should not be used at such
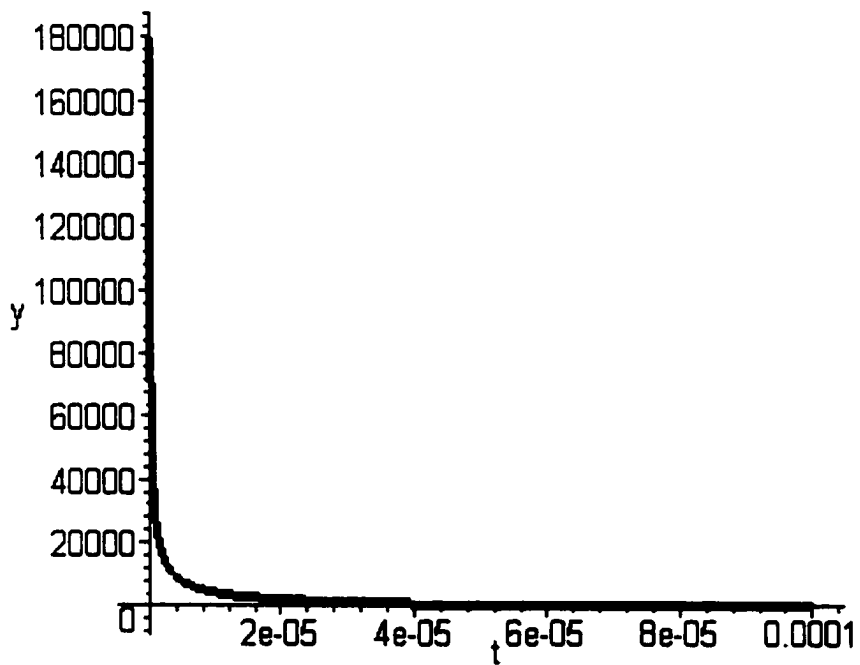
Figure 3.18. Sheath velocity calculated for nitrogen plasma ion density of $1 \times 10^{10}/cm^3$. The applied pulse voltage is 100 KV.
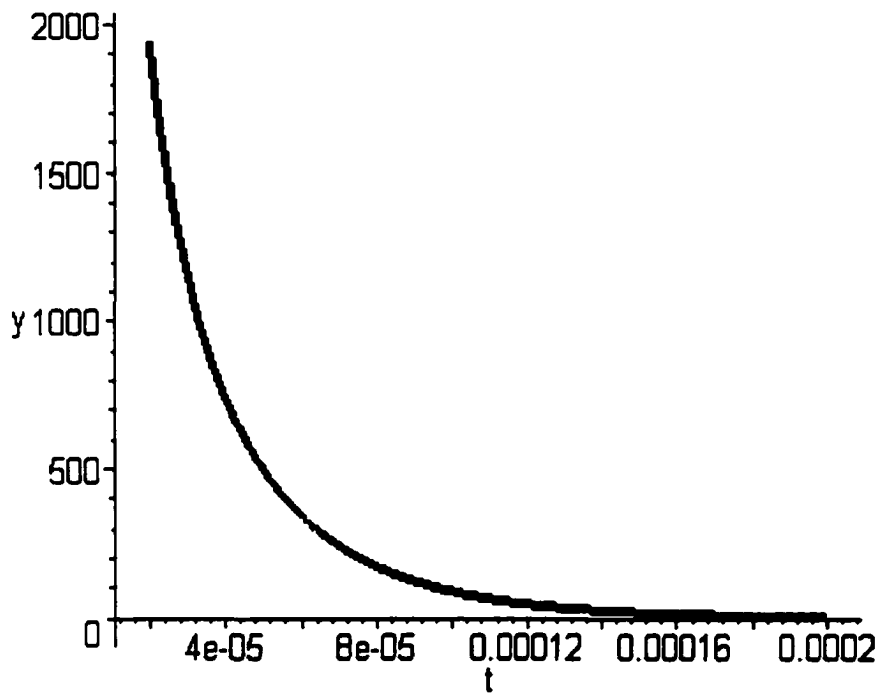
Figure 3.19. Sheath velocity calculated for nitrogen ion plasma density of $1 \times 10^{10}/cm^3$.
The pulse voltage used is 100 KV.

high implantation voltages if it is absolutely necessary to avoid arcing at the target surface,

thus we perform implants of polished targets at values lower than 100 KV in general.

Chapter 4

MAGIC Modeling of PSII Process

4.1   Introduction to PSII Modeling

Plasma source immersion ion implantation uses a plasma of the species to be implanted as the ion source. Instead of continuous acceleration voltage, a train of high voltage negative pulses, typically $1 - 100$ KeV, $1 - 50\mu m$ long, are applied to the target immersed in the plasma. The positive ions in the plasma are accelerated toward the target surface during each pulse. The implantation dose distribution has been found to be strongly dependent of plasma sheath distribution, plasma ion density distribution, and local electromagnetic field distribution.

Shamim, et al., have studied the distribution of incident ions and retained dose for a wedge-shaped target in plasma source immersed ion implantation [82]. It was found that there was enhanced sputtering, less retained dose, and a shallower penetration range of implanted ions in the vicinity of the acute angle edges as compared to square angle edges. They also found that a smaller wedge face retained a higher average dose than a face with larger area. The dose difference was thought possibly to be due to the stopping of the sheath

89

at different positions and to the difference in ionization rates of neutrals inside the sheath due to different electric field intensities. Spatial and temporal sheath evolution of plasma sheath for spherical and cylindrical geometries has also been measured and compared to the calculations using the quasistatic Child-Langmuir approximation [12,83].

Scheuer, et al., also developed analytical models for planar, cylindrical, and spherical geometries, assuming that the transient sheath obeys the Child-Langmuir law for space-charge-limited emission at each instant during the propagation of the sheath, predicting the sheath-edge position as a function of time, the final sheath extent, and average ion current to the target during each pulse [84]. In contrast to the model proposed by Lieberman for planar geometry [12] , they assumed that an ion does not drift toward the target at the ion acoustic speed prior to its propagating sheath, but rather has zero velocity until the sheath edge reaches it. Scheuer argues that this is a more realistic model in the case of a fast sheath since the presheath dose not have time to form before the sheath reaches a given point. Later work used a one dimensional analytic model of dynamic sheath expansion to develop a pseudo 2-D model [85].

Sheridan, et al., also simulated the ion matrix sheath surrounding a square bar and the determined equipotential lines by solving Poisson's equations, providing 2-D sheath distribution for PSII [79]. Another study also predicted equipotential evolution and dose distribution by solving Poisson's equations for a cylindrical geometry [86], using finite difference method. Wang, et al., have developed a Monte Carlo simulation model to determine the energy and angle distributions of ions incident on a spherical target during the sheath edge expansion in higher pressure regime for PSII [87]. The group at Los Alamos [80] also

used PIC codes to study the sheath distribution and implantation dose distribution for long rod and bore geometries. Paulus, et al., also used a PIC code to solve Poisson's equations around two simple shapes for ion current density, average impact energy, and other related information [88].

These previous modelers were successful in providing information for some aspects of PSII, such as implantation dose for each pulse for simple geometries [84], sheath distribution for simple, symmetric geometries [84], and equipotential lines [79]. One of the studies provided ion energy and angle distributions [87]. However, none of the simulations were capable of providing all of the relevant and important information for PSII, such as matrix sheath distribution, Child-Langmuir law sheath evolution, electromagnetic field distribution, equipotential lines distribution, ion trajectories across the sheath, and the ion flux distribution. Because of their choices of computational methods or the simplifying assumptions made in these studies, it was not possible to provide information for more complex 2D or 3D geometries.

PSII simulation using the MAGIC Code is presented in this Chapter. MAGIC is an electromagnetic particle-in-cell, finite difference, time-domain code that solves Maxwell's equations and Lorentz force equations. The user can choose 2-D or 3-D geometry according to the needs of the simulation. We found it successful in providing crucial information for PSII, and much easier to use because of its ability to easily handle different geometries and because the outputs are user-configurable. The plasma tool box eliminates the need for detailed low level programming. Details are presented in the following sections.

4.2 Modeling of PSII Process

4.2.1 Collisionless Model of PSII Process

Analytical models of planar collisionless sheath for the plasma source ion implantation process [12,84] have been widely used to help understand the basic plasma physics process, such as sheath formation and evolution. Such one-dimensional analytical models predict the sheath evolution and implantation current density as a function of time. To accelerate ions in the plasma to sufficiently high energy and to achieve narrow energy distribution, low processing pressure is usually used for PSII. Here a quick introduction to the collisionless model is given, which will be useful later to interpret the modeling results from MAGIC.

The planar PSII geometry is shown in Fig. 4.1. At time $t = 0$, a voltage pulse of amplitude $-V_0$ is applied to the target, which drives away the electrons in the plasma to form a matrix sheath, which has a width determined by the amplitude of the voltage and the plasma characteristics:

$$s_0 = (\frac{2\epsilon_0 V_0}{en_0})^{1/2}$$ (Eq. 4.1)

It is assumed that the ion flow is collisionless and the electron motion is inertia-less. The applied voltage V_0 is much greater than the electron temperature T_e, so that the Debye length $\lambda_{De} \ll s_0$ and the sheath edge at s is sharp.

A quasistatic Child Law sheath forms as the ions in the matrix sheath are being implanted [12,84]. The current demanded by this sheath is supplied by uncovering of ions at the moving sheath edge and by the drift of ions toward the target. During the motion of an
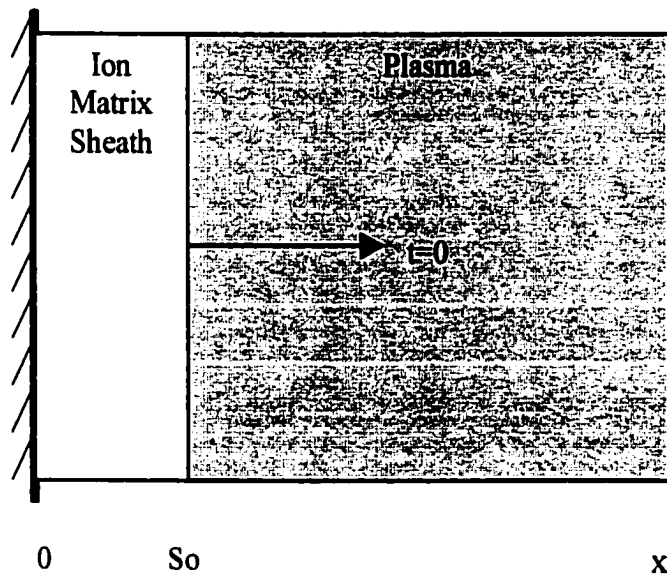
Figure 4.1. Planar geometry showing the formation of ion matrix sheath.

ion across the sheath, it is also assumed that the electric field is frozen at its initial value, independent of time, except for the change in field due to the velocity of the moving sheath. These two assumptions permit an analytical solution be obtained for the sheath movement and are justified post-hoc by comparisons with numerical results. The steady state Child law sheath thickness is

$$s_c = s_0 (\frac{2}{9} \frac{u_0}{u_B})^{1/2}$$ (Eq. 4.2)

. where $u_0 = (2eV_0/M)^{1/2}$ and $u_B = (eT_e/M)^{1/2}$.

The sheath thickness can also be expressed as

$$s = s_0 ((2/3)\omega_{pi} t + 1)^{1/3}$$ (Eq. 4.3)

where

$$\omega_{pi} = (\frac{e^2 n_0}{\epsilon_0 M})^{1/2}$$ (Eq. 4.4)

This result (Eq. 4.3) can be obtained by assuming that the drift velocity of ions toward the target is zero [84]. This assumption is also supported by experimental results of time-resolved Langmuir probe measurements, showing the presheath was suppressed for supersonic moving sheaths [89]. If the ions are assumed to have a drift speed of u_B toward the target, the same expression can also be obtained [12].

4.2.2   Modeling of PSII Process

Plasma simulation computes the interaction of charged particles with electrical and magnetic fields. In principle, direct integration of the Maxwell's equations and the Lorentz force equations should solve any electromagnetic problem and determine its dynamic behavior. Most often, a plasma exhibits complex nonlinear behavior and the field and particles interact with time-dependent boundary conditions. Usually, there are billions or perhaps trillions of particles per cubic centimeter for even a low-density plasma, which makes the simulation very computationally intensive [90].

Historically, computational plasma physicists wrote codes in structured languages such as Fortran and C. These codes often have 10^4 to 10^6 lines of code not including the user interface [90]. These "legacy" codes can often trace their origin to the 1960s or 1970s. They were programmed to solve specific and specialized problems, requiring experts to run and maintain them. Such codes are difficult to upgrade because of the close coupling of their structure and solution techniques, thus modular upgrading is difficult or impossible. Many times, the code developer was the only one who could run and maintain these codes.

4.3   Introduction to MAGIC Code

MAGIC Code is an electromagnetic particle-in-cell, finite difference, time-domain code that solves Maxwell's equations and the Lorentz force equations. Maxwell's time-dependent equations are solved to obtain electromagnetic fields and the Lorentz equation is solved to obtain particle trajectories. Meanwhile, the continuity equation is solved to provide current

and charge densities for Maxwell's equations [91]. MAGIC successfully integrated many useful PIC techniques, enabling the user to address different geometries and boundaries, materials, particle emission models, to interpret voluminous and abstract modeling output, and sometimes to integrate with other software in a design environment. Consequently, it has been used for the modeling in many areas, including antennas, sensors, Lasers, beam propagation, plasma heating, ion sources, and field emitter arrays [92].

MAGIC works like a tool-box for the user to configure the proper system geometry, materials combination, boundary conditions, field algorithms, particle algorithms, and output requirements. It represents the fields on a finite-difference grid. Particles are represented using the particle-in-cell approach, representing a large number of physical particles of the same species by virtual particles or macro particles. A variety of algorithms for particle kinematics and current density allocation are individually optimized for different density, velocity, and field strength [92].

4.4   MAGIC Modeling of PSII Process

Usually, large time steps and a small number of particles are desirable to reduce simulation costs. However, the choice of particle number is limited by the spatial resolution needed for the simulation. For the ion implantation process we are studying, the actual pulse width is ~10 μs. To show the trend and proper statistics for the physics, we have to opt for a long simulation time. However, when simulating the implantation of small geometric features on a large piece of substrate in a large-scale implantation chamber, using a large virtual par-

ticle numbers and long simulation times makes the modeling computationally intensive. To improve the spatial resolution of the simulation for small geometric features, it is important to choose the finest possible grid for the space around those features. However, the combination of these demands (fine grids, large virtual particle numbers, and long simulation times) can cause the simulation to crash. Successful execution of simulation require careful consideration of the desirable resolution, proper statistics, and acceptable computational cost. Most of the time, a compromise of these factors is required.

In the simulations reported here, the ion plasma density was assumed to be $1 \times 10^{10}/cm^3$. The initial ion and electron distributions were assumed to be uniform. The electron temperature was taken to be 4 eV [12]. The positive ions were singly ionized nitrogen molecules (see Chapter 3 on RFI source designing and characterization). The positive ions were created cold ($T_i < 0.5\ eV$) and then accelerated by a high voltage negative pulse of 100 KV. Using a discrete time step of 12.3 ps, the pulse was applied at $t_0 = 2$ ns, with a linear rise time of 0.1 ns. For all simulations with a large implantation chamber, the HV pulse was applied to the sample stage using the PORT command, from an opening at the bottom of the chamber. The simulated targets were placed on a 5 in. i.d. and 1 in. thick conducting plate, supported by, and insulated, from the chamber bottom by a hollow quartz ring (see MAGIC output graphs in following sections for more details).

The chamber and the sample stage geometry included in the models are assumed to be azimuthally symmetric. Thus only a 2-D half-plane cut is necessary for full simulation. The chamber simulated is 0.71 m ID, 0.61 m tall.

4.4.1 Potential Structure, Field Distribution, Ion and Electron Distribution

MAGIC modeling results of several geometries are presented in this section, providing information about sheath evolution, field distribution, and equipotential distribution. These results are compared to other modelings to show the advantages of MAGIC modeling.

Field distribution and/or equipotential lines determine the ion trajectory across the sheath, thus determine the implantation energy, incident angle, sputtering rate, dose distribution, and the retained dose on the target. Sheridan, et al., calculated the ion matrix sheath around a square bar solving Poisson's equations and obtained equipotential and field lines [79], which closely follow those found for a cylindrical electrode. The equipotential lines followed the structure of the bigger square bar better.

We modeled the sheath evolution around a long cylinder sitting on the sample stage as a benchmark. The electron distribution at $T = 110.070 \; ns$ is illustrated in Fig. 4.2, showing a well-defined sheath edge after the pulse rise-time transients have decayed [80]. The sheath surrounding the 1 in. i.d., 11 in. long conducting cylinder is greatly influenced by the presence of the sample stage. The sheath around the middle of the cylinder is almost cylindrical. However, the sample stage pushes the sheath away from the bottom of the cylinder, resulting in larger sheath width. The sheath surrounding the top of the cylinder resembles a half dome. The sheath edges are rounded (not showing sharp corners) and follow the contours of the target assembly. The sheath width slightly decreases as it approaches the top of the cylinder. This behavior is consistent with the results of previous models [79].

Time 110.070 ns: PHASESPACE for ELECTRON   Q/M Ratio: -1.759E+11
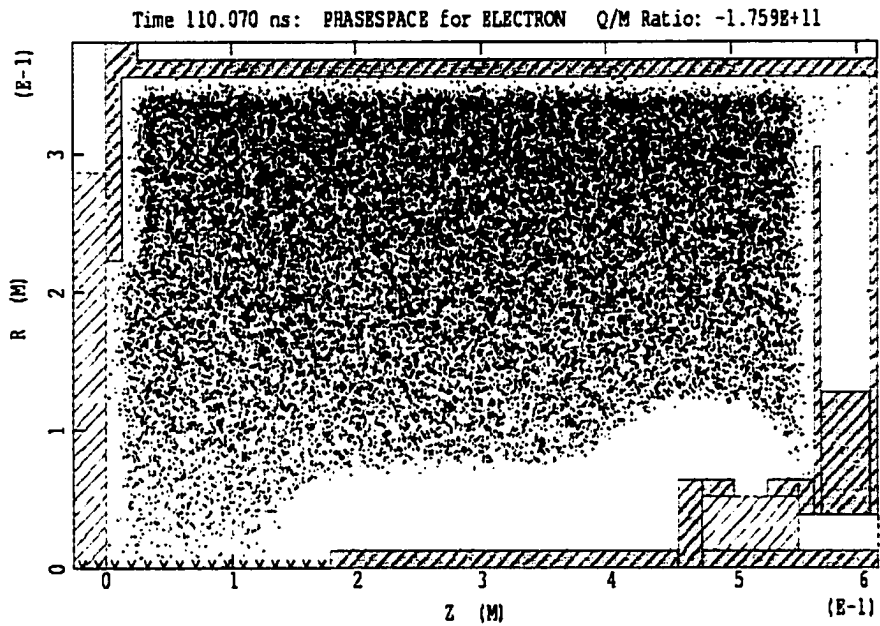
Figure 4.2. The plasma sheath distribution at $T = 110.070$ ns for a negative voltage starting at $T_0 = 2$ ns. The long cylindrical target was sitting on the sample stage, at the center of the cylindrial chamber.

The field distribution for the same setup is shown in Fig. 4.3. The length of the arrows are proportional to the field strength. The electric field converges at the top corner of the cylinder and at the edges of the sample stage, confirming previous models [79] and previous experimental measurements [82]. The electric field is weaker where the cylinder meets the stage. The electric field is perpendicular to most of the cylinder surface. The equipotential lines are also shown in Fig. 4.4. Equipotential lines are more rounded as the distance of the line from the cylinder increases. The equipotential lines are parallel to the side of cylinder, except at the top edge, and at the corner where the cylinder and the stage join. The electric field is weaker in areas with sparse equipotential lines.

The positive ion distribution at $T_0 = 105.066$ *ns* is shown in Fig. 4.5. The ion flow is substantially laminar along the side of the cylinder. Ion focusing is apparent for the top of the cylinder. The ion flux is not focused to the edge of the cylinder top, but rather to two annular zones close to the edge, one on the top of the cylinder and the other on the side of the cylinder. This effect was observed in previous experiments [82], and has been obtained by previous PIC models [79, 80]. The two smaller surfaces receive higher flux because of the more focused electrical fields there. Similar results have been reported when the dose distribution on a wedge-shaped implanted target was analyzed [82].

The electron and ion trajectories were also studied by making MAGIC "movies", showing the electron/ion distributions, field distribution, and equipotential lines distribution at a series of time intervals, to study the trend of the process and to decide when a steady state is reached for the implantation. By watching the movie made for the implantation of the long cylinder, we found that the ions strike the edge of the cylinder top and the edge of

Time 100.062 ns: Vector plot of (Ez,Erho)
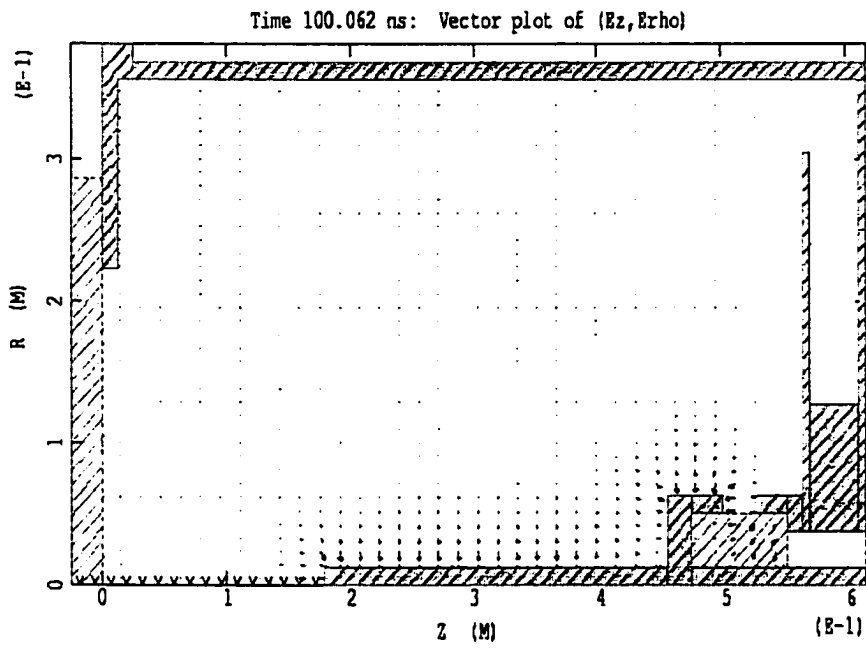
Figure 4.3. Electrical field distribution at $T = 100.062\ ns$.
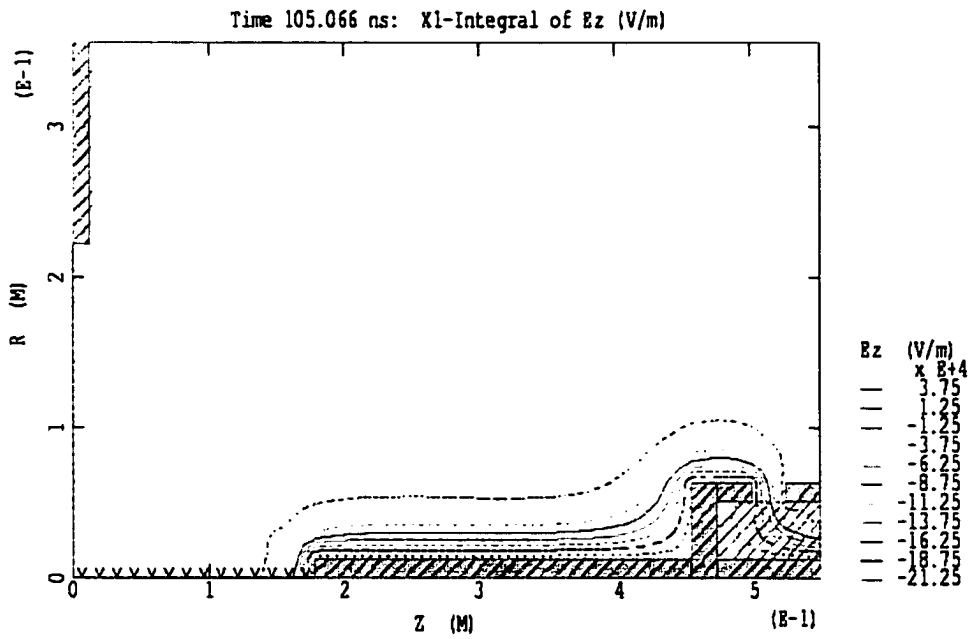
Figure 4.4. Equipotential lines at $T = 105.066\ ns$.

Time 105.066 ns: PHASESPACE for NITROGENMOLECULE   Q/M Ratio: 3.446E+06
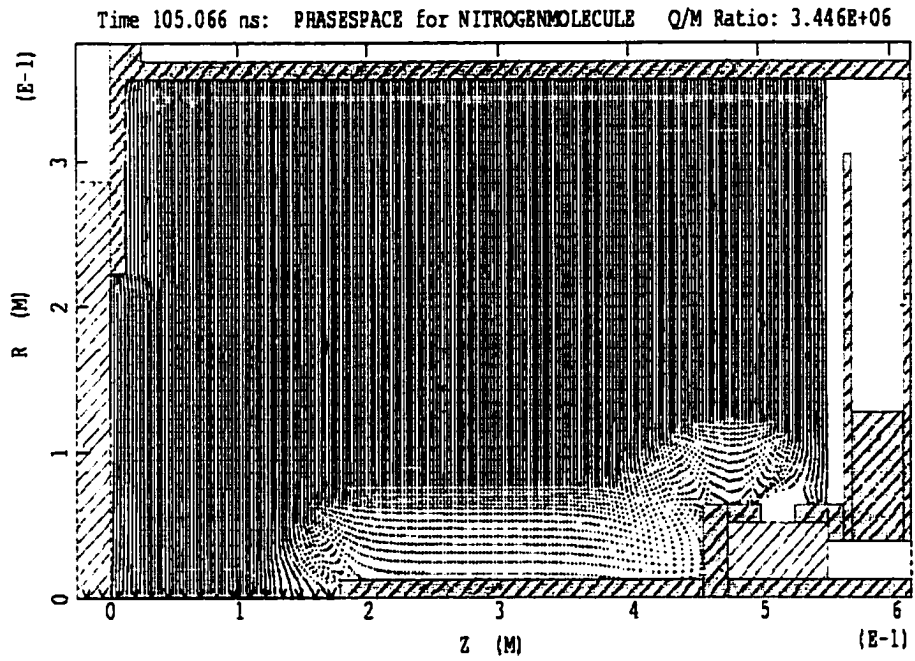
Figure 4.5. Plasma ion distribution at $T = 105.066$ ns, showing laminar structure near the side of the long cylinder and focusing near the edges.

the sample stage at shallow angles, which causes more sputtering of the surface, shallower implantation depth, and a lower retained implantation dose [12], even though the incoming fluxes to these areas are higher.

This information can be easily extracted from calculations for different geometries. We have modeled a thin plate, 23 in. i.d. and 0.5 in. thick, sitting on the stage. The results for electrical field distribution, equipotential lines, electron distribution, and nitrogen ion distribution are shown in Fig. 4.6, Fig. 4.7, Fig. 4.8, and Fig. 4.9. As shown in Fig. 4.6, the electric field is very uniform and is perpendicular to the plate surface, except for areas near the edge, where the field converges to the side of the plate. The apparent laminar flow of the nitrogen ions is seen in Fig. 4.9 for the plate top and for most of the bottom side. There are three annular zones near the plate edge which receive more ion flux, one on the side, one on the top, and one on the bottom, caused by the local convergence of the electric field. As mentioned above, the equipotential lines with smaller distance to the plate and/or the stage follow the surface profile of the target assembly more closely (Fig. 4.7). The sheath is more uniform for the plate top and is parallel to the plate surface.

Another geometry modeled and shown here is a 23 in.dia., 4.5 in. thick plate with a 2 in.dia., and 4 in. deep hole in the center. Only the electron and ion distributions are shown here (Fig. 4.10 and Fig. 4.11). There is apparent overlapping of the sheath with chamber wall. Compared to the 0.5 in. thick plate above, there is less ion flux focusing since the plate is thicker and therefore presents a larger surface area [82]. The laminar ion flow is obvious for the top, the bottom, and the side of the plate. The sheath width at the edge of the plate is smaller. In addition, there are some interesting focusing effects shown

Time 109.947 ns: Vector plot of (Ez,Erho)
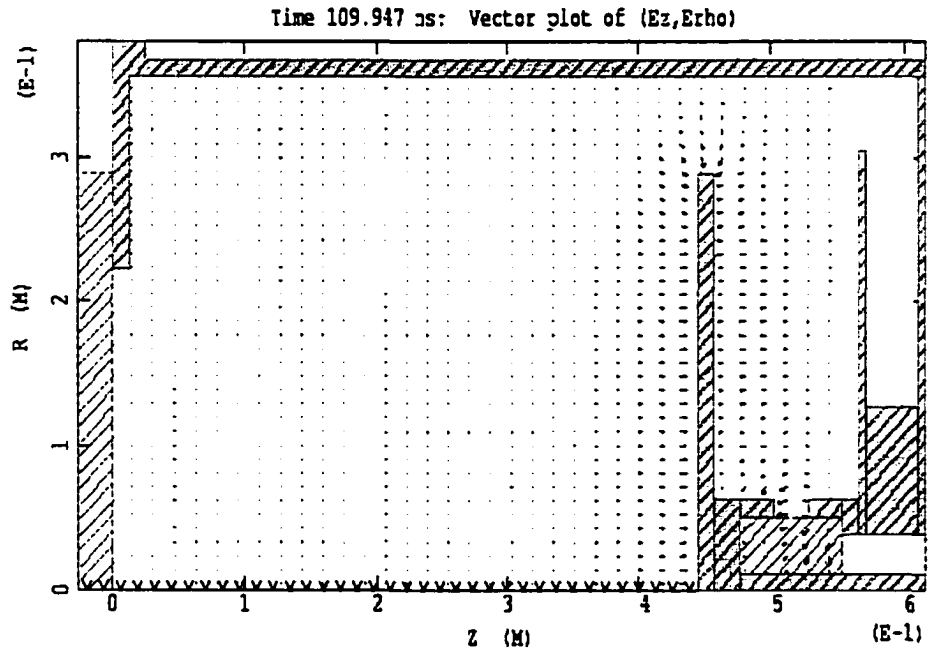
Figure 4.6. Electric field distribution at $T = 109.947\ ns$.
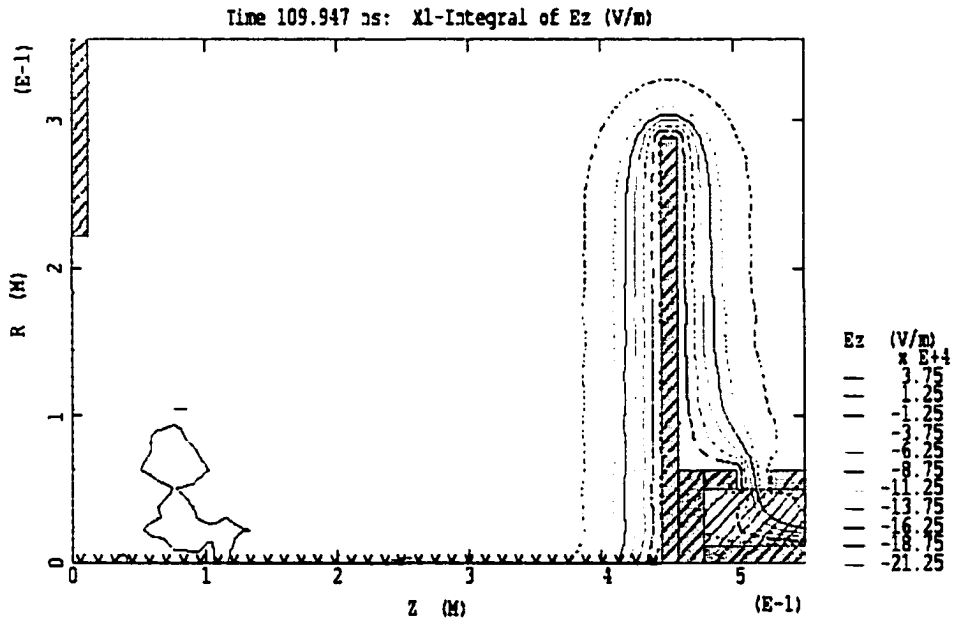
Figure 4.7. Equipotential lines distribution at $T = 109.947\ ns$.
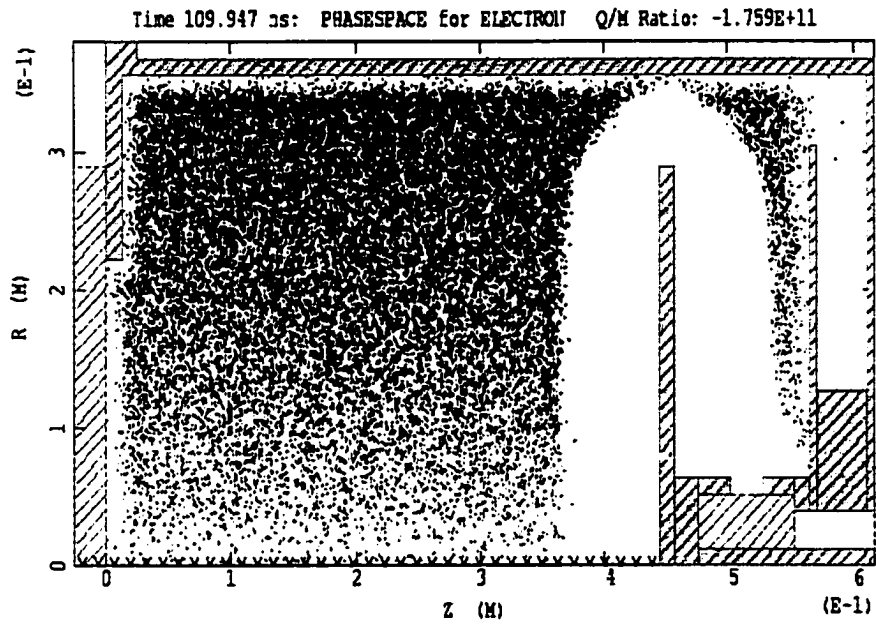
Figure 4.8. Electron distribution at $T = 109.947 \ ns$.

Time 109.947 ns: PHASESPACE for NITROGENMOLECULE   Q/M Ratio: 3.446E+06
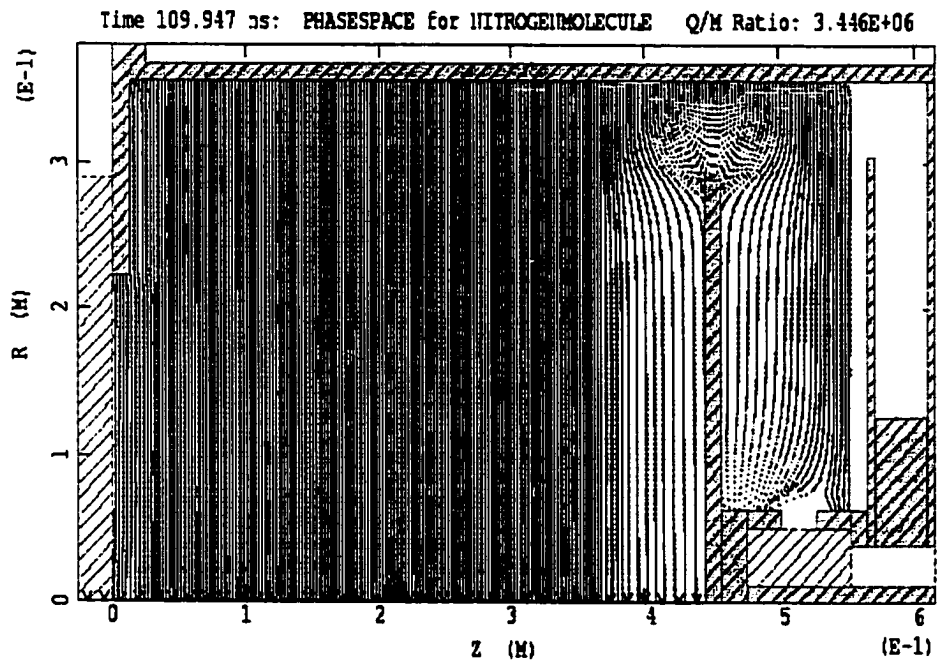
Figure 4.9. Nitrogen ion distribution at $T = 109.947$ ns.

near the side wall of the center hole, which will be discussed in more detail in next section.

It is seen that the obtained sheath distribution (Fig. 4.10) is very similar to that obtained in

previous studies of a similar geometry using PIC codes [80].

According to Eq. 4.3, the sheath width for planar geometry at $T = 109.947\ ns$

$$s = s_0((2/3)\omega_{pi}t + 1)^{1/3} = 0.047\,\text{m} \qquad\qquad \text{(Eq. 4.5)}$$

The observed sheath widths for the top of the thin plate was $0.075\ m$ at $T = 109.947$

ns. The same value was obtained for the 23 in.dia., 4.5 in. thick, plate with a center hole.

The sheath width surrounding the side of the long cylinder (Fig. 4.2, uniform part) was 0.06

m. These snapshots of sheath distribution were taken at slightly different times, however,

the effect on the sheath width is negligible. The results show that a thickness difference of

3 inches does not have significant influence on the sheath width on the plate top. The thin

plate thus can be considered to have a planar geometry since its thickness is much smaller

than its diameter. However, the sheath width for plate top is much larger than that predicted

by planar analytical model. The sheath width for the side of the long cylinder is smaller

than that for the thin plate. Both are larger than the prediction of the analytic model for

planar geometry.

4.4.2   Ion Flux Distribution

The ion flux distribution inside a 2 in. diameter center hole in a 20 in. diameter cylinder

was modeled, using the option provided by MAGIC to monitor ion flux at any location

in the simulated space. A simulation time of $2.5 \times 10^{-7}s$ was used for each hole depth,

Time 109.947 ns: PHASESPACE for ELECTRON   Q/M Ratio: -1.759E+11
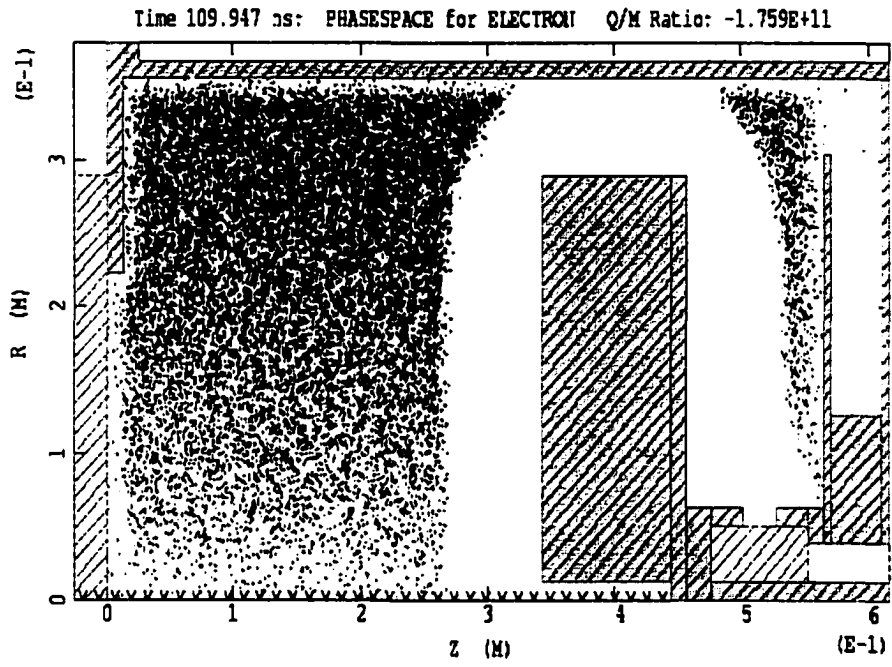
Figure 4.10. Sheath distribution at $T = 109.947$ ns.

Time 109.947 ns: PHASESPACE for NITROGENMOLECULE   Q/M Ratio: 3.446E+06
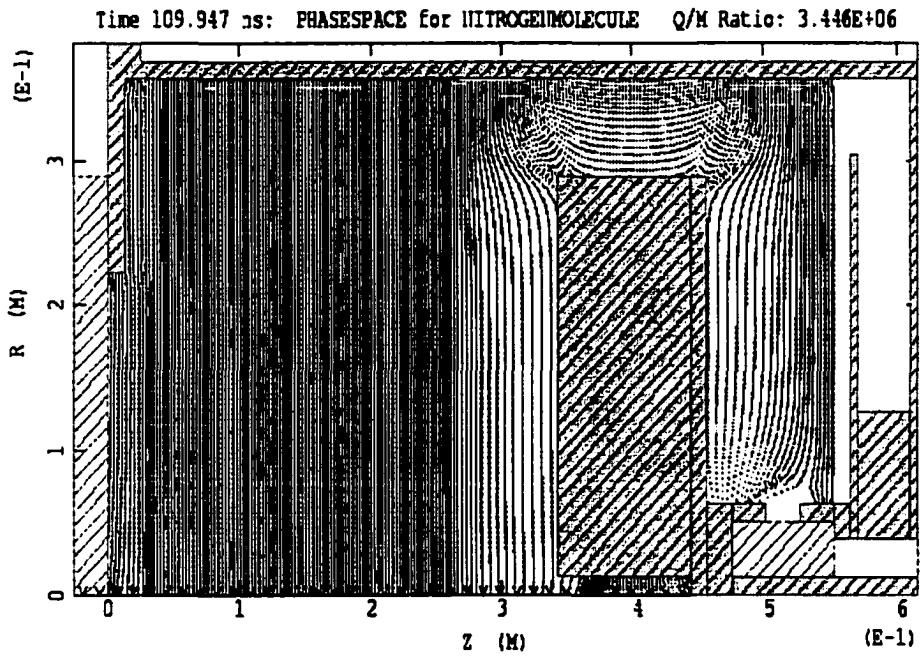
Figure 4.11. Nitrogen ion distribution at $T = 109.947\ ns$.

representing the initiation of a quasi-steady state lasting throughout the pulse. The ion flux

on the side wall and on the bottom of the hole was monitored and the accumulated total ion

fluxes were output as functions of spatial location. The definitions of hole depth and radial

position are shown in Fig. 4.12. Three different hole depths were used for comparison. Fig.

4.13 indicates that the bottom of the deeper holes received much less ion flux, although

with better spatial uniformity. The ion flux distributions for the walls are shown in Fig.

4.14. The ion flux focusing effect found in Fig. 4.11 is confirmed by the maximum of the

ion flux distributions, located 4 cm away from the opening of both the 4-inch deep hole

and the 8-inch deep hole. The accumulated total flux for the wall of the 8-inch deep hole is

larger than that of the 4-inch deep hole, probably from reflected ions that could not reach

the bottom, where the total flux is smaller than that of the 4-inch deep hole. On the other

hand, the focusing effect is not found for the 2-inch deep hole, which has the highest total

flux for the bottom, due to the lower depth to radius aspect ratio.

The cases for side walls joining the bottom at a angle less than 90 degrees are also

modeled for dose distributions. The depth is 2 in. for both. The radii of the bottom are 1

in. and 1.5 in. respectively. The angle of the side wall is 45 degrees for the 1-inch hole

and 53 degrees for the 1.5-inch hole. The locations for flux monitoring are shown in Fig.

4.15. The flux distributions for the bottom with a $2.5 \times 10^{-7}s$ modeling time are shown

in Fig. 4.16, indicating higher fluxes for the centers and for the 1.5-inch hole. The flux

distributions for the side walls are shown in Fig. 4.17, both decreasing monotonically from

the top to the bottom. The bottom of the 53 degree wall received much less flux than that of
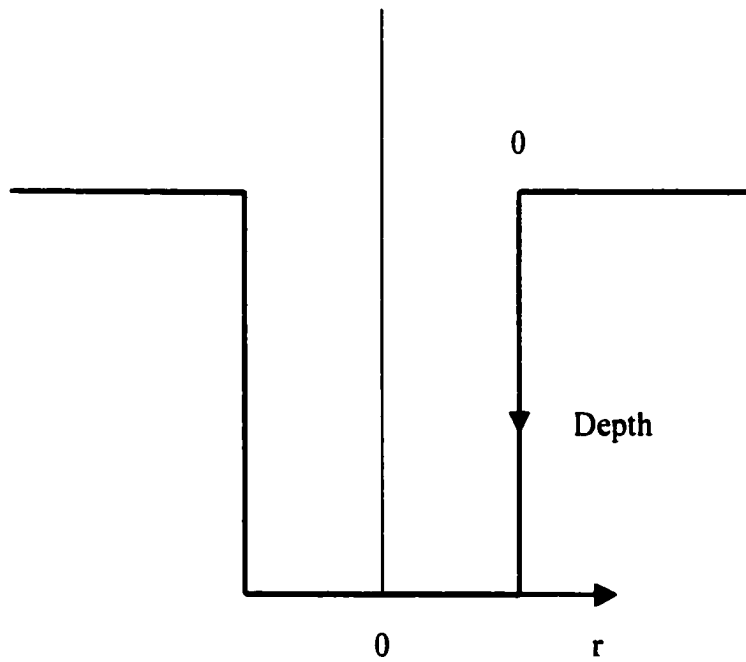
Figure 4.12. The definations of the radial location and depth for a hole for ion flux monitoring.
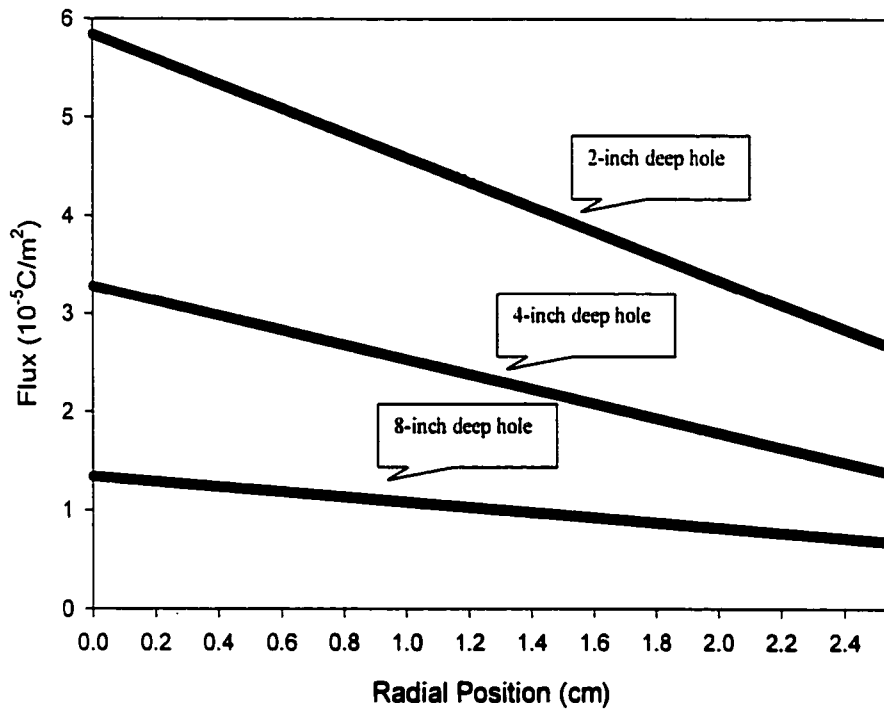
Figure 4.13. Accumulated total ion flux distributions for the bottoms of the holes.
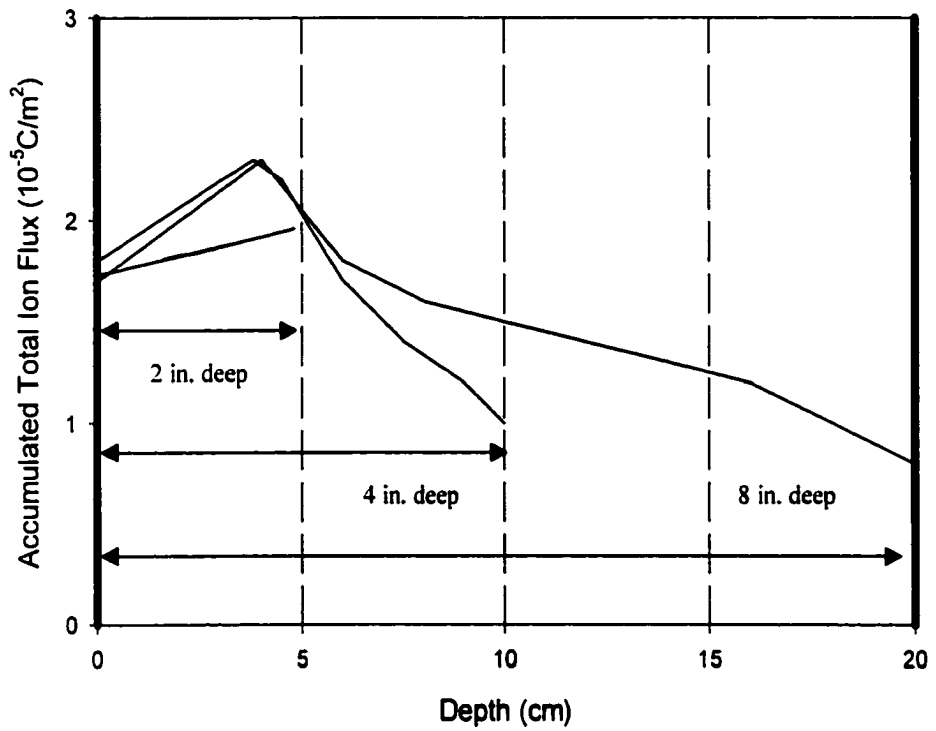
Figure 4.14. The accumulated total ion flux distributions on the walls of three holes.

the 45 degree wall. These results are consistent with the TEM results of a implanted trench presented in Chapter 5.

4.5 Summary

The MAGIC Code was successfully applied to model PSII process. With the many successfully integrated PIC techniques of MAGIC Code, the modeling addressed different geometries and boundaries, materials, plasma parameters, illustrated sheath formation and evolution, field distribution, ion and electron trajectories, for critical informations, such as ion incident angles and dose distribution, which are important for PSII experiment design and for the understanding of the PSII process. The results presented here compared favorably with experimental results and simulations from previous modelings by other groups. MAGIC modeling is advantageous compared to 1-D or pseudo 2-D analytical models, for its 3-D and user-configurable multiple information output capability. It is also more convenient and more efficient to perform than working on low-level PIC code development or modification of legacy code of plasma physics modeling.
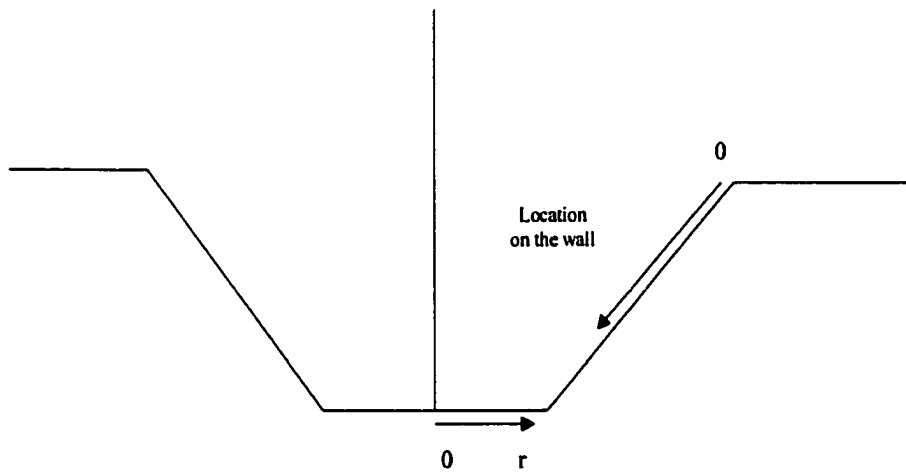
Figure 4.15. Locations defined for monitoring accumulated total ion flux distribution for a trench.
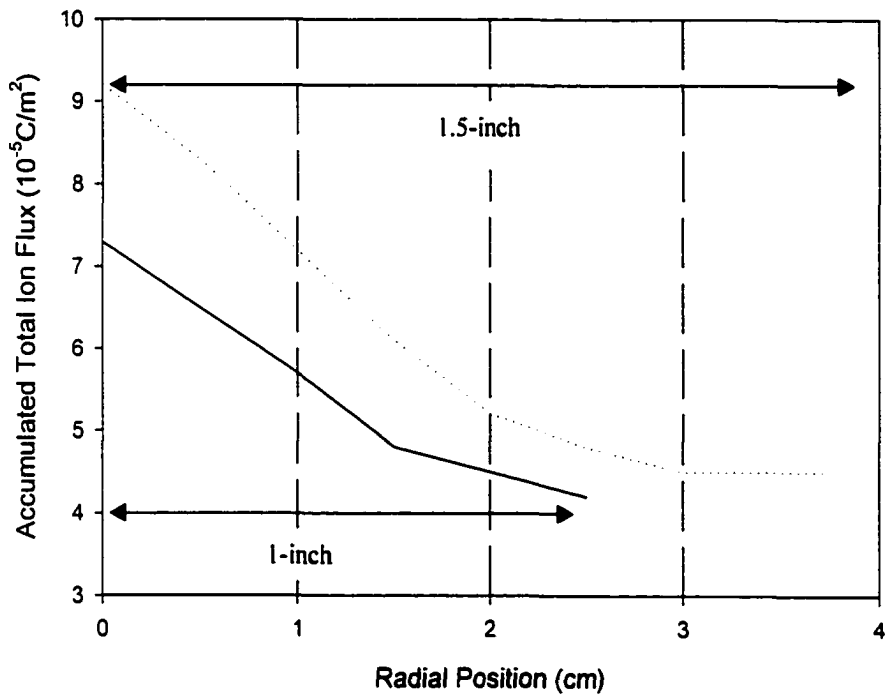
Figure 4.16. The radial distributions of the accumulated total ion flux at the bottom of 2-inch deep holes
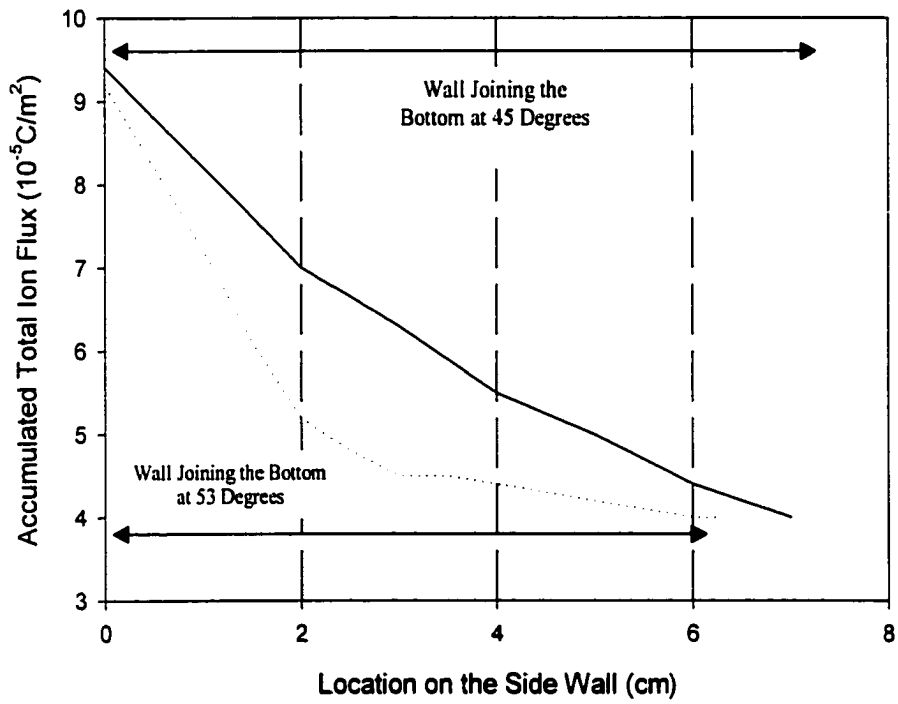
Figure 4.17. Accumulated total ion flux distribution on the trench walls.

Chapter 5

Pattern Writing by Implantation in a PSII System

5.1 Present Direct Write Technology

Direct write technology is under intensive study as one approach to integrate 3-dimensional mesoscopic electronic components in a conformal manner, at low-substrate temperatures, on a large variety of substrates. Mesoscopic electronic devices are defined as electronic devices that have sizes ranging between conventional microelectronic devices (sub-micron range) and traditional surface mount components (10 mm range). By integrating advanced electronics, functional devices, and active components into the substrate, one can lower the system weight and reduce cost [21]. The advanced electronic devices being considered include resistors, capacitors, inductors, high gain antenna, interconnects. Active components include batteries. Functional devices include embedded sensors for pressure, voltage, temperature, humidity, etc. The ability to directly-write power devices offers many system advantages, from higher battery specific energy densities to lower overall system weight. If the electronics and the power source are integrated, there will be no need for traditional

120

printed board circuits. Ultimately, machines and electronics can become simple integrated systems. Possible applications include miniature passive components for microsatellites, munitions, toys, and wireless communications such as cell phones and GPS, embedded sensors for condition based maintenance and for the medical industry.

Direct write also presents the possibility of replacing photoresist for all electronic applications by removing the mask step and reducing the number of steps required to produce electronic circuits [93]. The ability of direct write manufacturable device on the substrate will save money and process time. Current technologies used for direct write can be classified into two categories: deposition-based and print-based.

Deposition based technologies include thermal spray [94, 95], molten metal droplet deposition [96], micropen [97], focused ion beam [98], laser assisted chemical vapor deposition [99] and ink-jetting [100]. Thermal spray processing techniques are of great interest for large area coating in industrial applications. Thermal spray uses flame, arc, detonation, and plasma for spraying the materials to be deposited [4]. In each case, powder precursors are fed into the spray head where the local temperature is often in excess of $3000°C$. The heated precursor materials are subsequently accelerated onto the substrate at 90 m/s for flame spray to over 700 m/s for detonating spray. The high temperature and high kinetic energy of the arriving particles are beneficial for the formation of adherent and dense coatings but sometimes harmful to sensitive substrates. Fine tuning of the composition and structure of the coating is difficult. Molten metal droplets also are not suitable for sensitive substrates.

Variations of chemical vapor deposition (CVD) process rely on chemical reactions on the substrate surface to produce the desired film, and thus allow reproducible film composition However, it also makes producing films with composition that vary from equilibrium difficult. CVD usually requires elevated substrate temperature to promote the desired chemical reaction on the surface and to achieve good deposition rate, which may be unacceptable for some applications that need to keep the bulk material microstructure, or materials that can not be heated to high temperature, such as most plastics or polymers.

Print-based or ink-based technologies use existing or modified print heads and special "ink" to print microscopic features on the substrates. Thus for every material that needs to be direct written, a solution or suspension of the material with the proper viscosity has to be found. After printing, drying or annealing are usually involved to obtain the final features with right composition and properties.

Both deposition-based and ink-based technologies produced features on top of the substrate surface. Both the original surface finish and the substrate size are therefore changed by the writing process. There is no effective means to control the surface finish of the produced features, except perhaps by chemical-mechanical polishing after the write step. For deposition based technologies, film adhesion is always an issue and surface pretreatments or buffer layers may be found to be necessary. For ink-based technologies, the proper solvent may not be available for the material that needs to be written. Even with the materials can be written with ink, dense and uniform features are not easy to obtain.

5.2 Pattern Writing by Implantation

5.2.1 Strategy and Advantages

High energy ion implantation is an important surface modification technique, which causes minimal dimensional change, and avoids thermal distortion of the surface profile of the treated object [11–13]. It also keeps the surface finish of the substrate. As a low-temperature, surface processing technique, it changes the surface material properties without changing the bulk materials microstructure and properties. Unlike thin film deposition, ion implantation happens beneath the surface of the substrate. Therefore, there is no worry about the bond strength of the converted layer leading to coating delamination. PSII is also a non-equilibrium process; new alloys are not limited by classical thermodynamics properties and diffusion kinetics. By control of implantation time and voltage, graded surface layers can easily be produced.

Plasma source immersion ion implantation uses the plasma of the species to be implanted as the ion source. The target to be implanted is usually immersed in the plasma and all the exposed surfaces of the target are implanted simultaneously when a train of high voltage negative pulses is applied to the sample stage. Compared to beam line implanters, It is advantageous for large-area, high-dose, and three-dimensional target implantations.

Our planar RFI source for the large-scale PSII system has been found to be able to provide high density plasma with good spatial uniformity. It is capable of large area uniform processing. It is also feasible to selectively convert surface area properties of very large substrate.

In this study, pattern writing has been performed by exposing metal and semiconductor samples through masks, to high ion doses. It was studied as an ink-less, deposition free, mask-based direct write technique as an alternative to current direct write technologies. AFM calibration gratings, made from Si, were also implanted. Implantation depth profiles were characterized by variable-angle spectroscopic ellipsometry (VASE) and AES and compared to TEM results. Measured lateral and depth profiles are compared to the feature morphology to assess lateral diffusion, pattern transfer fidelity, and wall-effects on the depth profile. This chapter also presents the results of MAGIC modeling of flux and angle of ion trajectories through the boundary layer predicting the magnitude of flux as a function of 3-D location on objects in the expanding sheath, and to evaluate the fidelity of pattern transfer as a function of feature size.

5.2.2 Experimental Conditions

Two kinds of substrates were used for studying pattern transfer: flat substrates and silicon gratings. Flat substrates, including silicon wafers (100 mm in diameter, 0.5 mm thick), polished stainless steel plate (9.12 cm in diameter, 1.2 cm thick), and pure Ti and Ta sheets (25 mm×25 mm, 0.5 mm thick for Ta, 1 mm thick for Ti), were implanted through a 150 μm thick metal mask with 100 μm wide lines and 100 μm ID holes. The mask was weighted to secure it to the stage using a shaped metal ring and a metal cube. The ring is 2.5 cm tall, with a 2.5 cm OD and 2.3 cm ID. The cube is 3.8 cm×3.8 cm×3.8 cm. The ring and the cube were carefully positioned on the 100-mm Si wafer to study wall effect on

dose and sheath distributions. Pure silicon gratings with trapezoidal groove cross-sections and 10 μm groove separation were also implanted.

Research grade nitrogen (99.999%) was used as the gas source. A base pressure of $\sim 10^{-8}$ Torr and operating pressures of 5×10^{-4} to 2.5×10^{-3} Torr were used. Silicon wafer implants were performed at pulse voltages of 50 kV and repetition rate of 20 Hz for 10 hrs. Stainless steel was implanted at 50 kV at 25 Hz for 9 hrs. The Ti and Ta sheets were implanted through the mask at 40 kV at 25 Hz for 7.5 hrs. Si gratings were implanted at 25 kV at 40 Hz for 5 hrs. The estimated temperature rise for these implantation runs was less than 50°C.

AES and XPS spectra were taken using a VG Scientific MARKII ESCALAB equipped with EX05 ion gun for depth profiling. Nitrogen concentration depth profiles for high dose nitrogen implanted Si and Ti were obtained by AES. The sputtered depths were calibrated by surface profilometry. The overlapping of nitrogen and titanium peaks and compensation for the presence of oxygen were considered when calculating the nitrogen concentration [101]. The nitrogen AES peak is overlapped with titanium 385 eV peak. Usually, the concentration of nitrogen is deduced by a subtraction considering the ratio between the two titanium AES peaks, namely the 385 eV peak and the 418 eV peak. However, when there is oxygen in the system, things become more complicated because this ratio changes with different oxygen concentration. To reach the right concentration of implanted nitrogen for our samples, the influence of oxygen was also considered following methods developed by previous studies [101].

A variable-angle spectroscopic ellipsometer (VASE) [50] was used to study the optical properties of the nitrogen-implanted silicon and stainless steel samples. Three incident optical angles (70, 75, and 80 degrees) were used for each area. The incident optical beam was about 3 mm in diameter. Because the as-received Ti and Ta samples did not have smooth optical surfaces, ellipsometry could not be used to examine them.

The cross-section of nitrogen implanted Si gratings was examined by TEM at the Solid State Division of Oak Ridge National Laboratory.

The depth profiles for high dose implantation were also calculated using Profile Code [102].

5.2.3   Results and Discussion

The implanted Ti surface showed the gold color characteristic of stoichiometric TiN, with a slight pink hue because of the slightly oxidized surface layer. The AES depth profile for high dose nitrogen implantation of Ti is shown in Fig. 5.1 for a Ti substrate. The nitrogen concentration fluctuates around the level for stoichiometric TiN (50%) throughout most of the implanted depth, decreasing sharply at ~5000 Å. The native oxide layer of the original substrate was not stripped prior to implantation, accounting for the relatively low nitrogen concentration in this range. Similar nitrogen depth profiles were obtained for the implanted Si wafer (Fig. 5.2), again showing a thick native oxide layer that reduced the nitrogen reaction with silicon, producing a low nitrogen concentration.

The experimental implantation depth profiles are in good agreement with the high-dose model calculation of Profile Code, which predicts both the constant concentration for

most of the implanted depth and the steep decrease at the end of range [102]. As shown

in Fig. 5.3, the nitrogen concentration is saturated for some range at an implantation dose

of $1.0 \times 10^{18}/cm^2$. As the dose is further increased, the little valley of the concentration

curve is further filled to the saturation level, to result in a very flat depth profile (Fig. 5.4).

AES Depth Profile of Nitrogen Implanted Titanium
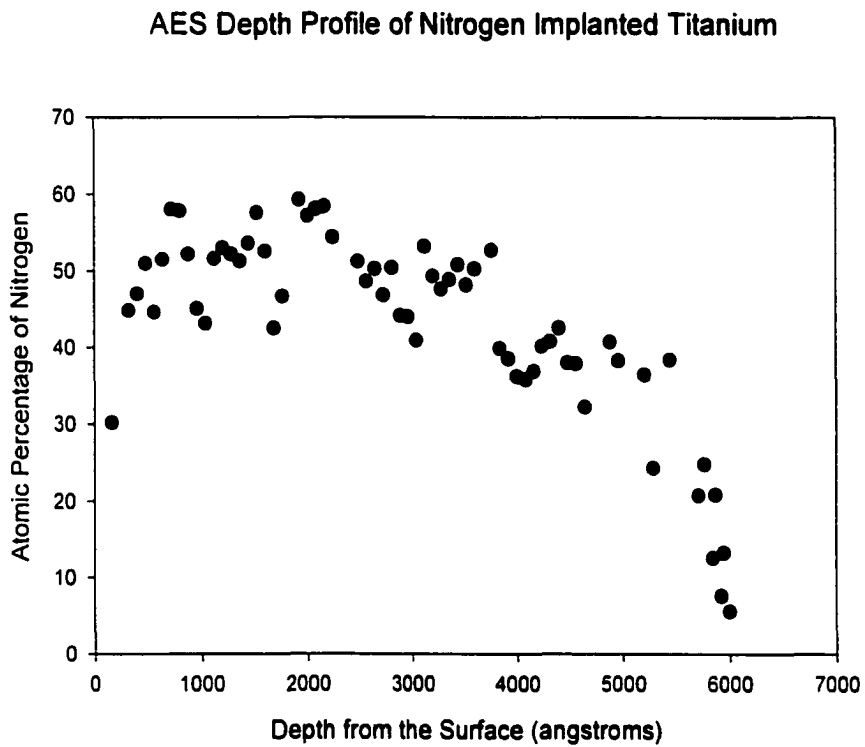
Figure 5.1. Implanted nitrogen concentration depth profile for Ti substrate obtained by AES depth profiling

Test Position	Thickness of Layer (Å)	Color of Spot
A	1770 ± 20	Golden
B	914 ± 3	Blue
C	1055 ± 3	Light Blue
D	1580 ± 20	Golden (lighter)
E	851 ± 2	Blue
F	1620 ± 20	Golden (lighter)
G	1820 ± 20	Golden

Table 5.1. Nitrogen implanted layer thickness on Si substrate obtained by ellipsometry measurements

The ellipsometry results for nitrogen implanted Si and stainless steel samples confirmed the film-like depth profiles observed by AES and predicted by Profile Code. Table 5.1 shows VASE results for 7 different spots on implanted Si wafer. Adding a graded optical layer to model the gradual concentration changes typical of low-dose implantation depth profile, did not improve the fits to the data. The optical properties of the implanted layer closely resemble that of an extremely uniform thin film. These optical methods thus provide a dose distribution for high dose implantation, since the dose is in proportion to converted layer thickness and thickness can be correlated to area color. They are non-destructive and quick compared to other depth profiling techniques, such as AES and SIMS. The color of 100 μm lines and 100 μm ID dots produced by implanting through the metal mask were studied using an optical microscope fitted with a CCD color camera and TV monitor. The edges between the implanted and un-implanted area were narrower than the resolution of our camera, indicating pattern transfer contrast considerably sharper than 2 μm. A 5.7 μm wide, blue-colored annular zone appears along the circumference of the exposed area. Ellipsometry indicated that this annulus received only ~40% of the maximum dose received at the center of a 100 μm hole. The sample stage temperature did not rise significantly dur-

AES Depth Profile of Nitrogen Implanted Silicon
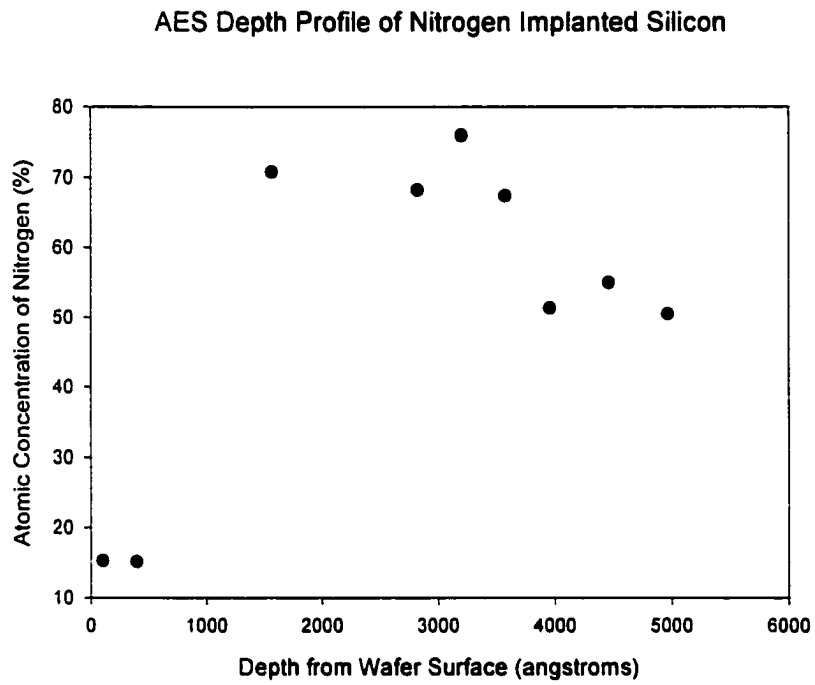
Figure 5.2. Implanted nitrogen concentration depth profile for Si substrate obtained by AES depth profiling
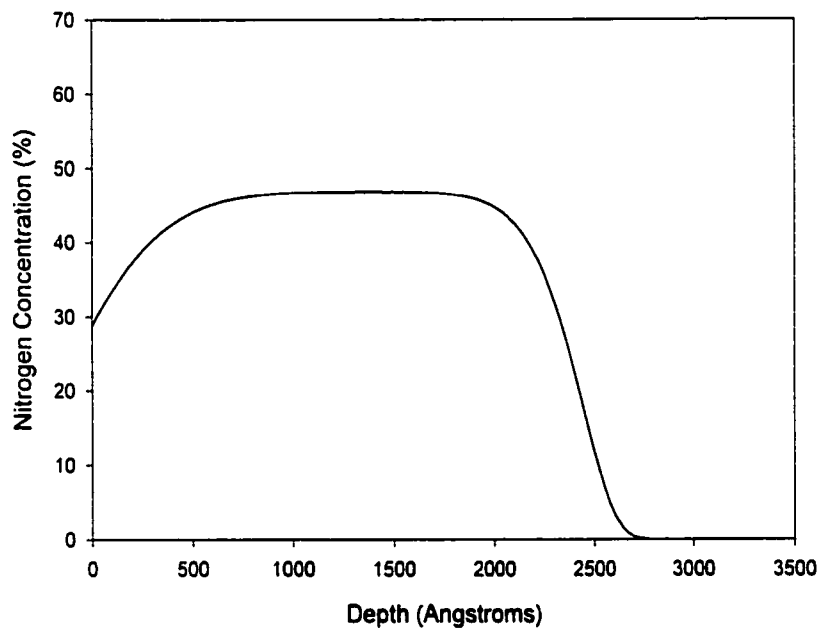
Figure 5.3.   Nitrogen concentration in Ti substrate calculated by high dose model of Profile Code. The implantation voltage is 50 KV and the dose is $1.0 \times 10^{18}/cm^2$.
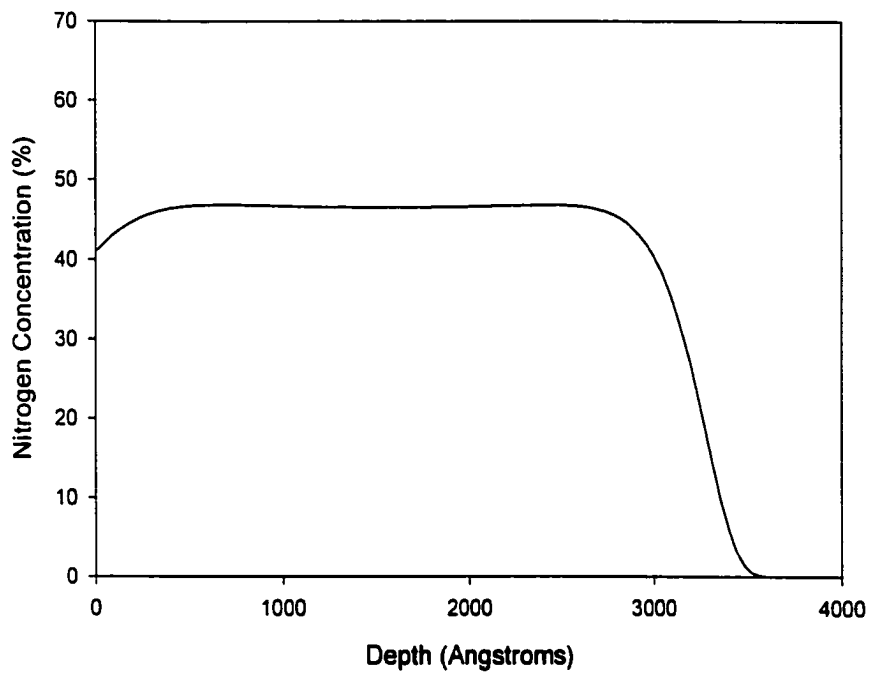
Figure 5.4.   Nitrogen concentration in Ti substrate calculated by high dose model of Profile Code. The implantation volatge is 50 KV and the dose is $2.5 \times 10^{18}/cm^2$.

ing implantation. Analysis of the annular zone just outside the implanted circle confirmed our assumption that lateral thermal diffusion may be ignored.

The AFM calibration gratings were exposed to study the dose distribution in and around narrow features. The trapezoidal groove cross-sections provide virtual mask stripes over the flat Si surface. Our apparatus may be operated in a manner which allows us to co-deposit SiO_2. This mode is discussed in Chapter 3 on RFICP source designing and characterization, and in Chapter 6, on nitrogen-doped SiO_2 films deposition. Fig. 5.5 shows TEM picture of Si gratings implanted in this mode. As shown in Fig. 5.5, the implanted layer is capped with co-deposited SiO_2. The flat tops and bottoms of the grooves show a similar implanted layer thickness. The sloped sidewalls were not uniformly implanted. The converted layer near the corner where the bottom and the sidewall meet is apparently thinner, while the layer near the corner where the top and the sidewall meet is much thicker.

We modeled the dose and angle distribution for mask-based pattern writing using MAGIC, an electromagnetic particle-in-cell, finite-difference, time-domain code for simulating plasma physics process [91], which we adapted for this purpose. The chamber and sample stage geometry included in the models are assumed to be azimuthally symmetric. Thus only a 2D half-plane cut is necessary for full simulation. We have used this simulation to examine matrix sheath formation, sheath propagation, evolving to the steady Child-Law sheath; ion trajectories, ion depletion, and the distribution of ion flux for different mask shapes and aspect ratios. In the simulations shown here, the time step was $5 \times 10^{-10} s$ over a simulated implantation time of $2.5 \times 10^{-7} s$, representing the initiation of a quasi-steady state lasting throughout the pulses. The modeled ion plasma density was $10^{10}/cm^3$ and ap-

SiO₂ cap

Implanted
Layer

Si Substrate

10 µm
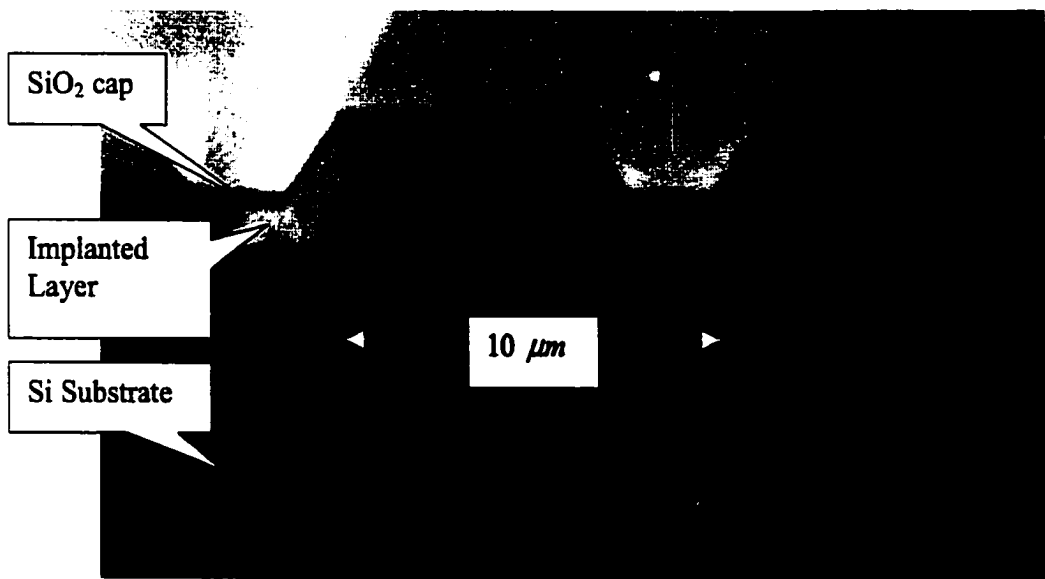
Figure 5.5. TEM picture of cross-section of nitrogen implanted Si gratings, showing the nitrogen-implanted layer, the Si substrate, and the SiO₂ cap layer

plied voltage ~10 kV. The positive ion distribution at $1.2 \times 10^{-7}s$ modeled for a groove with a sidewall to bottom angle of 53.1 degrees is shown in Fig. 5.6. The shallower angle of incidence at the slopes sidewall predicts a non-uniform distribution consistent with TEM observations. The ion flux distribution (Fig. 5.7) predicts that the bottom of the slope will receive a factor of 2 to 3 less flux, also in agreement with TEM results. Trenches with sidewall joining the bottom at different angles were also modeled and the ion flux distributions were obtained. More details were given in Chapter 4 on MAGIC modeling of PSII process. With carefully designed mask shape and thickness, the uniformity of implantation and shorter implantation time can be achieved.

5.3 Conclusion

High dose nitrogen implantation into various substrates was performed, yielding film-like depth profiles. A stoichiometric TiN layer was produced on the Ti surface. Depth profiles obtained experimentally by AES, VASE and those modeled with Profile Code are in good agreement. Patterns 100 μm in line-width were transferred by implantation, with lateral contrast better than $2\mu m$. The TEM study of nitrogen implanted Si gratings showed implantation can produce sharp patterns as small as $3\mu m$ with good uniformity, in agreement with MAGIC code simulation. With carefully designed masks and good control of implantation parameters, PSII can be used for pattern writing of smaller features.
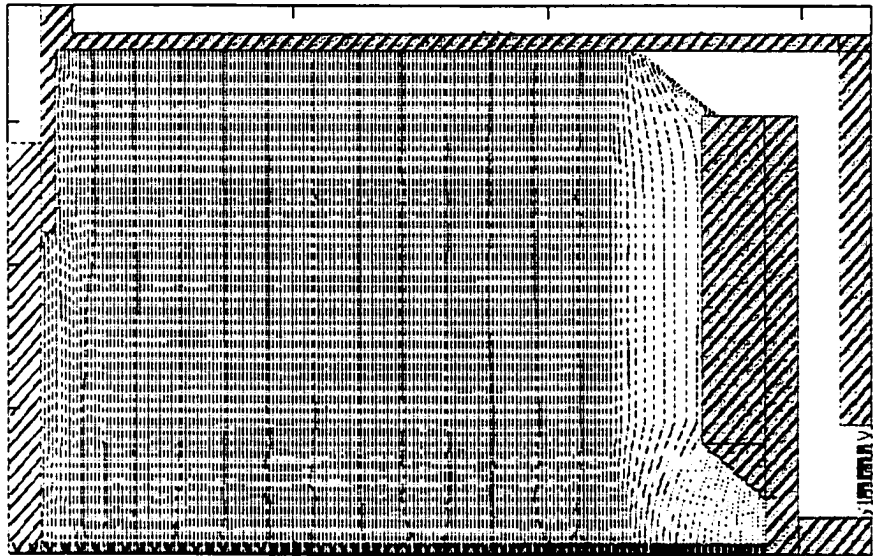
Figure 5.6. MAGIC modeling of PSII process in a trench, showing positive nitrogen ion distribution at time $1.2 \times 10^{-7} s$.
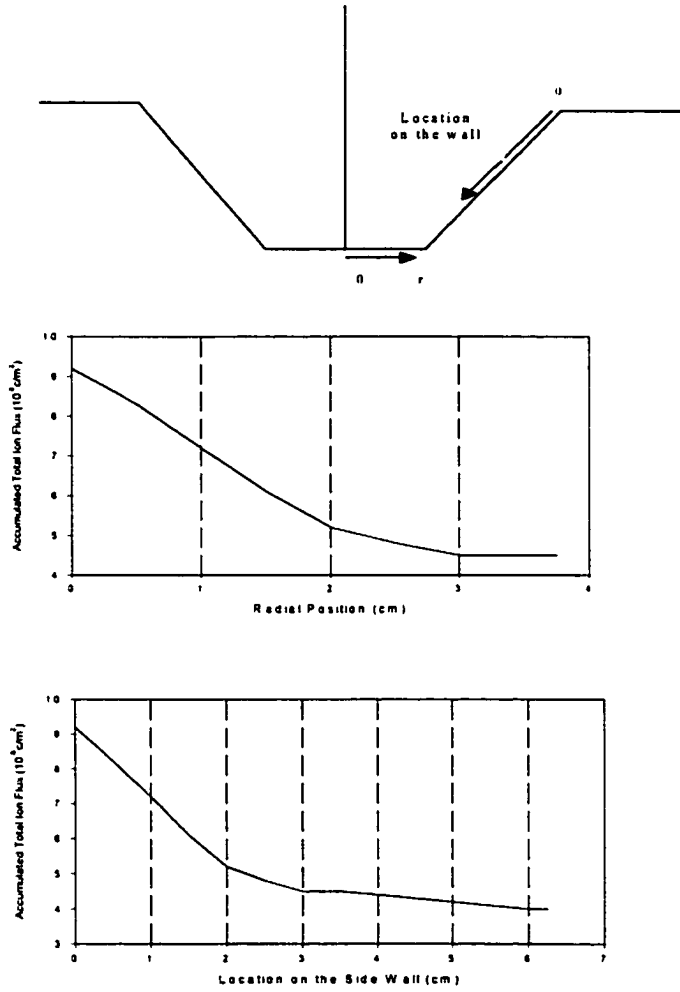
Figure 5.7. MAGIC simulation results of ion flux distribution along a trench surface. The trench is 2 in. deep, 3 in. wide at the bottom, with side wall joining the bottom at 53.1 degrees. The simulation time is 2.5×10^{-7} s.

Chapter 6

Deposition of N-doped SiO$_2$ Films by Novel Control of the rf Operation Mode

6.1 Introduction

High quality SiO$_2$ film is important for ULSI [103] and for optical Si-based waveguides fabrications [104]. It has been produced by methods including various kinds of CVD [23, 103, 105–107], thermal oxidation [103], oxygen ion implantation [104, 108], aerosol-gel deposition [109] and by Laser or electron beam ablation [110–112]. SiH$_4$ process is popular for CVD SiO$_2$ because of its low deposition temperature and high growth rate, however, SiH$_4$ is not safe to handle. Thermal oxidation and oxygen ion implantation require Si substrate to generate SiO$_2$. Laser or electron beam ablation usually produces rough film surfaces.

A small concentration of nitrogen in the SiO$_2$ film and at the Si-SiO$_2$ interface has been found to improve the reliability of the dielectric film and to prevent doped boron diffusion [3, 105, 106]. Spatially controlled nitrogen incorporation SiO$_2$ layers for device

Reproduced with permission of the copyright owner. Further reproduction prohibited without permission.

manufacturing has been studied [22]. Hydrogen-free deposition gases have also been investigated for higher film quality [23, 106]. As an alternative, SiO_2 films can also be doped with F to achieve a lower dielectric constant for ULSI applications [113].

In this work, a novel operating regime has been used in our PSII apparatus which we called PSII/PVD. Using this controllable regime, our system has been used to deposit large-area, uniform, N-doped SiO_2 films. This method shows promise for depositing doped SiO_2 at very low temperatures, on a variety of substrates, allowing a range of dopant combinations to produce variable dielectric constant, and spatially controlled nitrogen incorporation into the deposited layers. The system uses planar rf coil for plasma generation and for SiO_2 film sputter deposition. Nitrogen is incorporated into the deposited films and the film/substrate interface by a combination of PSII and continuous plasma nitriding. High quality nitrogen-doped SiO_2 films have been successfully deposited on Si, Ti, glass, and stainless steel substrates with excellent adhesion. Compared to other gases for SiO_2 deposition [103, 106], N_2 is safe to handle and is available in high purities at low cost. N_2 is also easy to pump and is benign to vacuum systems. In addition, the deposition plasmas is inherently hydrogen free so the amount of hydrogen incorporated is minimized. The PSII apparatus can also be employed to perform in-situ substrate surface cleaning and conditioning prior to film deposition. In addition to Si substrates, SiO_2 films can be produced on other metal, glass, or polymer substrates.

Nitrogen-doped SiO_2 film deposition by the PSII/PVD system is discussed in this chapter. The system design and operation is described. The deposited films were studied by AES and by SIMS concentration depth profiling. Variable angle spectroscopic ellipsometry

(VASE) also was employed to investigate film optical properties and thickness, which was compared to and confirmed by surface profilometry results. The cross-section of processed small features was studied by TEM to reveal the multi-layer structure and the degree to which the process preserves small feature dimensions during processing.

6.2   Experiments

The PSII/PVD system is shown schematically in Fig. 6.1. It consists three sub-systems: the vacuum deposition chamber, the rf plasma source, and the high voltage pulse forming network. Detailed information of the PSII/PVD system is given in Chapter 7.

Three different kinds of substrates were used: pure titanium sheet (nominal purity 99.6%), silicon wafer (with a thin native oxide layer), silicon AFM calibration gratings (with a thin native oxide layer), and highly polished stainless steel test electrodes for the FEL at TJNAF. The titanium sheet is 2.54 mm×2.54 mm, 1 mm thick. The Si wafer used is 100 mm ID, p-doped, and (100) oriented. The pure Si grating is 5 mm×5 mm and 1 mm thick, with the center 3 mm×3 mm area consisting parallel trenches 2 μm deep and 2 μm wide. The stainless steel test electrode is ~0.15 m diameter, 0.019 m thick plate having a Rogowski surface profile [2]. It was also polished to a 1 μm rms surface finish.

Research grade nitrogen (99.9995%) was used for all depositions. The system base pressure before processing was better than 1×10^{-6} Torr. All the samples were placed on the sample stage in the middle of the chamber without active cooling.
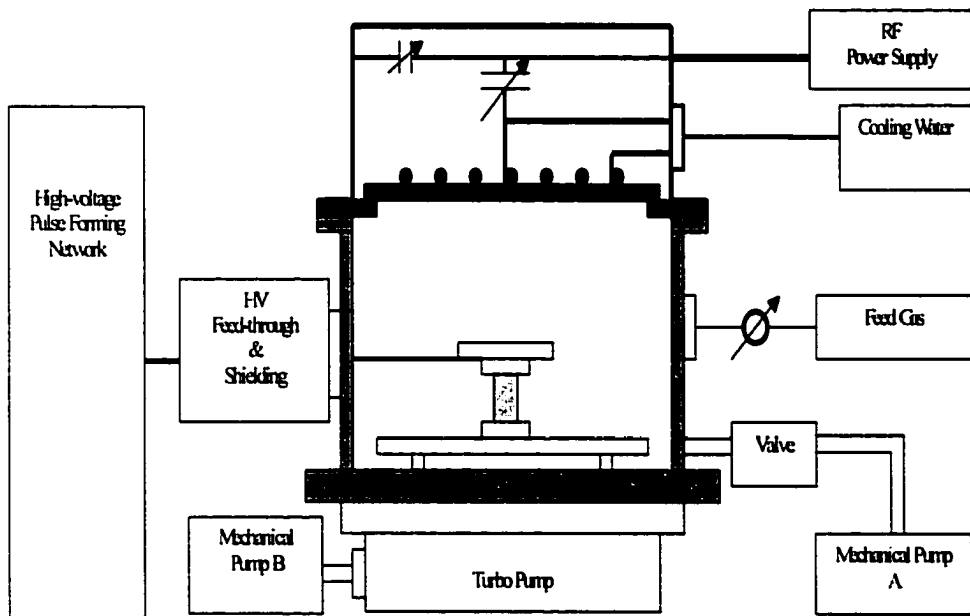
Figure 6.1. The integrated PSII/PVD system for large-area, uniform, doped SiO₂ films depostion.

The titanium sheet was first exposed to the plasma with an rf power of 360 watts and nitrogen pressure of 5.2×10^{-4} Torr for 1.7 hr. The substrate was then pulsed at 38 KV and 25 Hz for 3.7 hr. The high voltage pulse was 10 μs wide, with an average current of 21.3 A. Part of the titanium sheet was masked to create a untreated zone for comparison purposes.

The silicon wafer was processed at 5.0×10^{-4} Torr with an rf power of 750 watts for 9 minutes, then pulsed at 30 KV at 25 Hz for 4.63 hr. A metal mask was fixed on part of the wafer for film thickness measurements.

The silicon gratings were processed at a nitrogen gas pressure of 8.0×10^{-4} torr. The rf power used for plasma generation and sputtering was 750 watts. The substrate was processed in the plasma for 20 minutes before it was co-implanted at 25 KV and 40 Hz for 5 hr. with 20 μs wide pulses. The average current during each pulse is 10 A.

The stainless steel test electrode was first processed with an rf power of 700 watts and at a nitrogen pressure of 2.0×10^{-3} Torr for 6.15 hr. Then it was pulsed at 25 KV at 20 Hz for 2.58 hr., with an rf power of 750 watts and at a nitrogen pressure of 1.8×10^{-3} torr. The pulse width was 20 μs, with an average current of 10 A during each pulse.

The processed Si gratings, Si wafer, and the titanium sheet were studied by AES for surface composition. The processed Si wafer and the titanium sheet were also depth profiled by AES. The untreated zones of the Si wafer and the titanium sheet were also depth profiled by AES for comparison. The processed Ti sheet was also studied by SIMS depth profiling. The cross-section of the processed Si gratings was also studied by TEM at Solid State Division of Oak Ridge National Laboratory. The SiO_2 film on Si wafer

was studied by VASE for its thickness and optical properties. The thickness obtained was compared to the thickness as measured by surface profilometry (Dektak^{3}ST surface profile measurement system).

6.3 Results and Discussion

6.3.1 Operation of the PSII/PVD System

Planar coil rf plasma source is capable of producing large-area uniform plasma for materials processing at low pressures (<50 mTorr) [12, 17]. Since rf power is coupled to the plasma inside the vacuum chamber usually through a quartz window, there are no electrical connections or supporting apparatus inside the chamber to take up extra chamber space to complicate chamber geometry, which is important for 3-D uniform PSII of large target. Operated in inductive mode, it is clean and long lasting plasma generating source for ion implantation, which requires low processing pressure for a long mean free path [114]. The planar rf coil is the inductive component of the rf impedance matching network, which inevitably causes electrostatic coupling between the coil and the plasma. Electrostatic coupling is important for the ignition of the plasma and helps to sustain the discharge at low plasma ion densities. For the sub-mTorr pressure and low rf power (<1 Kw), capacitive coupling dominates and there exists large self-bias on the rf coil, which produces an rf sheath at the plasma-window boundary [17, 68, 115]. This high voltage sheath accelerates ions in the plasma to sputter the window material. In our system, we can choose this mode to produce high purity SiO_2 films from our optical quality quartz window.

For our preliminary studies, nitrogen was used as the processing gas for all of the substrates. However, Ar can be used for sputter deposition if pure SiO_2 is desired. Dopants other than nitrogen can be introduced into the system, either being mixed with Ar, with other dopants, or being used as the sole low-pressure working gas. Stacked layers can also be produced by introducing different dopant gases for controlled time periods during the process. Implantation frequency can be adjusted during the deposition phase to produce films with different dopant concentrations.

The rf source can be controlled to operate in an inductive mode without deposition. This can be done by a combination of plasma parameter control and /or adjustable electrostatic shielding. In this mode, large-area uniform PSII can be performed to produce doped layers of different thickness and implantation dose. This pure PSII mode can be used for substrate sputter cleaning and conditioning, pre-deposition implantation, or post-deposition implantation in the deposited layer. Patent applications have been prepared regarding these novel and useful ideas.

6.3.2   AES and SIMS Depth Profiling

The AES depth profiles of the un-processed and processed Si wafer are shown in Fig. 6.2 and Fig. 6.3. As shown in Fig. 6.2, the bare Si sheet used has a thin oxide layer about 18 Å thick. The processed Si wafer is covered by Si-oxynitride layer about 1700 Å thick, consisting 60% oxygen, 32% silicon, 7% nitrogen for the 50 Å to 1700 Å range. Because of the incorporation of nitrogen, the oxygen concentration in the film is slightly lower than the stoichiometric level. The carbon concentration for this range is below 1%. At the interface

of the deposited film and the substrate, there is a nitrogen-rich zone from 1750 Å to 1840 Å, where the nitrogen concentration is more than 10%. The peak concentration for nitrogen is found to be 16% at 1790 Å. The higher concentration of carbon and nitrogen and the lower concentration of oxygen and silicon in the topmost 50 Å range were attributed to the surface absorbed layer on the film resulting from air handling. The existence of the doped SiO_2 layer was also confirmed by SIMS depth profiling

The AES depth profiles of the un-processed and processed area of Ti substrates are shown in Fig. 6.4 and Fig. 6.5. There exists an oxide layer on the bare substrate surface, with oxygen concentration higher than 10% for the top 260 Å range. The oxygen concentration decreases to below 5% after 400 Å. Carbon concentration varies around 4% level throughout the profiled depth except the top layer, where higher carbon and Si concentration were detected. The average concentration of Si in the bare substrate is lower than 3%. Depth profiling of the processed Ti substrate shows about 2250 Å of Si-oxynitride layer, consisting of about 60% oxygen, 30% silicon, 7-8% nitrogen, and less than 2% of carbon. Carbon concentration is highest at the film-substrate interface again from air handling. The oxygen and silicon concentration are very close to stoichiometric SiO_2. Depth profiling by SIMS also confirmed the existence of around 2000 Å thick silicon-rich layer (Fig. 6.6).

6.3.3   TEM Study of the Cross Section of Processed Si Gratings

The TEM picture of the cross-section of processed Si gratings is shown in Fig. 6.7. The top of the grating is covered by a nitrogen-doped SiO_2 layer, which is about 4000 Å thick for the trench top and bottom, and about 2200 Å thick for the trench sidewalls. As shown in the
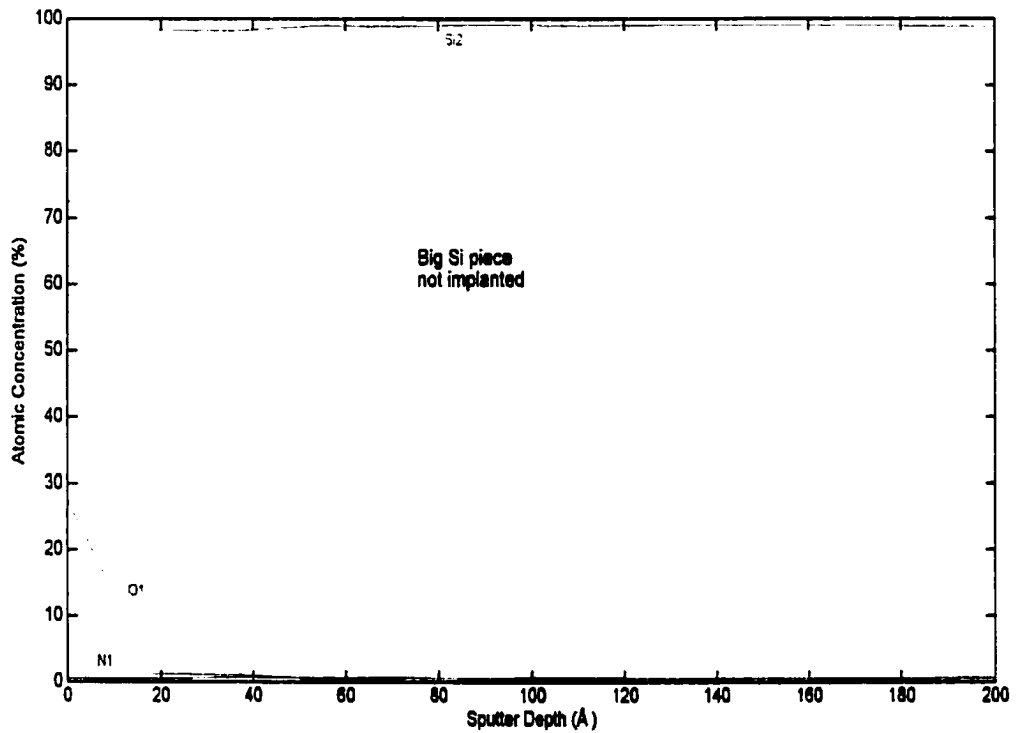
Figure 6.2. AES depth profile of bare Si substrate.
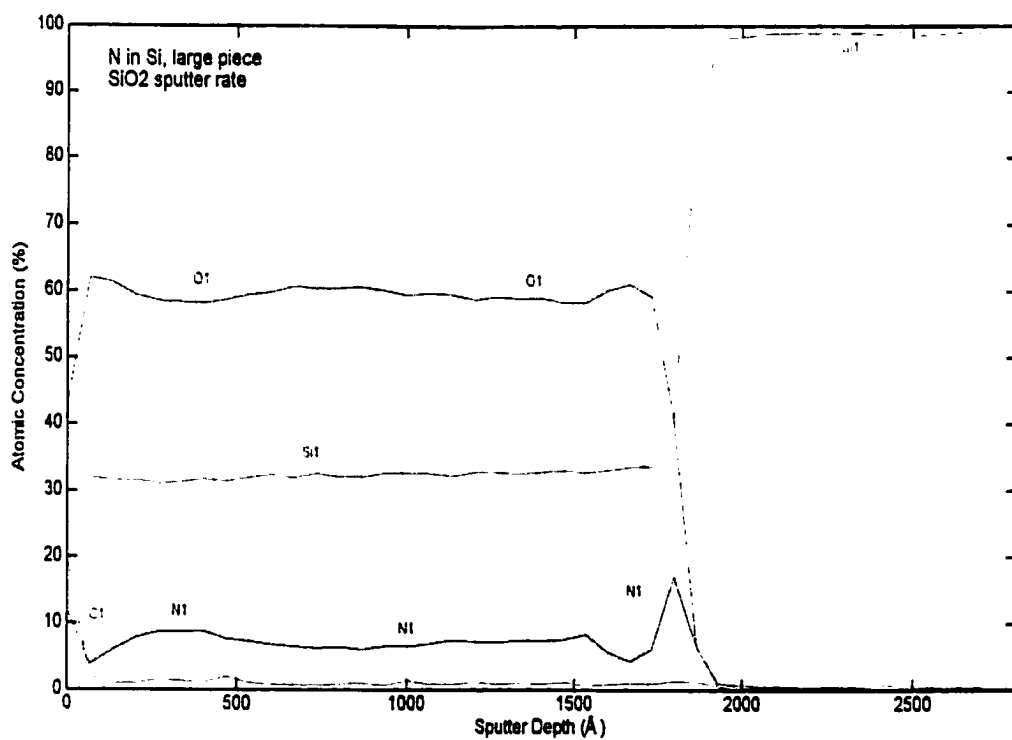
Figure 6.3. AES depth profile of nitrogen-doped SiO_2 coating on Si substrate.
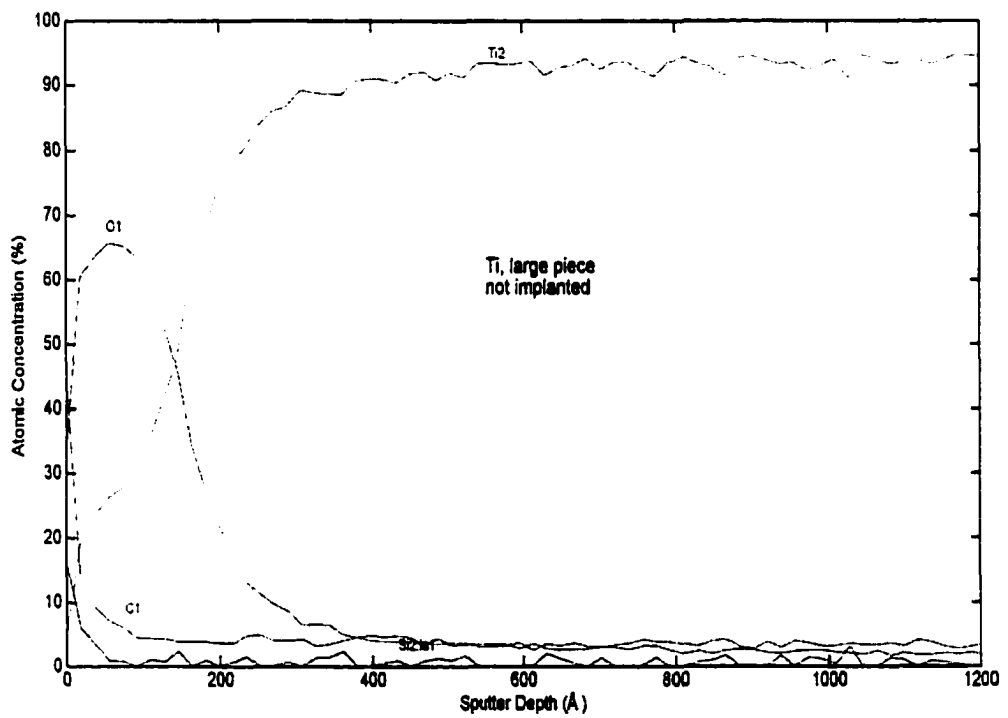
Figure 6.4. AES depth profile of bare Ti substrate.
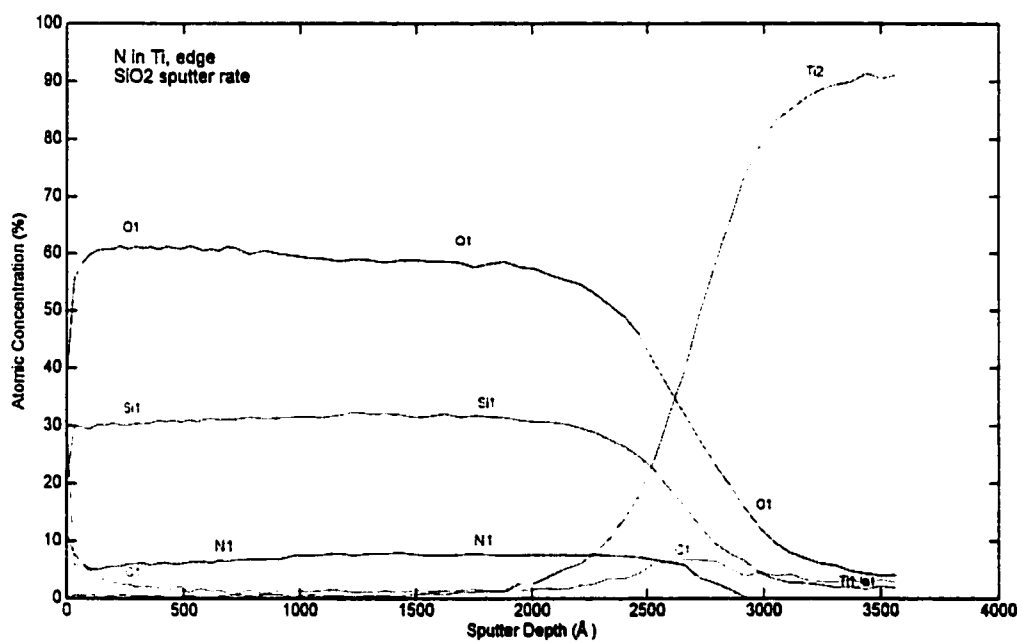
Figure 6.5. AES depth profile of nitrogen-doped SiO_2 coated Ti substrate.
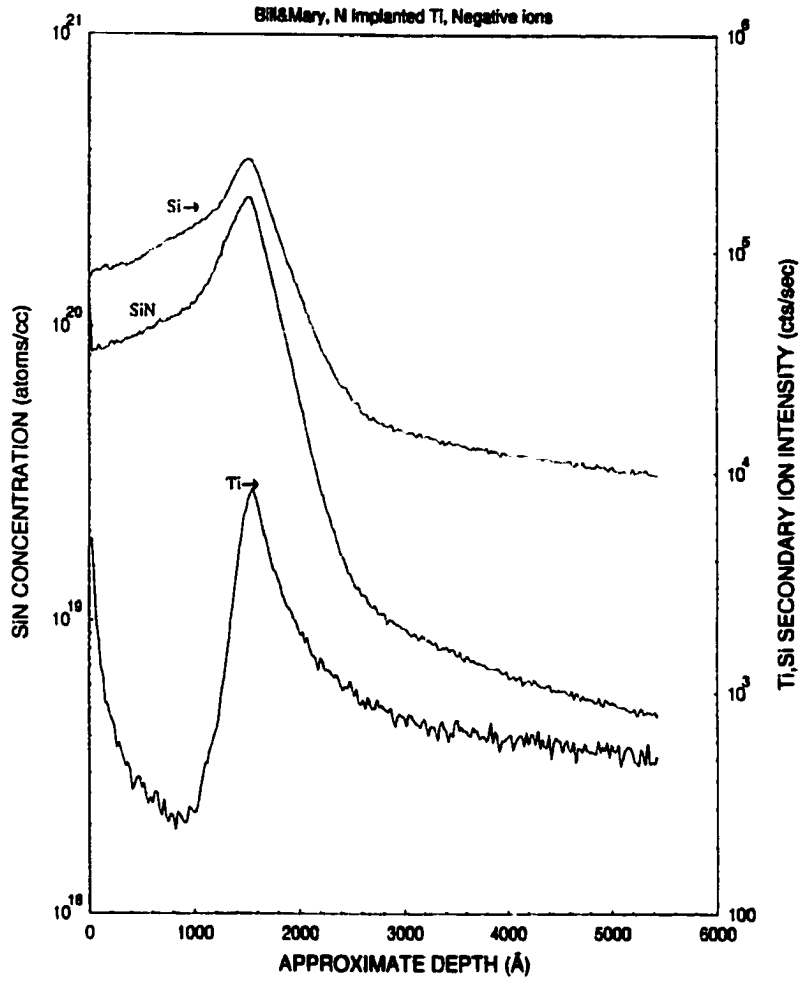
Figure 6.6. SIMS depth profile of nitrogen-doped SiO_2 coating on Ti substrate.

picture, the nitrogen implanted Si layer extends beyond the deposited film. The deposited film was confirmed by AES to be a Si oxynitride layer. The AES study of the surface of the film on the trench bottom shows 48.9% silicon, 27.6% oxygen, 13.3% nitrogen, and 10.3% carbon, whereas the concentration for the top is 49% silicon, 30.1% oxygen, 13.0% nitrogen, and 8.0% carbon, nearly the same, and probably within the expected error from the combination of the process variability and measurement methods.

6.3.4   Ellipsometry and Surface Profilometry Study

One area of the SiO_2 film deposited on the Si wafer through the metal mask was studied by Ellipsometry for its optical properties and thickness. A typical result is shown in Fig. 6.8. The deposited film is highly transparent, showing interference colors when viewed under fluorescent room light. The measured index of refraction is 1.483 at 5086 Å. The handbook value for fused quartz is 1.462 [29].

The surface profilometry results also confirmed the thickness results obtained by ellipsometry studies. The result of one of the measurements is shown in Fig. 6.9. Considering the processing time for the Si wafer, the average deposition rate is about 8-9 Å/min. Because a metal block was used to clamp down the metal mask to the Si wafer, there are areas of different film thickness available for profilometry study. The thickness of each area was correlated to color appearance to investigate film thickness distribution.

The film deposited on the stainless steel FEL test electrode was inspected visually for color distribution, to determine film uniformity [114, 116]. The picture of the processed electrode is shown in Fig. 6.10. The processed top surface is very uniform, showing
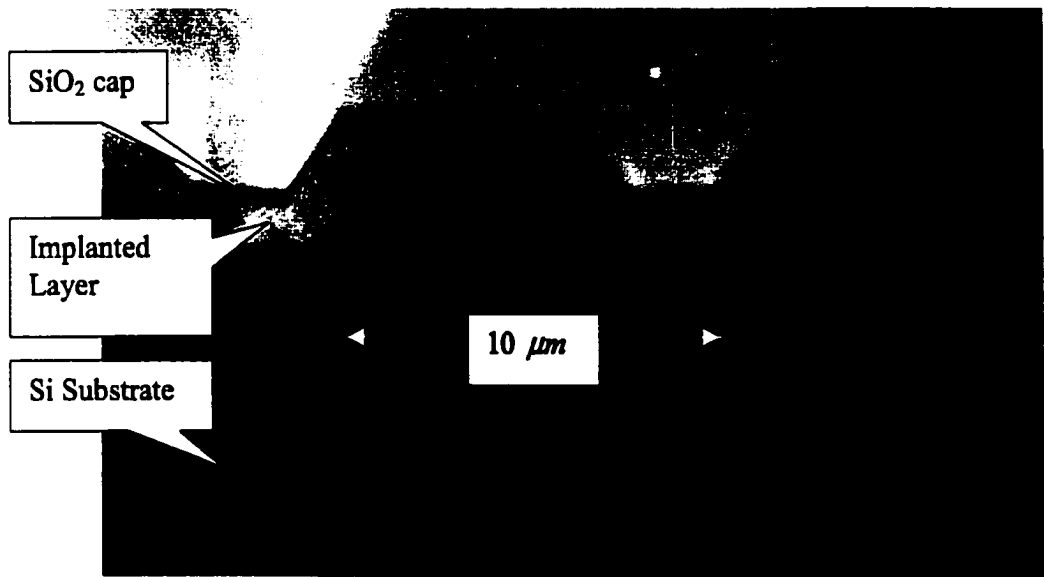
Figure 6.7. TEM picture of cross-section of processed Si AFM gratings, showing the nitrogen-implanted layer, the Si substrate, and the SiO_2 cap layer.

Cauchy Optical Constants
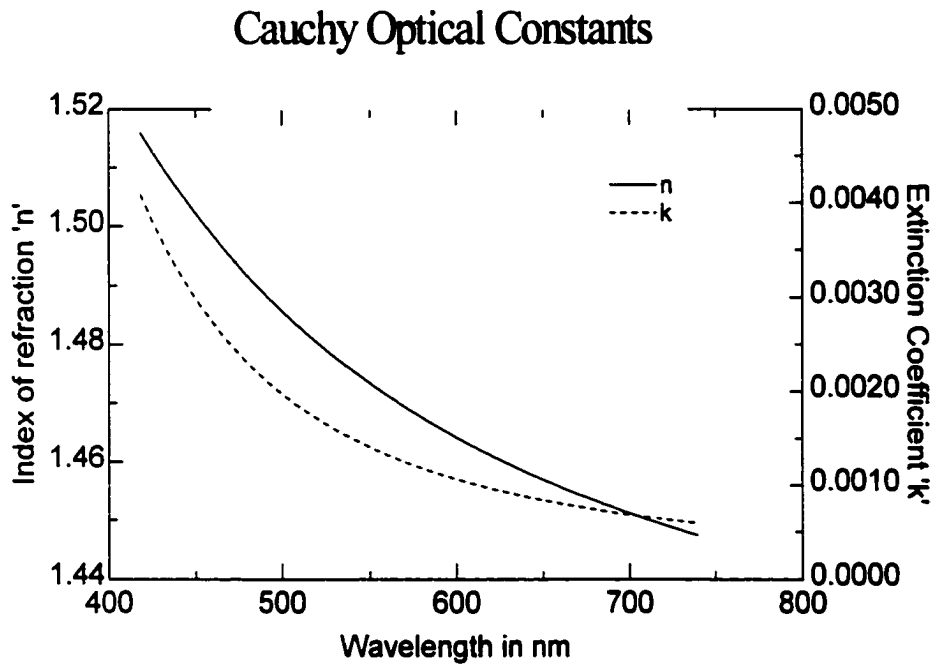
Area thickness: 2447 ± 9 Å

Figure 6.8. Ellipsometry study of the thickness and optical properties of N-doped SiO_2 film on Si wafer. Cauchy optical model was used to model the experimental data. The obtained film thickness is 2447±9 angstroms. The film is almost transparent, with index of refraction of 1.483 at 5086 angstroms. The value for fused quartz is 1.462 at the same wavelength.

Figure 6.9. Profilometry measurement of nitrogen-doped SiO_2 film thickness

the same interference color when viewed at a fixed angle. This indicates very uniform film thickness. The curved edge at the sides of the top shows color stripes parallel to the circumference of the plate, indicating different film thickness. This is to be expected, since these areas face the quartz plate at different angles. HV breakdown test at TJNAF showed that the nitrogen-doped SiO_2 film on a 0.15 m ID. FEL electrode has helped to suppress field emission. The electrode was able to operate with a field gradient of 24 MV/m, with a dark current of only 160 pA, after shorter conditioning time. The un-processed electrode for the FEL is currently operated with a field gradient of 3 − 6 MV/m, with a dark current of a few hundred nanoamps.

6.4   Summary and Conclusion

A novel operating method has been discovered in our large-scale PSII system and has been used for large-area, uniform, doped SiO_2 films deposition. The PSII capability enables in situ substrate surface cleaning and conditioning, ion implantation during film deposition, pre- and post-deposition implantation to incorporate dopant into the processed substrate with spatial control. Nitrogen doped SiO_2 films have been deposited on Si, Ti, and stainless steel substrates. The concentration depth profiles obtained by AES and SIMS show that the film is near stoichiometry SiO_2 film with 7-8% of nitrogen throughout most of the deposited layer. Higher nitrogen concentration was found for the interface between the film and the Si substrate. Ellipsometry results for one of the processed area indicate the film is highly transparent with index of refraction close to the value for fused quartz. The obtained film
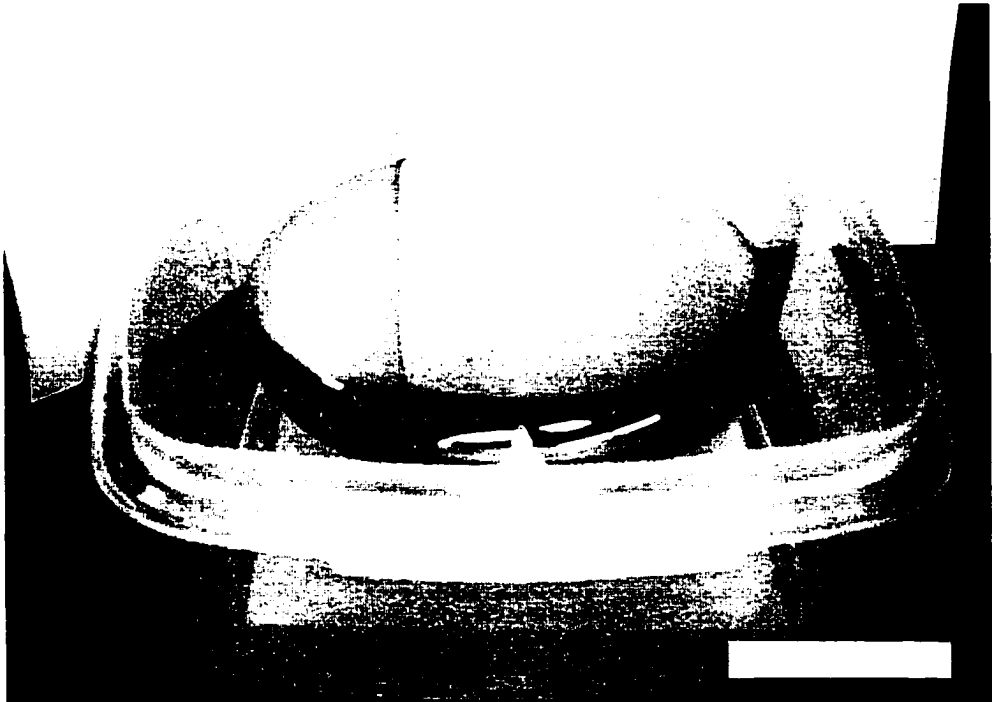
Figure 6.10. FEL stainless steel test electrode processed by PSII/PVD. The electrode is 0.15 m ID.

thickness of the area is 2450Å, which is confirmed by surface profilometry study. Large-area SiO_2 film has also been deposited on 0.15 m ID highly polished SS test electrodes. Except for the curved edge of the Rogowski surface profile, the film on the electrode surface is highly uniform. HV breakdown test at TJNAF showed that the nitrogen-doped SiO_2 film on a 0.15 m ID. FEL electrode has helped greatly to suppress field emission.

Chapter 7

Surface Processing by Plasma Source Immersion Ion Implantation

7.1 Introduction

Ion implantation is the process of accelerating ions into a material, changing its surface chemical composition, and electrical, mechanical properties. Traditional ion implantation is done by beam-line implanters. As shown in Fig. 7.1 [10], there is usually an ion source, from which an ion beam is extracted. The beam is then accelerated and steered toward the target. Because beam size is usually smaller than the target size, beam rastering is needed for uniform implantation. When a three dimensional target is implanted, target tilting and rotation are necessary to provide a uniform dose distribution. Plasma source immersion ion implantation is advantageous for implanting large area, three-dimensional, and complicated shaped target [10, 13–15]. As shown in Fig. 7.2, the target is immersed in the plasma of the species to be implanted. When a high voltage negative pulse is applied to the target, the positive ions in the plasma are accelerated and implanted into the target. All the surfaces of the target that are exposed to the plasma are implanted simultaneously. PSII is a non-line-of

158

sight surface treatment technique. It is not limited by beam size or beam current, especially suitable for high-dose, large area, and three-D target surface treatment.

PSII is significantly different from the conventional mass-separated and single-energy beam line implantations [10–12]. For example, in an oxygen plasma, positive ion species include O_2^+ and O^+. For a nitrogen plasma, positive ion species include N_2^+ and N^+. The substance to be implanted is introduced into the chamber in gaseous form. Proper pressure (usually in the 10^{-4} Torr range) is maintained for plasma generation. Plasma species concentration, ion energy distribution, plasma sheath distribution, and ion density distribution are important factors determining dose distribution and depth profile for PSII. When the negative voltage pulses are applied, all the positive ion species in a plasma are accelerated and subsequently implanted.

Short duration, high voltage pulses are used for PSII. The pulses are typically $10-100$ KV, $10-50$ μs long, at a repetition rate around 100 Hz. During implantation, the positive charges accumulated on the target surface need to be neutralized by the negative charges from the plasma. At high implantation voltages, the ion induced secondary electron emission coefficient is around 4.90 for 30 KV and 6.33 for 50 KV [2], which aggravates the charging problem. On the other hand, a sustained high voltage in the plasma can cause severe arcing problems, which is unacceptable for sensitive substrates or polished samples. One example is the high voltage electrode used for the Free Electron Laser electron injection gun at the Thomas Jefferson National Accelerator Facility. The electrodes are made of stainless steel with special surface profile [2], polished first to 9 μm then to 1 μm to effectively suppress field emission from small imperfections or protrusions from the surface.
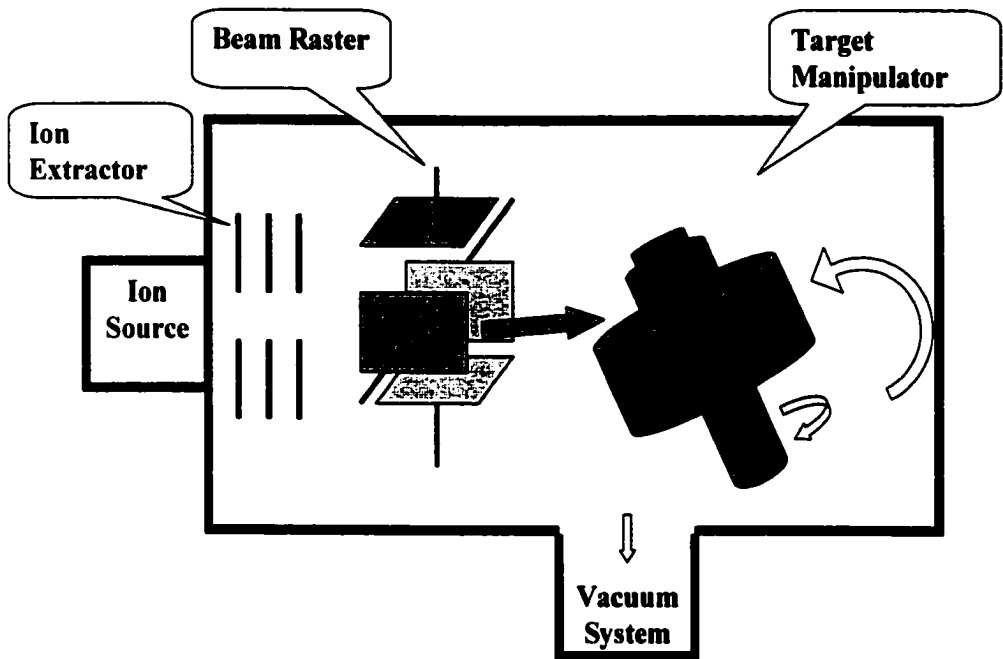
Figure 7.1. Traditional ion implantation setup.
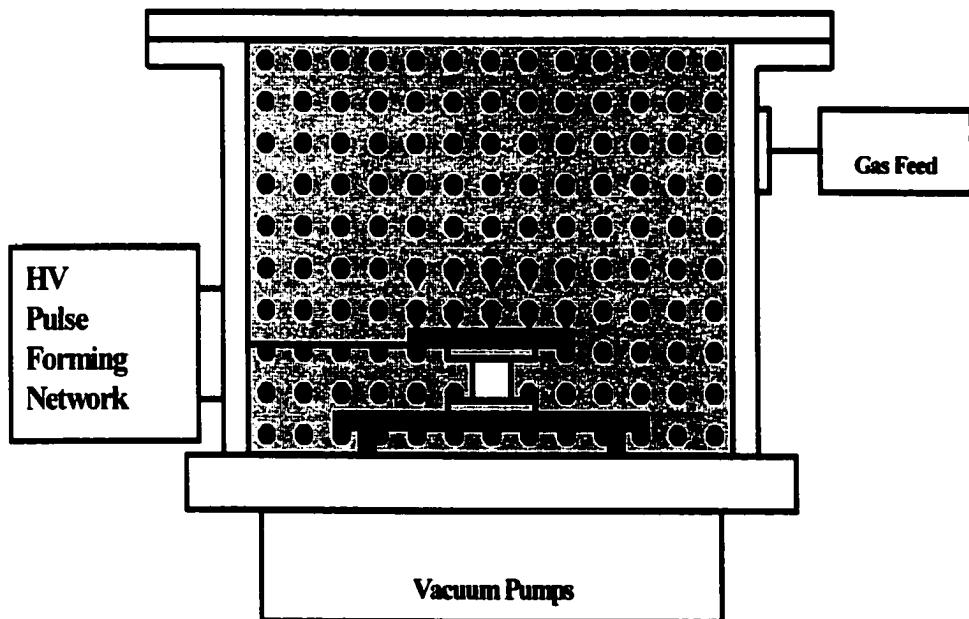
Figure 7.2. Concept of PSII

When such electrode is nitrogen ion implanted in the PSII system, extra attention has to be paid to maintain the implantation process arc-free.

Nitrogen ion implantation has been found to improve steel surface hardness, corrosion resistance and wear resistance [117,118], producing higher nitrogen concentration and wider hardened layer than low-voltage plasma nitriding [117]. Previous work in our group established that nitrogen ion implantation suppressed field emission from small stainless steel test samples [2]. Nitrogen ion implantation can also be used to produce TiN layers, which are very hard and have superior wear resistance [119]. TiN also acts as diffusion barrier between Cu and Si for microelectronics applications. Nitrides of other transition metals such as Ta, Nb, and W are also attractive because their high thermal stability and chemical inertness with Cu [120].

RFI PSII has the advantages of large-area, uniform, high-purity, long processing time, and 3-D ion implantation (see Chapter 3 on large area RFI plasma source design for large-scale PSII). Hence, it was used to perform nitrogen ion implantation into a variety of metal substrates.

Low temperature, high dose nitrogen ion implantation into a selected group of high purity transition metal substrates, including Ti, Ta, Nb, Mo, and SS, was conducted using the large-scale RFI PSII system. Surface morphology of implanted and bare substrates were studied by optical microscope. Auger electron spectroscopy (AES) was used to study the retained dose, concentration depth profile, and chemical composition of the implanted samples. Surface hardness was also analyzed for different loads to study the surface hard-

ening effect of nitrogen implantation. Highly polished stainless steel test electrodes were also implanted for testing in the TJNAF FEL facility.

7.2 Experiment

Detailed information of our RFI source is given in Chapter 3. Here we provide a simple description of the RFI PSII system to discuss the works of our implantation studies. The Large-scale PSII system with planar RFI plasma source at ARC is shown in Fig. 7.3. It consists three main subsystems: the implantation chamber, the planar RFI plasma generating system, and the pulse-forming network (PFN).

The cylindrical implantation chamber is 0.61 m I. D., 0.51 m tall, with a 0.57 m in diameter and 0.0254 m thick quartz window sitting on top of the chamber to work as the dielectric media for RF coupling. Over the implantation chamber, a 0.4 m tall aluminum cover shields the rest of the lab from RF radiation and protects the quartz window. It also serves as the support structure for the RF matching network, water-cooling lines and the 0.43 m in diameter RF antenna that is in close contact with the quartz window surface. The chamber is pumped by a Leybold-Heraeus Turbovac 450 turbo molecular pump at the bottom of the chamber and by a CIT-Alcatel (Type2033) mechanical pump attached to a side port. A Leybold D8A mechanical pump backs the turbo pump.

The pulse-forming network (PFN) is capable of delivering high voltage pulses of up to 100 KV, 30 A at a repetition rate of 200 Hz. The high voltage outputs are connected to
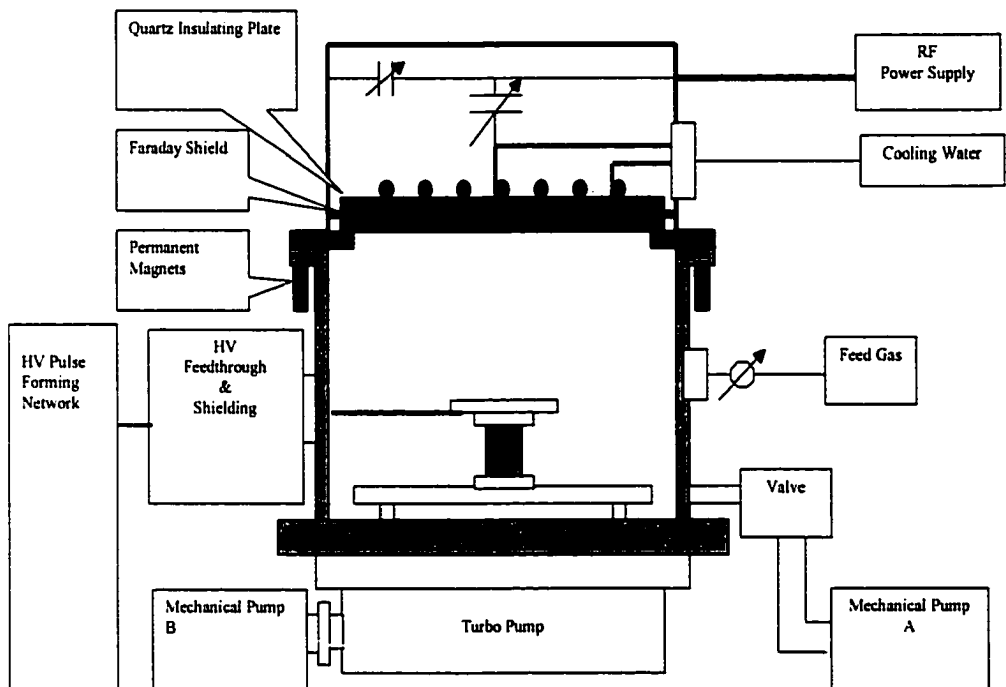
Figure 7.3. CWM large-scale RFI PSII system.

the sample stage inside the implantation chamber through a shielded HV feedthrough on the side of the implantation chamber.

Metal samples to be implanted are placed on a 6 in ID stainless steel supporting plate placed on the sample stage centered in the chamber. In this study, we used substrates of high purity Ti, Ta, Mo, and Nb sheets, 25 mm ×25 mm. Typical analysis by the manufacturer indicated nominal purity of 99.6% for Ti sheets, 99.9% for Ta sheets, 99.9% for Nb sheets, 99.9% for Mo sheets. The Ti substrate is 1 mm thick. The other sheets are 0.5 mm thick. Type 304 SS sheets with 0.03 μm (Rmax) mirror finish were also implanted. Each of the samples were half masked to provide areas that were not treated by nitrogen plasma for comparison purposes.

Research grade nitrogen gas (99.999%) was introduced into the chamber to maintain a pressure of 2.0×10^{-3} torr. The rf power used was 850 W. The samples were pulsed at 30 KV at 100 Hz. The samples were not actively heated. Previous investigation of the ion plasma density distribution allowed us to place the samples in the area where the plasma density was very uniform (see Fig. 3.9 for radial plasma density distribution). Thus the implantation condition may be considered identical for each of the metal substrates. The implantation time was 3 h. for a nominal dose of $1.75 \times 10^{18}/cm^2$.

The implanted samples were studied by AES depth profiling. The AES spectra were investigated with an electron beam of 5 KeV and 1.0 μA. Surveys were acquired before sputtering to determine elemental surface composition. Sputter depth profiling was performed while monitoring all minor elements in the survey scan, along with the substrate elements. Silicon and other chamber elements were also included in the list for monitoring

possible contaminants from the implantation system. A 3 KV, 30 μA Ar^+ ion beam was used for sputter depth profiling. The beam was rastered across a 2 mm ×2 mm area, with a incident angle of 55° to the sample normal.

The surface hardness was also tested with Shimadzu microhardness tester and was compared to unimplanted samples. For each data point, ten indentations were made. The average and standard error were calculated.

Optical microscopy was also used to compare the surface morphology of implanted and unimplanted substrates.

7.3   Results and Discussion

7.3.1   Target Temperature

Target temperature is an important parameter for PSII applications. Higher temperature usually results in more diffusion of the implanted species and in a deeper range. For masked implantations, higher target temperature results in more lateral diffusion. In order to reduce implantation time and reach higher dose, high power is usually applied, which can produce high target temperature. High target temperature may or may not be beneficial for specific applications. For instance, higher temperatures are desirable when diffusion of the species is desired. On the other hand, high temperature is not desirable for plastic, rubber, and polymer materials, or materials that with special microscopic structure which will be changed by high temperature, such as alloys. Thus target temperature prediction or estimation is important for applications design.

It is difficult to measure the target temperature in a PSII apparatus. High pulsed bias on the target is hard for thermocouples to handle. Optical measurement is limited by the chamber and port setup.

The power is applied to the target by way of a series of high voltage pulses during implantation. The PFN for our PSII system produces pulse of $0 - 100\ KV$, at $0 - 30\ A$, at a repetition rate of up to $200\ Hz$. Ideally, each high voltage and high current pulse is $20\ \mu s$ wide, with a flat top. The pulses provide high power density during the $20\ \mu s$ period. Between the pulses, the target loses heat by radiation to the chamber environment and from conduction to the supporting stage. The net power input for individual pulse is quite small, thus only a small temperature increase is expected for one pulse.

To calculate the equilibrium temperature or temperature rise over a longer period of time, we estimated the time averaged power from four major sources: heating by high voltage pulses, heat loss from conduction, radiation loss, and heat convection from the plasma. Because the plasma is on before pulsing starts, it is assumed that the target has reached an equilibrium temperature from plasma heating before the implantation begins. This equilibrium temperature is taken as the initial temperature to calculate the temperature rise from pulse heating. After the pulsing starts and the target is heated up, convection from the plasma can actually cool the target and cause a temperature gradient. However, in these studies, for the small metal sheets tightly coupled to the 5.970 in ID, 0.780 in thick stainless steel holder, convective cooling is small and the thermal gradient may be considered to be negligible [121]. Furthermore, it is assumed that for reasonable contact resistances and surface areas, reasonable emissivity difference between the base plate and metal sheets, the

temperature difference between the plate and the sheets is quite small, so the supporting plate and samples assembly can be treated as a single body, simplifying the calculation. The stage is connected to the HV input through a 1/4 in stainless steel tubing, inserted into the side of the stage so heat conduction through the HV connection is negligible. However, the target assembly is supported by a 2 in. ID, 3 in. long quartz rod, which is inserted in a stainless steel fixture centered at the bottom of the chamber. The heat loss from the conduction of the rod should be considered.

The lumped model is then justified for estimating the temperature for the PSII target [121, 122]:

$$mc_p \frac{dT}{dt} = Aq - A\epsilon\sigma(T^4 - T_0^4) - K_q A_q (T - T_b)/L_q \qquad \text{(Eq. 7.1)}$$

where A is the surface area of the target, q is the time-averaged heating effect from the pulsing on unit surface area, ϵ is the emissivity of the radiating surface, σ is the Stefan-Boltzmann constant, T_0 is the chamber temperature. The second term on the right hand side represents the radiation loss from the target assembly. The third term represents the heat conduction loss from the quartz rod, where K_q is the thermal conductivity of quartz, A_q the contact area, L_q is the length of the quartz rod. One end of the rod is assumed to have the same temperature as the target assembly, the other end have the same temperature as the chamber bottom, which is T_b. The heat loss due to the radiation from the rod surface is ignored, since the value is small compared to the other terms on the right side of Eq. 7.1. This assumption has also been justified afterwards using the obtained equilibrium target temperatures.

The initial temperature of the inside of the chamber and the target is assumed to be 400 K. The following material parameters are used [29]:

Material	Density ρ (kg/m^3)	$c_p(J/kgK)$ (at constant pressure at $25°C$)	Thermal Conductivity k (W/mK)
304 SS	8020	460	30
Ti	4500	523	21.9
Ta	16400	140	57.5
Nb	8570	265	53.7
Mo	10200	251	138
Si	2328	705	124
Quartz	2200	752	1.38

In this model, the heating from the energetic ions is treated as a surface heat flux. A volume heating process is only slightly more accurate since the ions actually deposit their energy over a finite depth, which can be characterized by the typical heat conduction length (considering transient heat conduction in a semi-infinite slab) [121]:

$$l = 2\sqrt{\kappa t}$$

where l is the length over which significant temperature change has occurred, $\kappa = k/(\rho C_p)$ is thermal diffusivity, t is the pulse width. For the pulse width used in our implantation, $t = 20\,\mu s$, considering different materials properties, we have:

	304 SS	Titanium	Tantalum	Niobium	Molybdenum	Silicon
$l(\mu m)$	25.5	27.3	44.8	43.5	65.7	77.7

Typical implantation depth for the above calculated materials is several thousand angstroms, much less than the typical heat conduction length. Thus the volumetric heating effects can be ignored and surface heat flux can be used in our calculation.
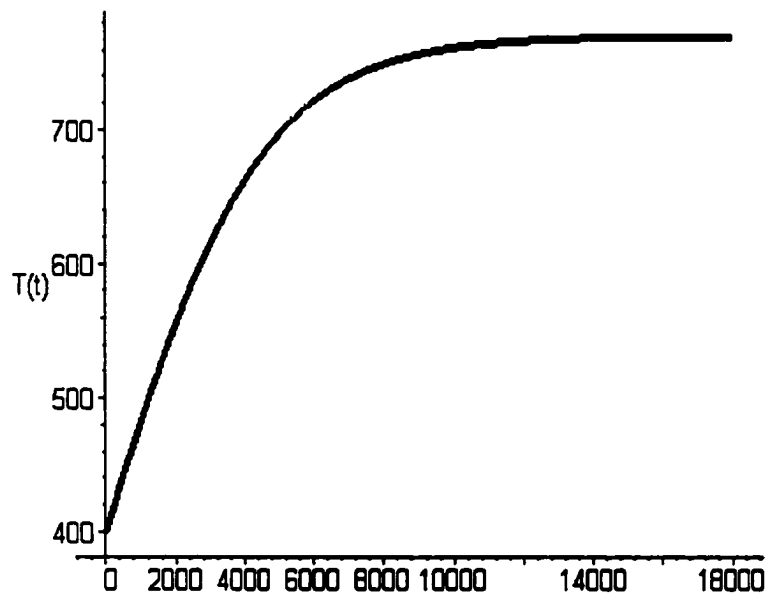
Figure 7.4. Target temperature (in Kelvin) as a function of time in seconds. The applied pulse is 30 KV at 100 Hz. The target surface emissivity is 0.2.

Eq. 7.1 was solved numerically using Maple. The typical results for stainless steel plate with a pulse repetition rate of 100 Hz and different emissivities are shown in Fig. 7.4 ($\epsilon = 0.2$) and Fig. 7.5 ($\epsilon = 1.0$). In the plots, t represents elapsed time in seconds, T represents target temperature in Kelvins. For all the calculations, the input pulse is assumed to be 30 KV, with an average current of 15 A and duration of $20\mu s$. The secondary electron emission coefficient at 30 KV was also considered to adjust the power input from pulsing. As shown in Fig. 7.4 and Fig. 7.5, the target temperature rises sharply at the beginning, reaches equilibrium value at a later time, depending on the balance of the heating, conduction heat loss, and radiation cooling process. It takes longer for target with lower emissivity to reach equilibrium temperature. Lower emissivity also leads to higher ultimate temperature. Fig. 7.6 shows the equilibrium temperatures obtained for different pulse repetition rate and target emissivity. Higher repetition rate of pulse provides more time-averaged heating of the target, which leads to higher equilibrium temperature especially with target having low emissivity. However, at pulse repetition rate of 50 Hz, the equilibrium temperature is only around $259°C$ if the surface emissivity is 0.6, which is typical for polished steel; or $236°C$ if the emissivity is 0.8, for steel with a shiny layer of oxide [29]. Fig. 7.6 also applies to all the other materials listed above, since the ultimate temperature is a function of emissivity, chamber temperature, and the input heating power. Target equilibrium temperature is not a function of target mass and heat capacity.

Lower chamber temperature results in slightly lower equilibrium target temperature, due to more radiation heat loss to the environment, as shown in Fig. 7.7.
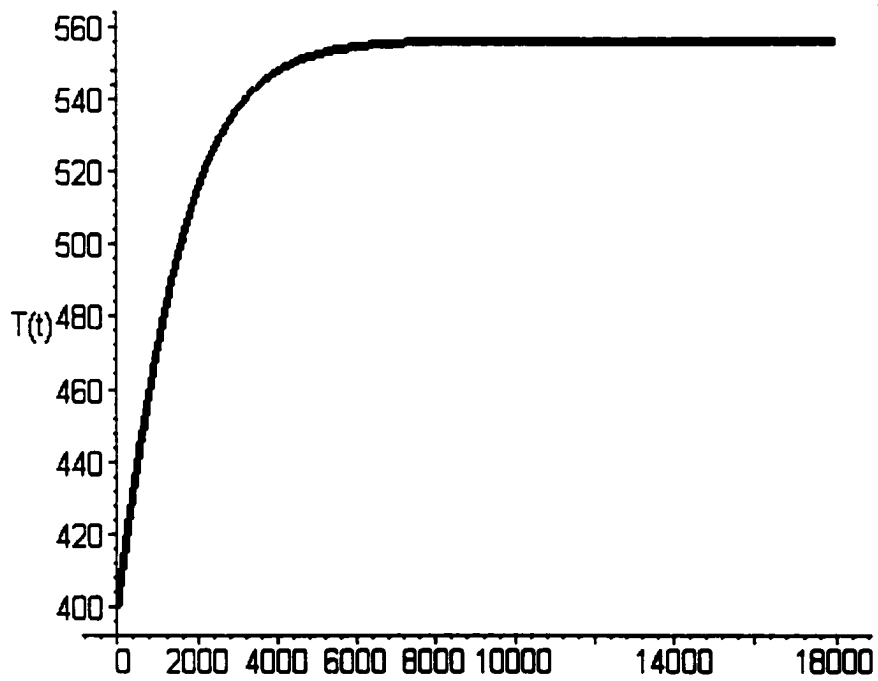
Figure 7.5. Target temperature (in Kelvin) as a function of time in seconds. The applied pulse is 30 KV at 100 Hz. The target surface emissivity is 1.0.
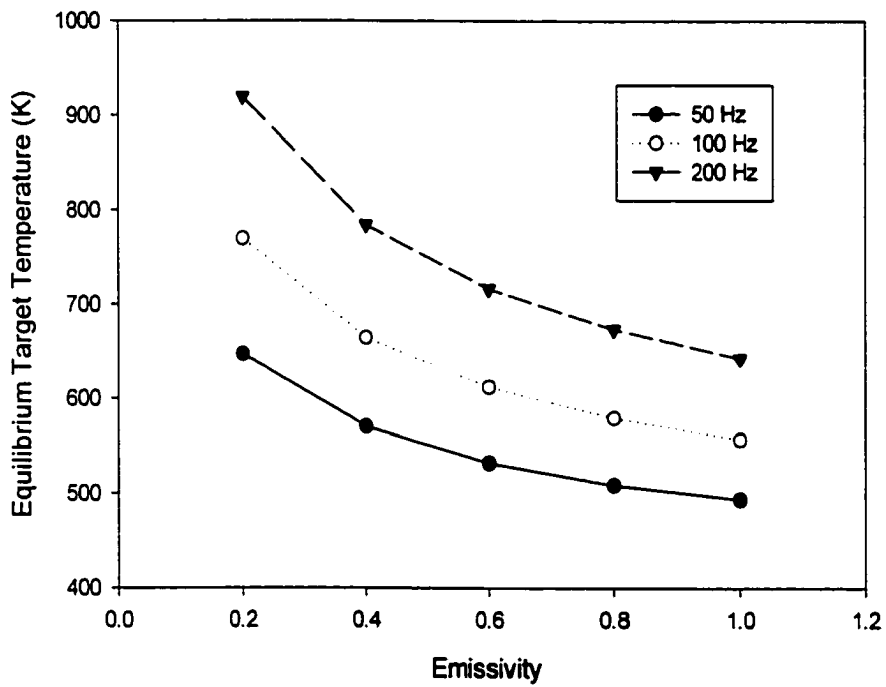
Figure 7.6. Target equilibrium temperature for different pulse repetition rate and surface emissivity. The chamber temperature used is 400 K.
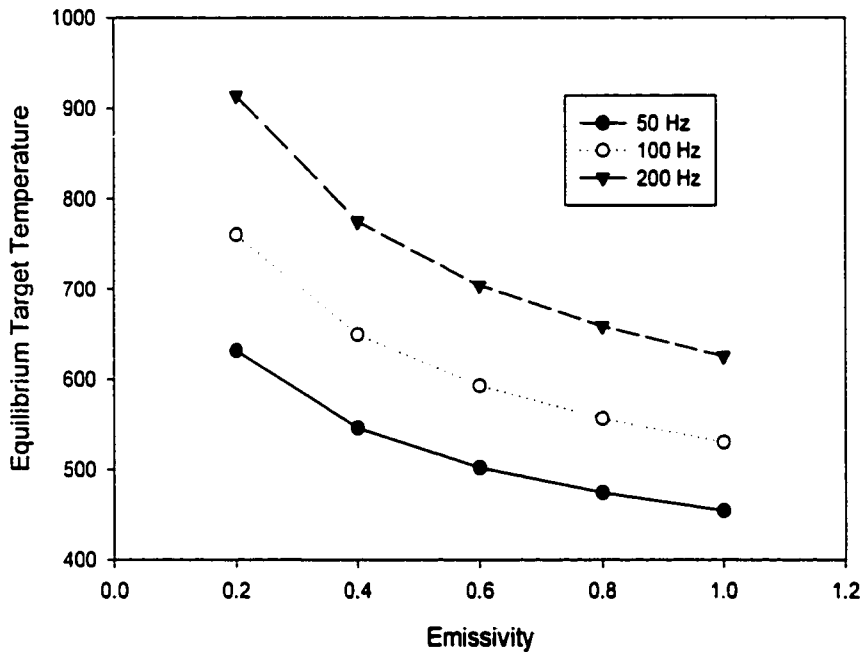
Figure 7.7. Target equilibrium temperature for different pulse repetition rate and surface emissivity. The chamber temperature used is 300 K.

The use of time-averaged heating by HV pulses for our calculations is justified by the following considerations. The temperature rise from one 20 μs wide pulse is calculated to be 0.18 K. Once the pulsing starts, the target temperature ratchets up, increasing during the pulse-on period, and decreasing during the pulse-off period. However, because the radiation heat loss is small compared to heating at low target temperatures, the target temperature increases for each pulse cycle. At high target temperatures, the radiation loss, which becomes the dominant heat loss mechanism, increases to be comparable to or equal to the heating from one HV pulse. Therefore the net temperature change for each pulse cycle decreases and the target temperature reaches a quasisteady state in which the temperature at the end of the cycle is identical to the temperature at the begining of the cycle. The target temperature history is illustrated in Fig. 7.8, where the time period and heating effect are exaggerated to show this effect. For the actual PSII conditions we are interested in, the heating period is much shorter (20 μs) compared to the cooling period, which is 4980 μs for a pulse repetition rate of 200 Hz, allowing more time for the target to cool. The temperature swing is also much smaller for each pulse (0.18 K). The actual temperature history closely resembles a smooth curve.

It is concluded from the above calculations that active target cooling is necessary for higher pulse repetition rate and for heat sensitive samples. One way of doing this is to use a water-cooled sample stage. If the stage is kept near room temperature by active water-cooling and is in good thermal contact with the back of the sample assembly, the cooling effect can be estimated. Here, the same target assembly is considered as for above calculations. Assume that the whole bottom of the assembly is cooled by the sample stage.
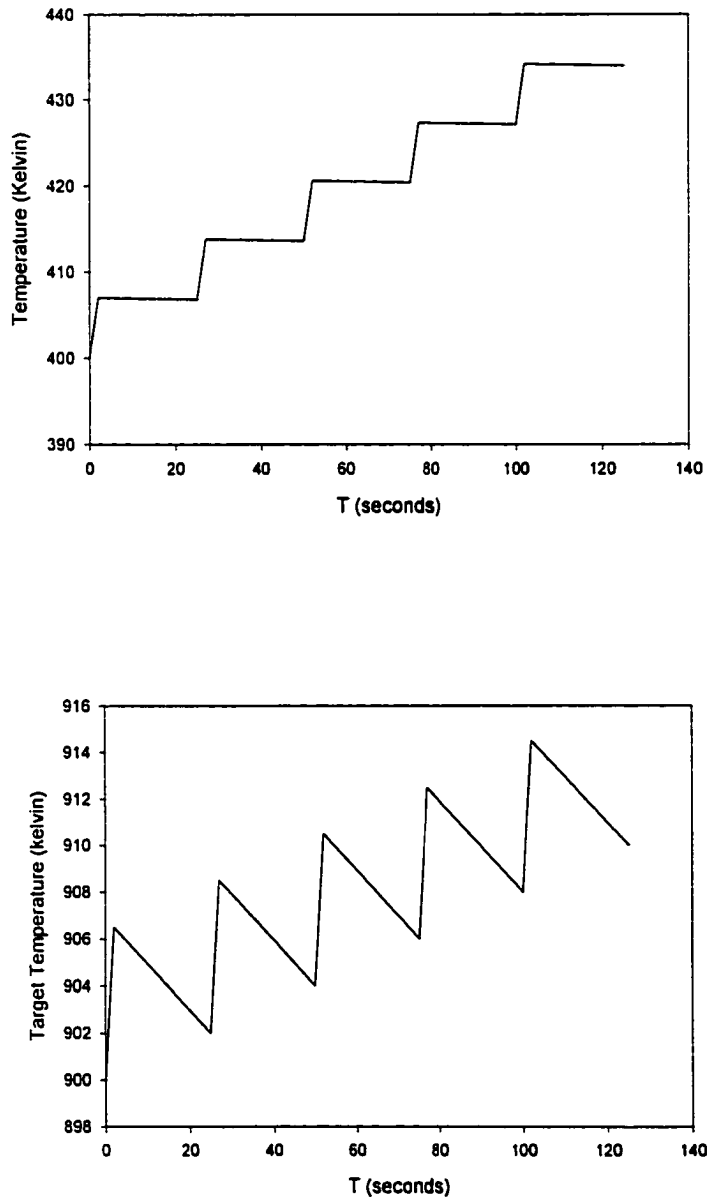
Figure 7.8. Schematic of temperature history for the target. Time periods and temperature swings are exaggerated relative to typical PSII target temperature histories.

Only the top and side of the assembly are implanted, heated, and cooled by radiation heat

loss, so a cooling term is added to the equation:

$$mc_p\frac{dT}{dt} = Aq - A\epsilon\sigma(T^4 - T_0^4) - A_ch(T - T_s)$$ (Eq. 7.2)
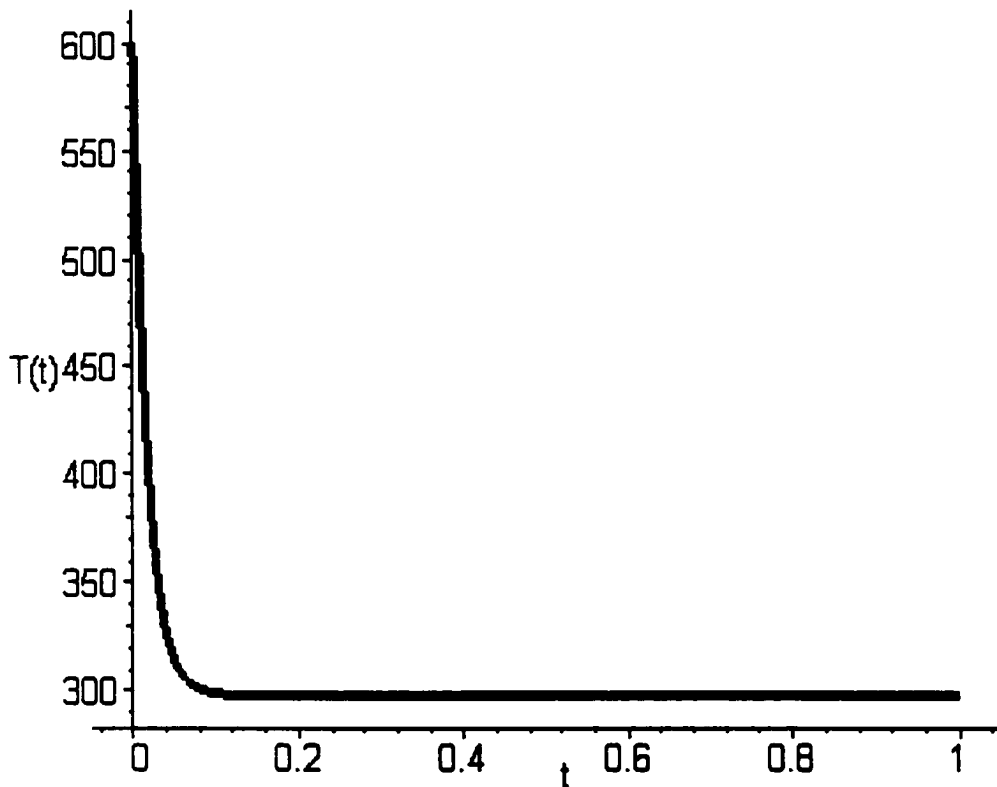
Figure 7.9. Target temperature history as a function of time. Assume that the target temperature has reached 600 K by pulse heating before cooling is turned on at t=0. Assume that 0.1 mm thick silver layer is used for heat conduction between the target and the cooled stage, which is at 298 K by active water cooling.
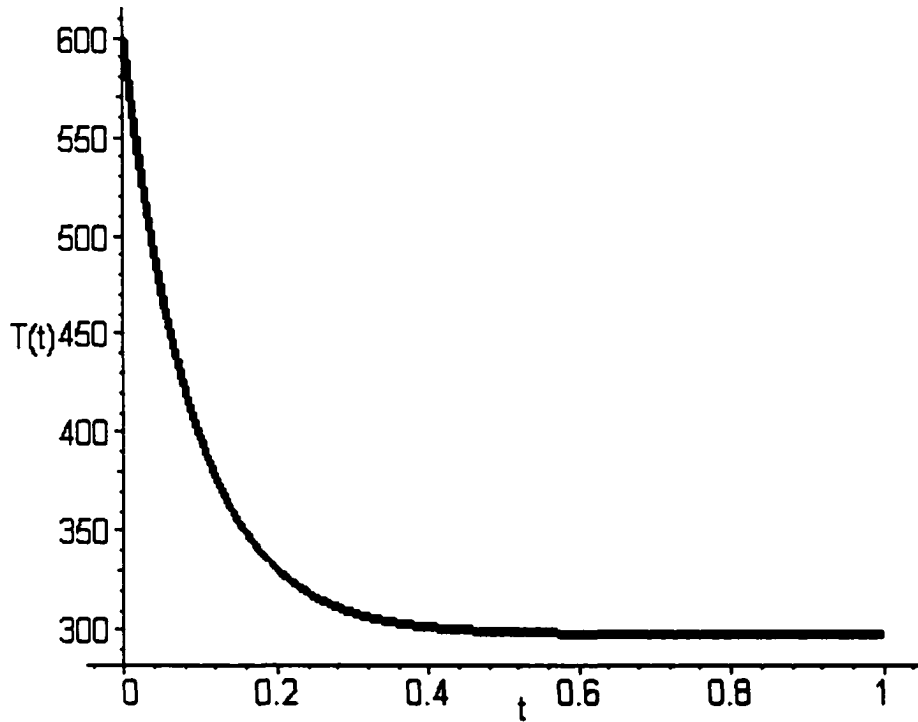
Figure 7.10. Target temperature history as a function of time. Assume that the target temperature has reached 600 K by pulse heating before cooling is turned on at t=0. Assume that 0.1 mm thick indium layer is used for heat conduction between the target and the cooled stage, which is at 298 K by active water cooling.

A_c is the contact area between the target assembly and the cooling stage, T_s is the cooling stage temperature, and h is the heat transfer coefficient of the heat conducting material used between the stage and the assembly. Assume that there is a 0.1 mm thick heat conducting material between the target and the stage, and the stage surface is kept at 298K by water cooling. Also assume the chamber wall temperature to be 400 K and the target has reached 600 K because of the pulse heating. If the heat conducting material is silver, the heat transfer coefficient would be 4.3×10^6 W/m^2K, obtained by dividing thermal conductivity by the layer thickness. Calculation gives the temperature history after the cooling is turned on in Fig. 7.9, showing that the target temperature would drop to the stage temperature (298 K) in less than a second (around 0.1 second). If Indium is used, the heat transfer coefficient would be 8.16×10^5 W/m^2K for a 0.1 mm thick layer. Similar calculations can be performed and the result is shown in Fig. 7.10. The target assembly can also be cooled to 298 K in less than a second (around 0.5 second). Since copper or other good heat conducting materials are usually used to construct cooling stages, the time it takes for the stage to reach 298 K was ignored. Similar calculations were also performed for targets that had already reached higher temperatures (900 K or 1000 K) by pulse heating, showing that it takes less than a second for the target to be cooled to 298 K.

A calculation considering the heating effect of the individual HV pulse was performed since the cooling stage was found to cool the target to stage temperature in very short period of time. It was assumed that the starting temperature for the stage was 400 K. Eleven HV pulses were applied to the target raising the target temperature to 401.98 K, before the cooling was turned on. The pulse repetition rate was 200 Hz. The pulse-on time

was 20 μs and the pulse-off time was 4980 μs for each heating cycle. Cooling was constant once it was turned on. The temperature history (Fig. 7.11) showed that the target temperature dropped from 401.98 K to 298 K in about 0.1 second, confirming the results above obtained using time-averaged heating of the HV pulses (Fig. 7.9). Enlarged plots of the temperature curve were also made and are shown in Fig. 7.12 and Fig. 7.13. As shown in Fig. 7.12, the target temperature rise was 0.18 K for each pulse. Because the radiation loss was small at low temperatures (around 400 K), temperature drop during the pulse-off period was not significant. After the cooling was turned on (as shown in Fig. 7.13), heat generated by each pulse was slightly smaller than the conduction heat loss to the cooled stage, resulting in small temperature drop ($< 0.1\ K$) for the pulse-on period. The temperature drop for the pulse-off period started from 26.36 K at $t = 6 \times 10^{-2}$ s, decreased to 0.14 K at $t = 1.5 \times 10^{-1}s$, as the temperature difference between the target and the stage decreased.

7.3.2 Profile Calculation of Nitrogen Concentration

The profile calculation of low dose implantation helps to understand how implanted ions of the same energy interact with different substrates. Nitrogen concentrations in Ti, Nb, Mo and Ta substrates were calculated by Profile Code. Profile Code was developed by Implant Sciences Corporation, for rapid prediction of implantation profiles under a variety of conditions, such as different substrate materials, implantation species, doses, incident angles, and implantation voltages. The Profile Code results are usually equivalent to those generated by Monte Carlo programs, such as TRIM^{TM}. The calculations of Profile Code
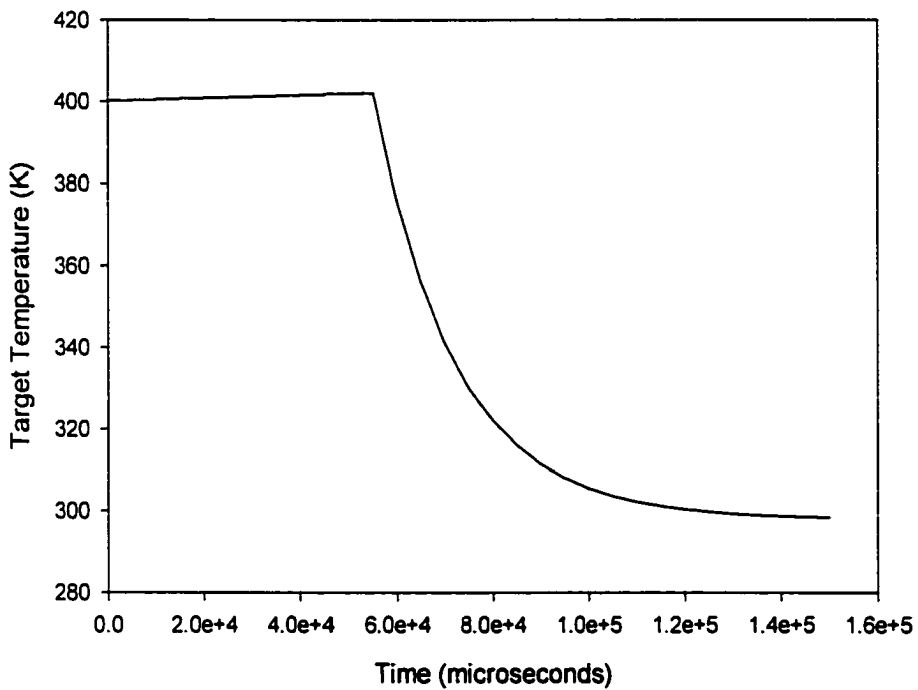
Figure 7.11. Calculated target temperature history showing the heating from a train of pulses. The target starting temperature was assumed to be 400 K. Eleven HV pulses were applied before the stage cooling was turned on (0 - 5.5 × $10^4 us$). The pulse repetition rate was 200 Hz. Cooling was turned on at 5.5 × $10^4 us$ when the target was at 401.98 K.
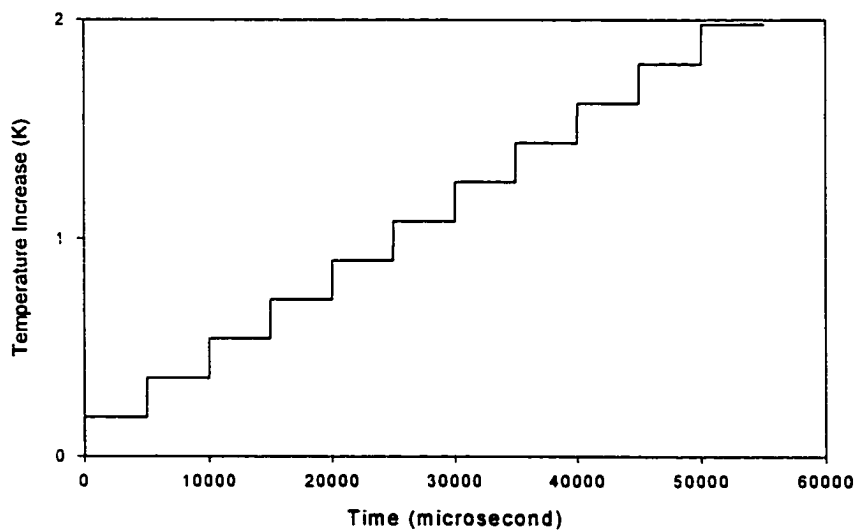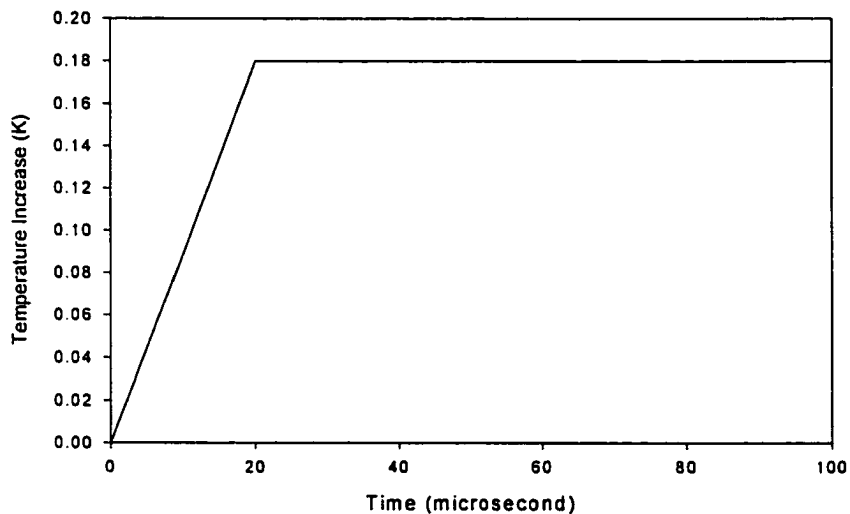
Figure 7.12. Target temperature history calculated showing the heating effect of individual HV pulses. The pulse repetition rate was 200 Hz.
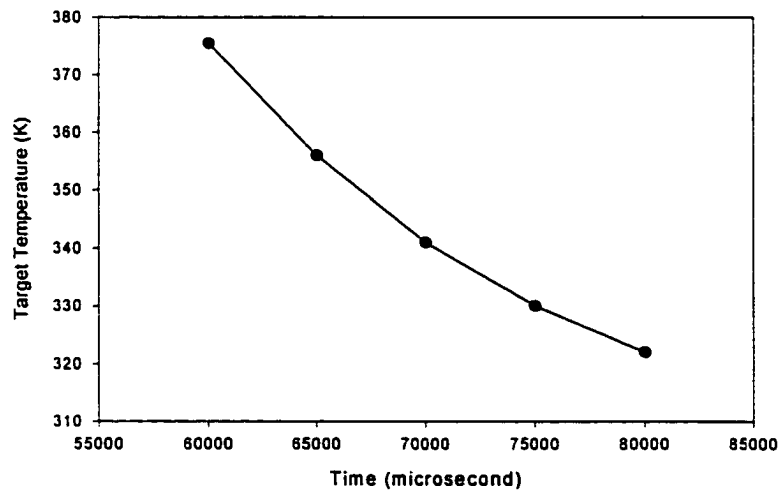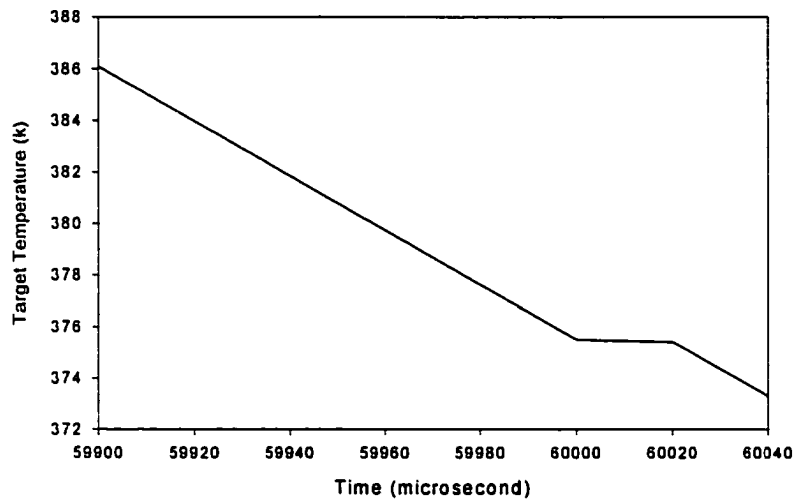
Figure 7.13. Target temperature history which considers the heating effect of individual HV pulse and the cooling from the stage. The pulse was 20 μs wide and the repetition rate was 200 Hz. The target temperature was 401.98 K after heated by 11 HV pulses. The cooling was turned on at $T = 55000$ μs.

are usually completed in a matter of seconds instead of hours as required by other codes [102]. It is considered a powerful research tool for experiment design, and for understanding experimental depth profiles. For the following calculations, an implantation voltage of 30 KV and applied dose of $1 \times 10^{17}/cm^2$ was used. As shown in Fig. 7.14, nitrogen penetrates deepest into the Ti substrate for the same applied dose and implantation voltage. Its peak concentration is 19.1% at 584 Å. Retained dose is 92.4% of the applied dose, or $9.24 \times 10^{16}/cm^2$. The nitrogen peak concentration is 24.1% at 304Å for Nb substrate, 19.3% at 287Å for Mo, and 20.4% at 220Å. It is obvious that the peak position is closer to the surface for substrate with larger z values. The sputter loss is 61 Å for Ti, 78 Å for Nb, 66 Å for Mo, and 62 Å for Ta. Retained dose is 83.5% for Nb, and 74.5% for Mo, and 64.9% for Ta, which is higher for substrate with low-z elements. Ions are assumed to be incident perpendicularly on the substrate surface. These results are valid for pure substrates, without any surface oxide or carbide layers. With the existence of these surface layers, the sputtering coefficient would be significantly lower than the prediction of Profile Code [102].

7.3.3 Characterization of Implanted Samples

Optical Microscopy Study of the Sample Surface

The implanted Ti sheets show a golden color which is characteristic of stoichiometric TiN. Optical microscope pictures of implanted and un-implanted Ti substrate areas are shown in Fig. 7.15 and Fig. 7.16. They indicate that the implantation process helped to
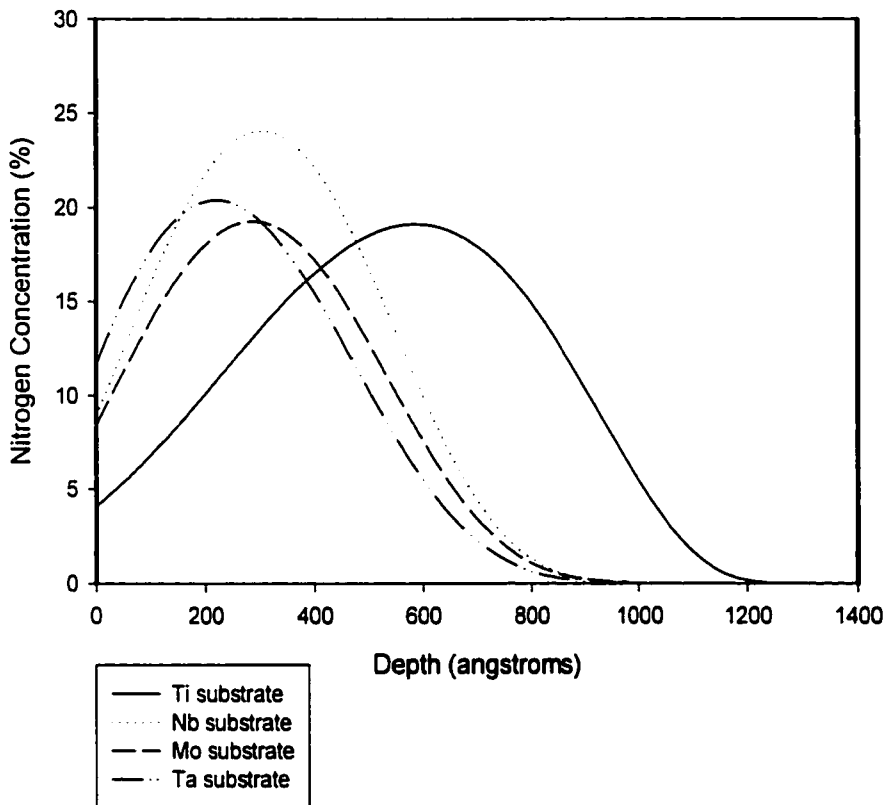
Figure 7.14. Profile Code calculation of nitrogen concentration in Ti, Nb, Mo and Ta substrates. The implantation voltage is 30 KV and the implantation dose is $1 \times 10^{17}/cm^2$.

smooth out the sharp features and possibly to anneal the surface. This is important for the implantation treatment of FEL electrodes for suppressing field emission. Ti is also being used to make the FEL electrode because of its high hardness. The implanted nitrogen forms nitride and hardens the Ti surface. The conditioning and smoothing effect of the PSII process also removes sharp surface protrusions, which are believed to be locations of high field strength and sources of field emission.

The nitrogen implanted Ta shows a dark blue color. Optical microscope pictures do not show apparent differences of surface morphology between the implanted and un-implanted area (Fig. 7.17 and Fig. 7.18).

Nitrogen implanted Mo shows a silver metal color. Compared to the implanted area, the un-treated area shows a yellow-green hue. Optical microscope pictures of implanted and un-implanted Mo surface are shown in Fig. 7.19 and Fig. 7.20. The implanted area is apparently smoother than the un-implanted area. The implantation process possibly annealed the Mo surface, too.

The nitrogen implanted Nb surface shows a pale golden color. However, the optical microscope study did not show any apparent difference for the implanted and un-implanted substrate (Fig. 7.21 and Fig. 7.22).

Nitrogen implanted stainless steel shows a uniform dark brown color. Optical micro-scope picture of the implanted and un-processed sample surfaces are shown in Fig. 7.23 and Fig. 7.24. There are no signs of arcing or other damage on the implanted area. The implanted substrate has a surface smoothness at least as good as the surface finish of the un-treated substrate.

Figure 7.15. Optical microscope picture of nitrogen implanted Ti substrate.

Figure 7.16. Optical microscope picture of un-implanted Ti substrate
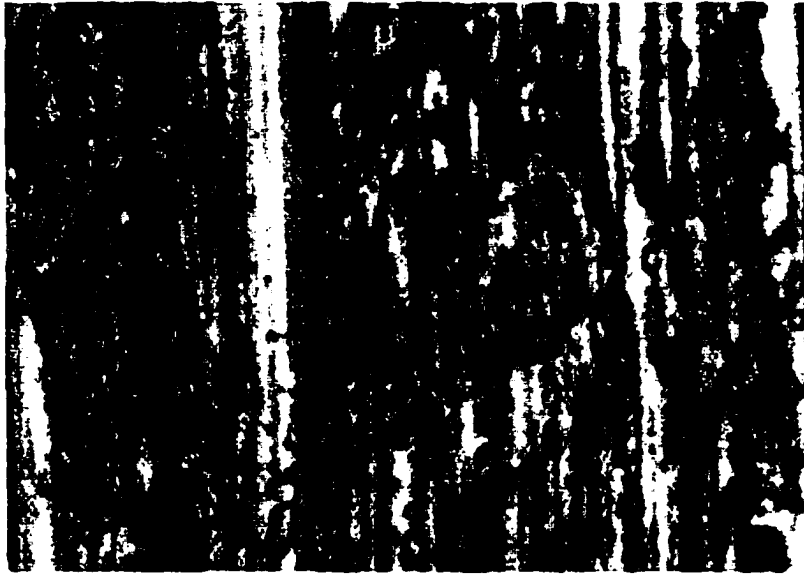
Figure 7.17. Optical microscope picture of un-implanted Ta substrate.

Figure 7.18. Optical microscope picture of nitrogen implanted Ta substrate.
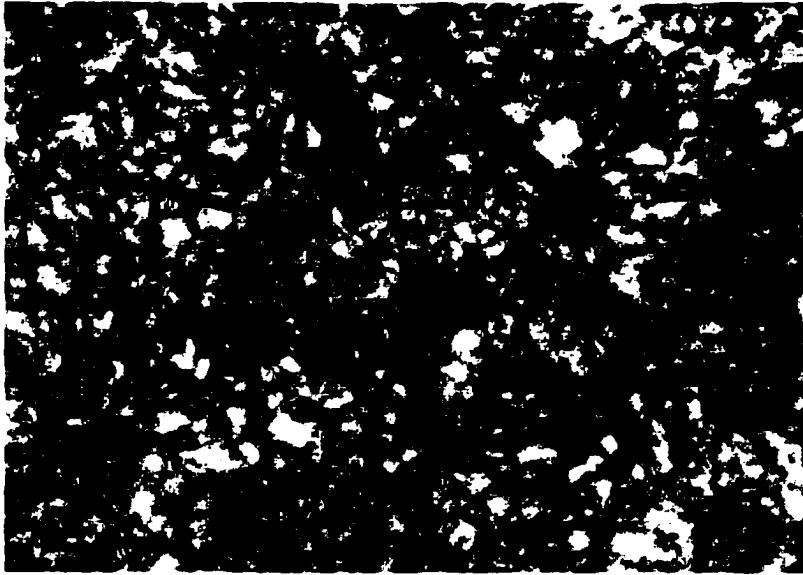
Figure 7.19. Optical microscope picture of nitrogen implanted Mo substrate.
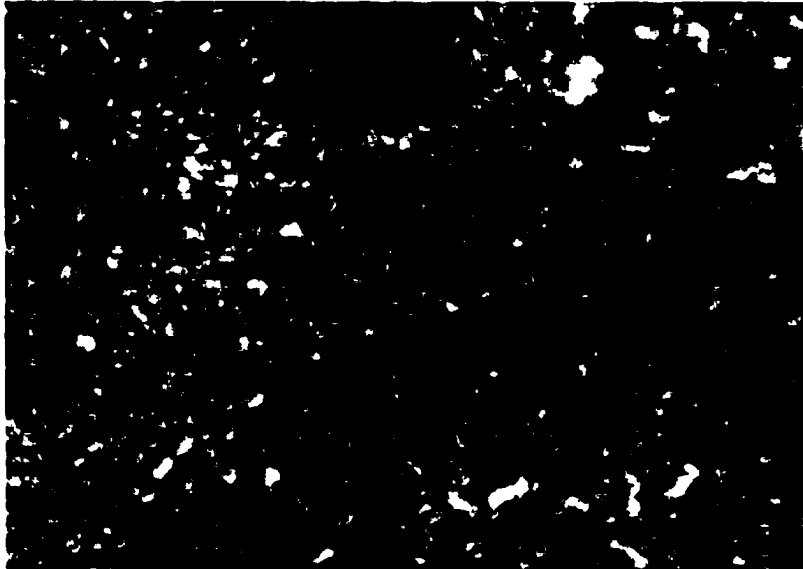
Figure 7.20. Optical microscope picture of un-implanted Mo substrate.
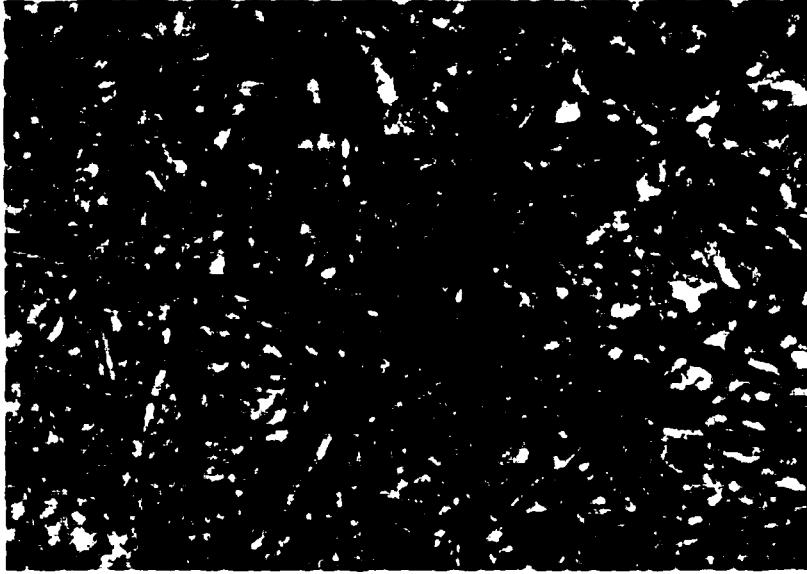
Figure 7.21. Optical microscope picture of un-implanted Nb substrate.
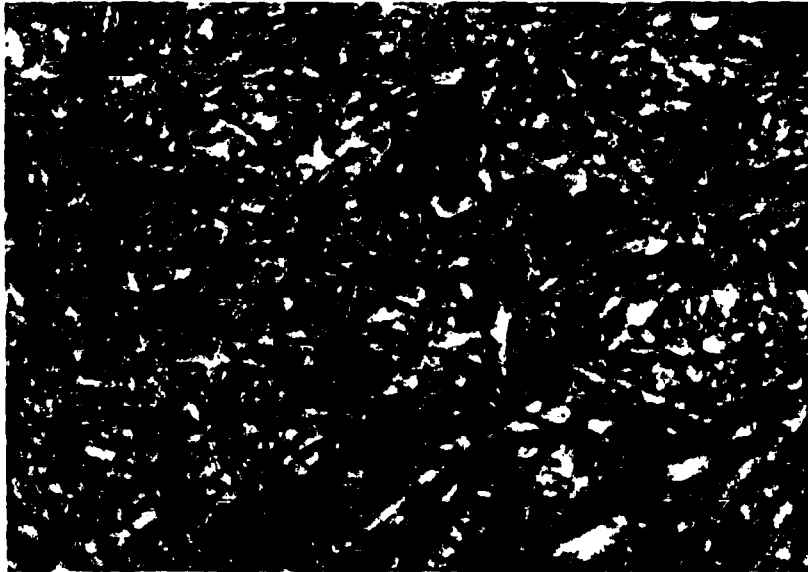
Figure 7.22. Optical microscope picture of nitrogen implanted Nb substrate.
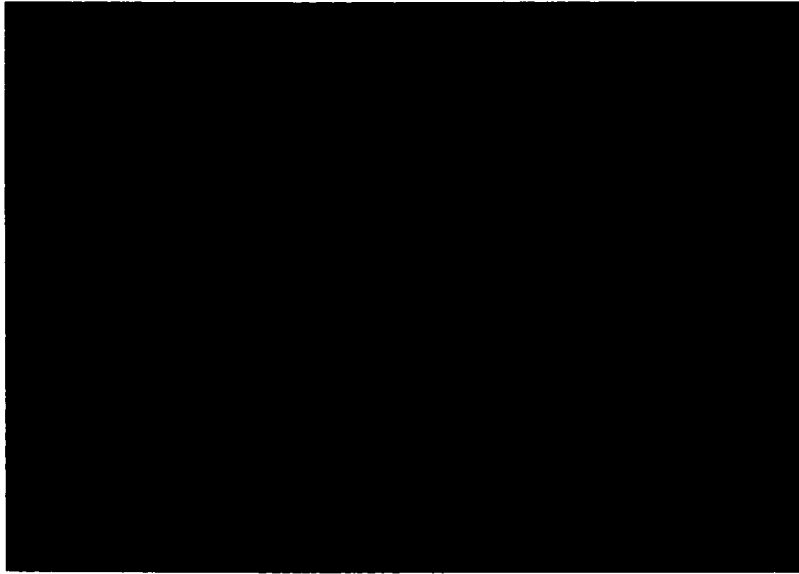
Figure 7.23. Optical microscope picture of 0.03 μm mirror finish 304 stainless steel substrate.
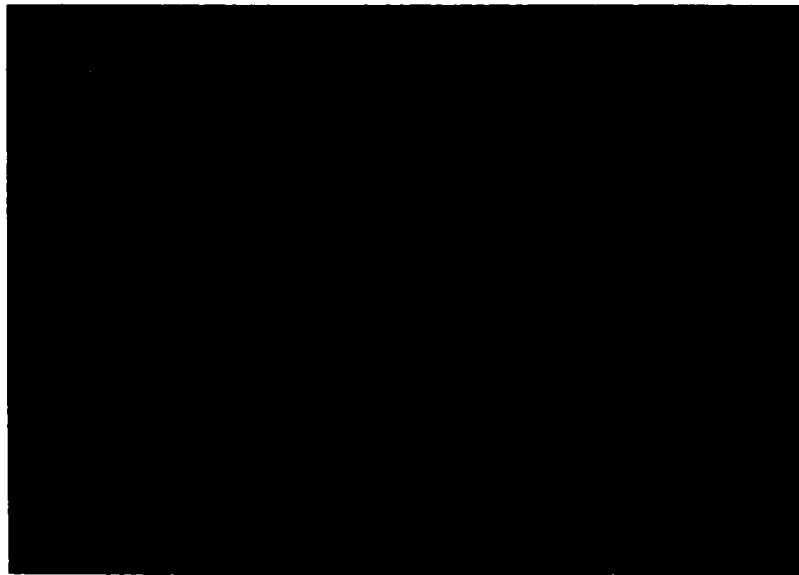
Figure 7.24. Optical microscope picture of nitrogen implanted mirror finish stainless steel substate.

Surface Hardness Study

The surface hardness of the implanted and un-implanted substrates are studied using different load values. Because the implanted layers are very thin compared to the indentation depth, the Vickers criteria were not rigorously satisfied. Some attempt to compensate for this can be made by measuring the hardness value as a function of load (indentation depth) and extrapolating the resulting curves to their values at zero loads. The general problem of measuring the hardness of ultra-thin, very hard layers over soft substrate has been discussed in reference [61]. The measurements reported here can be used as a qualitative indication of the implanted layer hardness, which show that the implanted samples are indeed harder (probably much harder) than the bare samples (Fig. 7.25, Fig. 7.26, Fig. 7.27, Fig. 7.28, and Fig. 7.29) The surface hardness results for Mo substrate are shown in Fig. 7.27. Because of the surface roughness, the reading at $15g$ load is very unreliable and thus is not included in the graph. TiN layer that has larger ratio of thickness to indentation depth yields larger hardness values, confirming this qualitative result (see below for AES depth profiles of implanted nitrogen concentration).

AES Depth Profile of Implanted Nitrogen

The AES spectrum of the implanted Ti surface is shown in Fig. 7.30. Elements present on the surface in trace amounts include carbon, nitrogen, oxygen, titanium, calcium, sodium, aluminum, copper, and sulfur. Because of surface absorbed ambient gas species, carbon, nitrogen, and oxygen have prominent peaks. The AES depth profile of implanted nitrogen is shown in Fig. 7.31. The Ti-N peak overlap and the influence of oxygen
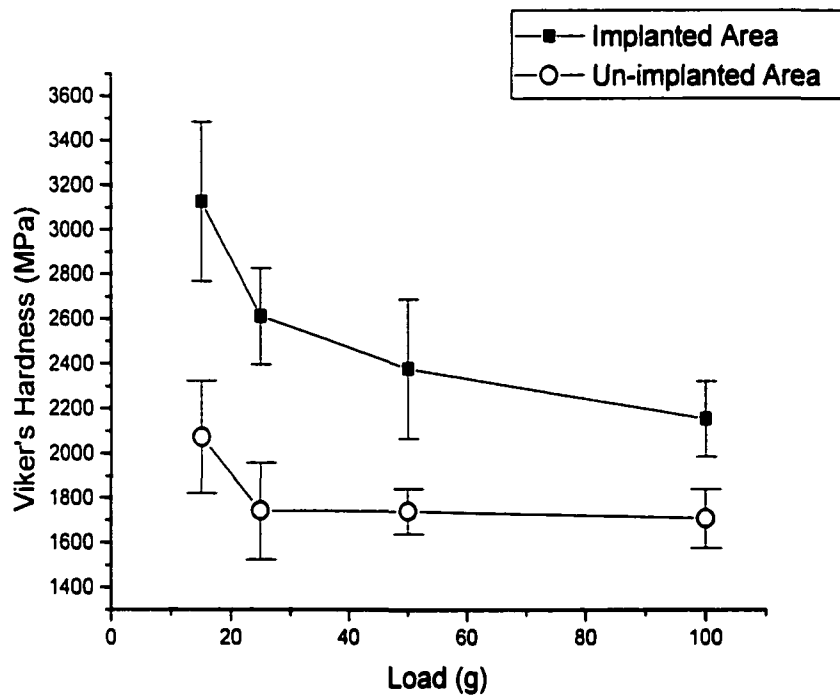
Figure 7.25. Surface hardness test results for nitrogen implanted and un-implanted Ti substrates.
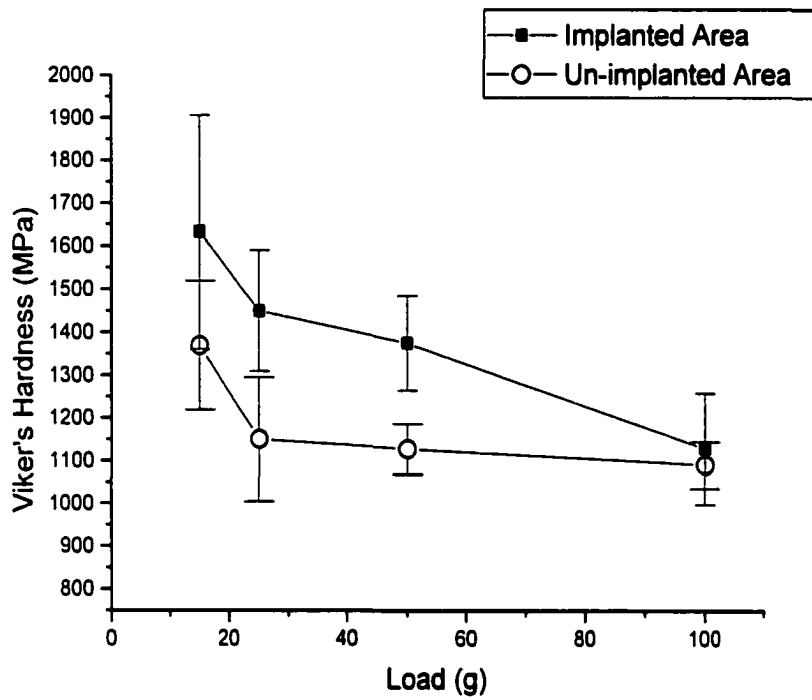
Figure 7.26. Surface hardness test results for nitrogen implanted and un-implanted Ta substrates.
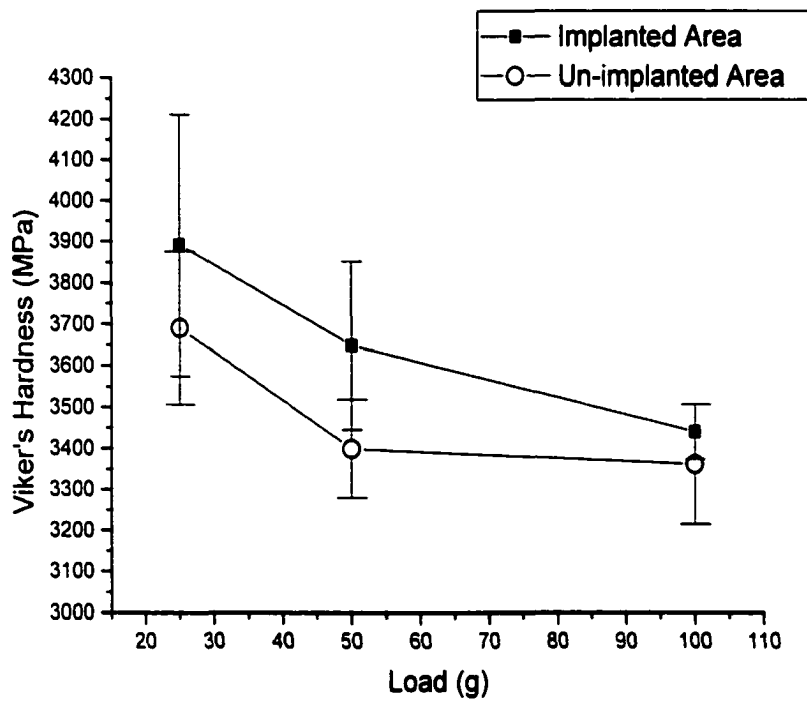
Figure 7.27. Surface hardness test results for nitrogen implanted and un-implanted Mo substrates.
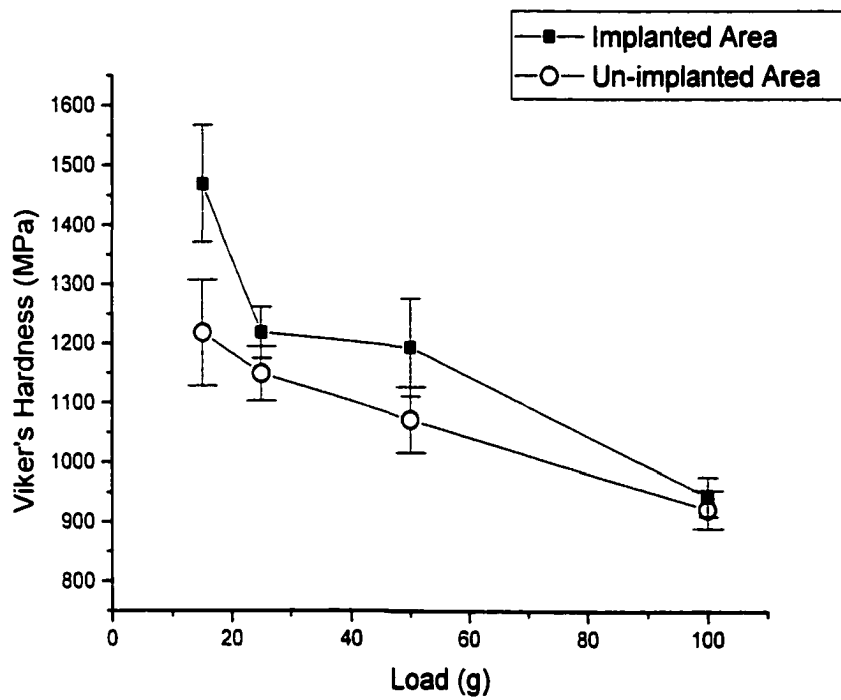
Figure 7.28. Surface hardness test results for nitrogen implanted and un-implanted Nb substrate.
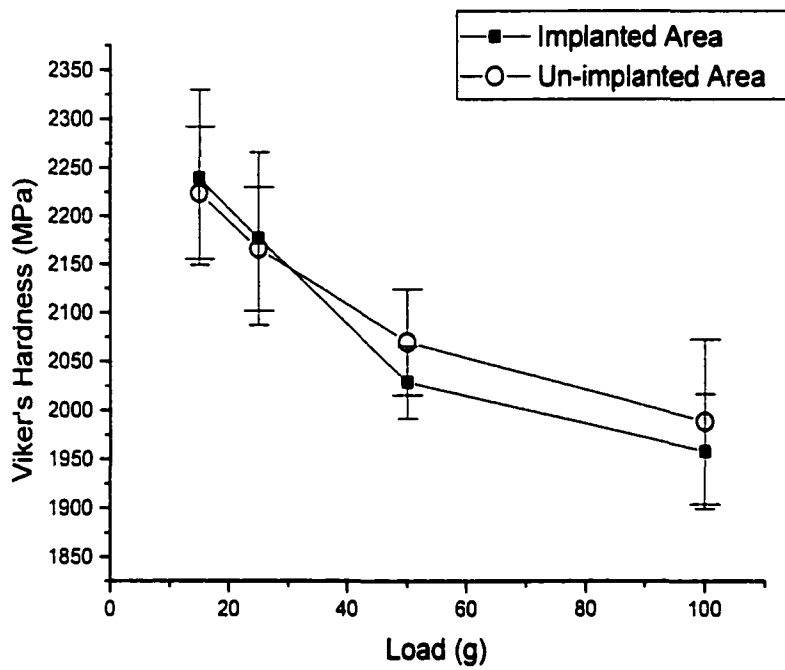
Figure 7.29. Surface hardness test results for nitrogen implanted and un-implanted mirror finish 304 stainless steel substrate.

on the Ti_{385}/Ti_{420} peak ratio was considered when calculating the nitrogen concentration [101]. Nitrogen concentration is around 60-64% percent for the top surface (0 − 950Å), except for the topmost 200Å range, where the higher concentration of oxygen from the surface oxides prevent more nitrogen from reacting with the titanium. The oxygen concentration decreases from about 25% to below 3% in 0 to 800Å range. Nitrogen concentration slowly decreases after a depth of 1000Å. Carbon, aluminum, and silicon are of very low concentration throughout the sputtered range; they are intrinsic impurities in the metal. Sulfur was not plotted for the depth profile because it was not detected except at the surface, where it was only 0.5%.

The almost constant concentration of implanted species for the top depth range is characteristic of high dose implantations. The concentration of implanted species usually saturates at the stoichiometric level for each depth. This can also be illustrated by calculation results from Profile Code, as shown in Fig. 7.32 and Fig. 7.33. At a dose of $6 \times 10^{17}/cm^2$, the nitrogen concentration begins to saturate for depth around 800 Å. As the dose is further increased to $1 \times 10^{18}/cm^2$, the small gap at the top surface is further filled and the layer thickness increased from around 1500 Å (Fig. 7.32) to 2000 Å (Fig. 7.33). The implanted layer has a constant nitrogen concentration for most of the implanted range, which is very similar to a deposited stoichiometric TiN film.

It is noticed that the nitrogen concentration in the Ti substrate for the top 200 Å to 1000 Å range is higher than 50%, the stoichiometry level of TiN, and therefore higher than the 45% level predicted by Profile Code. Titanium is often used as vacuum pumping material [123,124] wherein evaporative or sputtering processes are used to produce nascent
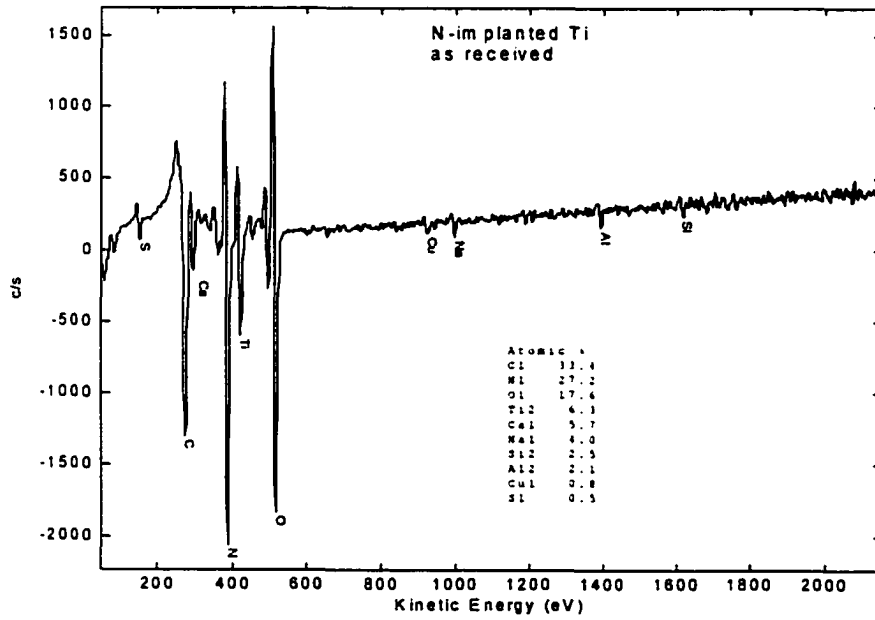
Figure 7.30. AES spectrum of the implanted Ti surface.
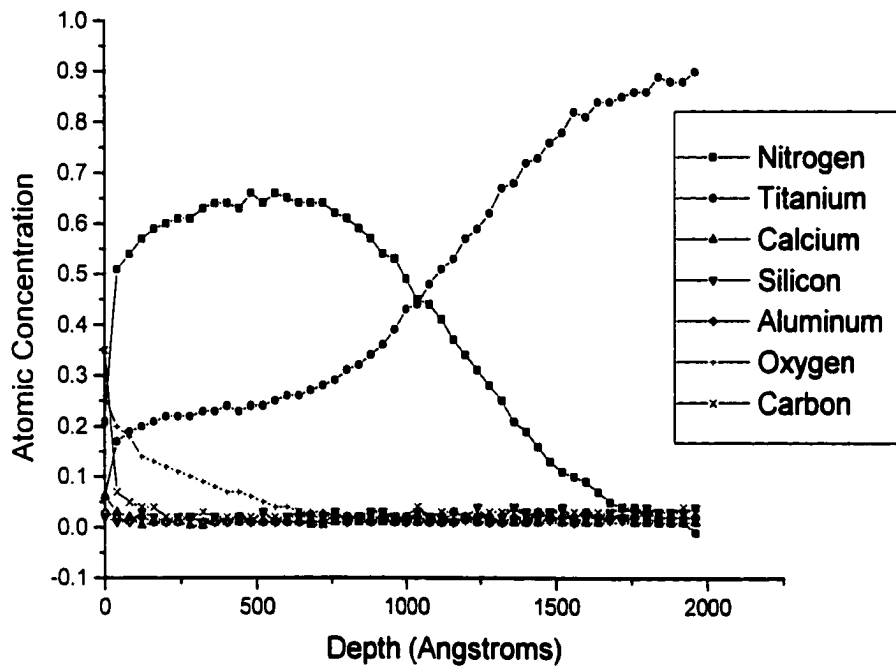
Figure 7.31. Concentration depth profile of a nitrogen implanted Ti substrate obtained by AES depth profiling

Ti films, which provide gas-absorbing power. We believe that solid solutions of nitrogen are also formed on our Ti substrates. The micro-structure of the substrate also influences the retained concentration of nitrogen. It was found in the sample preparation process that the Ti sheet is porous and mechanically weak. It is also quite possible that excess nitrogen can be trapped between the Ti particles and the sputtered particle surfaces, causing higher nitrogen concentration in these samples. Other studies [120] have found nitrogen concentrations as high as 70% in ion implanted and high temperature annealed TiN layers. Our implanted nitrogen concentration profile has an elongated tail. This may be caused by the elevated temperature. As shown in Fig. 7.6, at a repetition rate of 100 Hz and emissivity of 0.8, the target temperature can reach ~300°C, sufficient to allow for enhanced diffusion to occur.

The AES spectrum of nitrogen implanted Ta is shown in Fig. 7.34. Tantalum, nitrogen, carbon, oxygen, and calcium are detected. Carbon and oxygen were probably mainly from the surface absorbed gas molecules, resulting from long duration exposure to air prior to analysis. The AES concentration depth profile are shown in Fig. 7.35. The nitrogen concentration is around 40% for the top 450Å range, decreasing slowly to below 10% after 1150Å. The topmost 50Å range also contains less nitrogen due to the higher oxygen concentration in that range. It also shows a long tail, probably due to diffusion caused by elevated substrate temperature.

The AES spectrum of an implanted Mo sample is shown in Fig. 7.36. It includes peaks for Mo, C, N, Cu and Al. Again, the high concentration of C and O on the surface can be explained by surface absorbants. The AES concentration depth profile is shown in
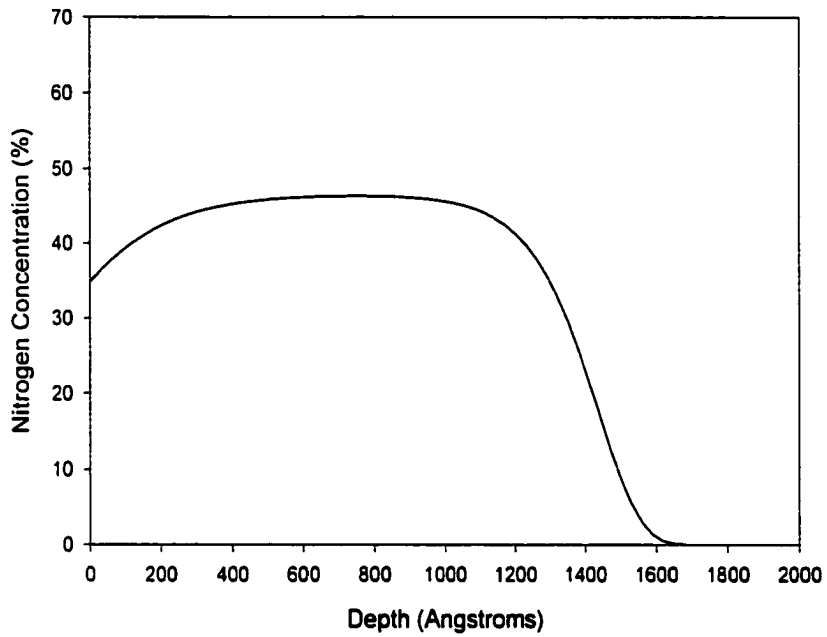
Figure 7.32. Profile Code calculation of nitrogen concentration in a Titanium substrate for implantation voltage of 30 KV and dose of $6 \times 10^{17}/cm^2$.
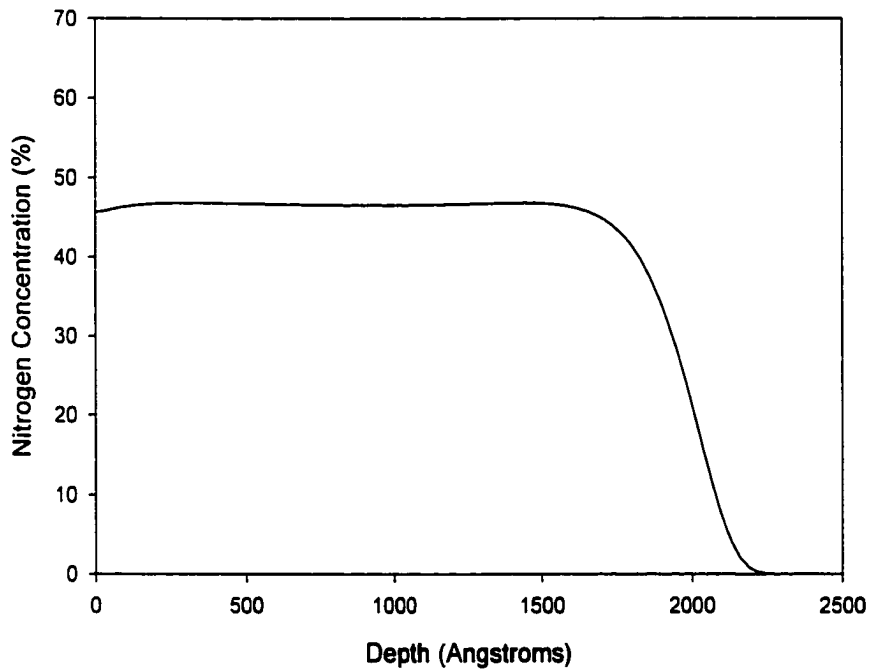
Figure 7.33. Profile Code calculation of nitrogen concentration in a Titanium substrate for implantation voltage of 30 KV and dose of $1 \times 10^{18}/cm^2$.
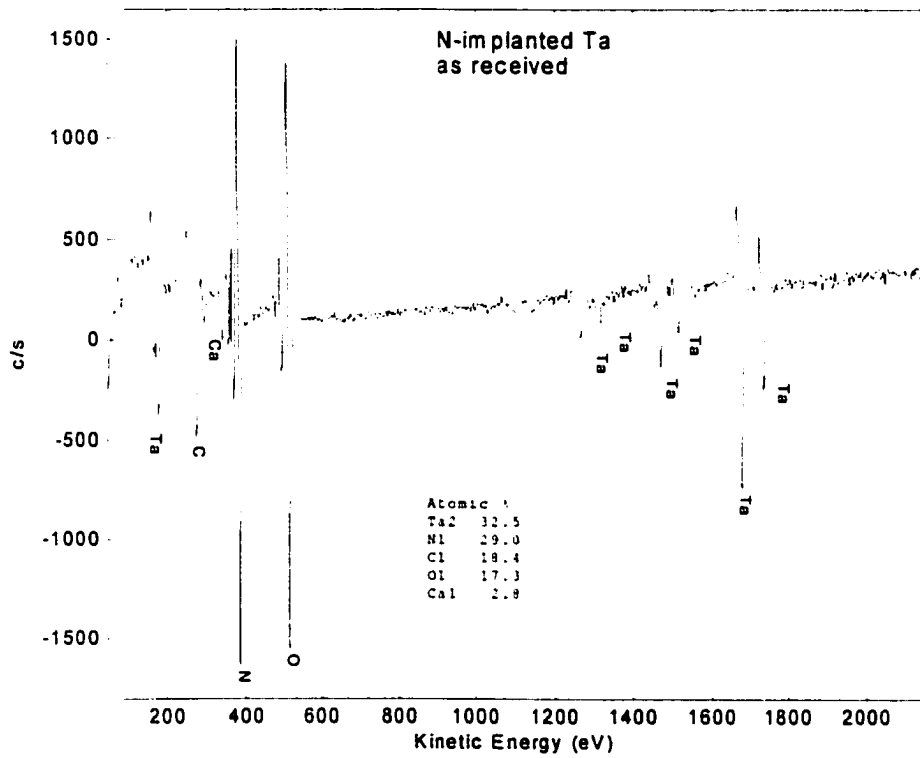
Figure 7.34. AES spectrum of a nitrogen implanted Ta substrate surface.
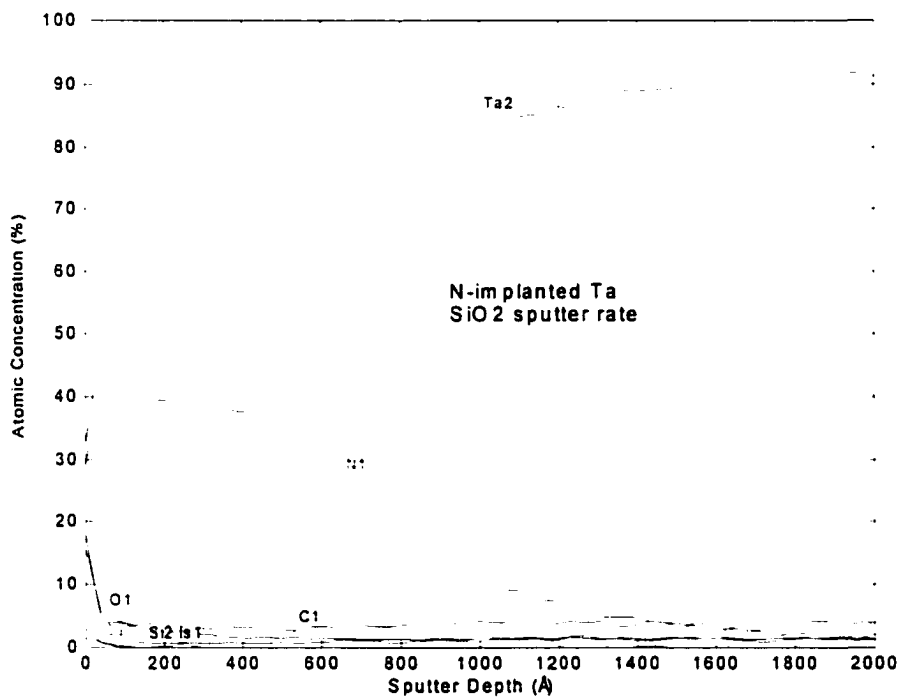
Figure 7.35. AES depth profile of a nitrogen implanted Ta substrate.

Fig. 7.37. The nitrogen concentration decreases monotonically from 17% at the surface

to about 3% at 200Å depth. Compared to the Nb implanted at the same conditions, the

nitrogen concentration is low and the range is confined to the topmost layer. A possible

reason for the very low nitrogen concentration is the existence of thin but dense carbide

and oxide layer on the Mo surface. The carbon concentration is more than 20% for the top

50 Å range and the oxygen concentration is over 20% from 10Å to 110Å range. Compared

to Mo, the surface oxygen and carbon concentration are lower for Nb substrate, which has

a much higher and wider distribution of nitrogen (see below).

AES spectrum of the implanted Nb surface is shown in Fig. 7.38. The elements

shown are nitrogen, carbon, oxygen, and niobium. The concentration obtained by AES

depth profile is shown in Fig. 7.39. The top 300Å layer shows a nitrogen concentration

of around 50%, which decreases slowly to about 10% at 1400Å. Nitrogen concentration is

lower than 50% at the top surface where the oxygen and carbon concentration are higher.

Throughout the sputtered depth, except for the top 100Å range, there is an almost constant

concentration of oxygen (around 10%), carbon (around 6%) and silicon (around 4%).

The AES spectrum of the implanted SS surface is shown in Fig. 7.40. Elements

detected are oxygen, ion, carbon, nitrogen, silicon, aluminum, calcium, and sulfur. AES

depth profile (Fig. 7.41) shows that the nitrogen concentration peaks at about 200Å, with a

peak value of 19%. The nitrogen concentration stays above the 10% level until 1800 Å, then

slowly decreases to below 3% around 3000 Å. The condition through the top 0-600Å range

is more complicated. The Ni peak concentration (22%) is found at 400Å depth while Cr

peaks (27%) at 200 Å. For depths larger than 600Å, the Ni concentration fluctuates around
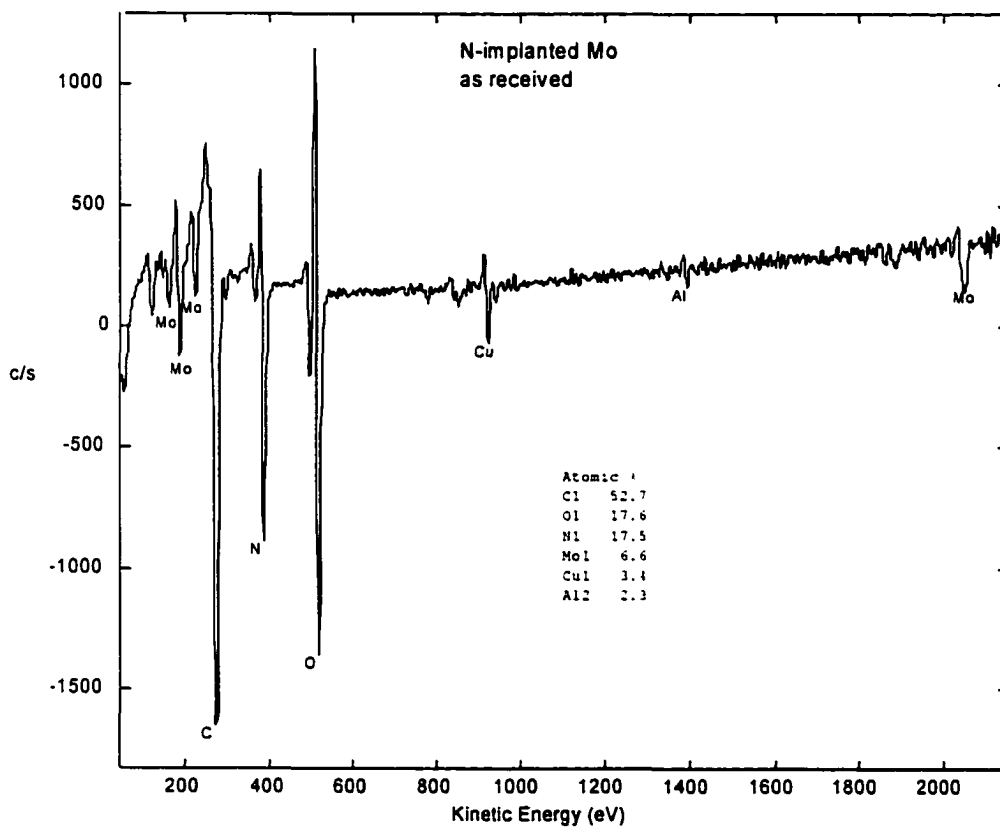
Figure 7.36. AES spectrum of a nitrogen implanted Mo substrate surface.
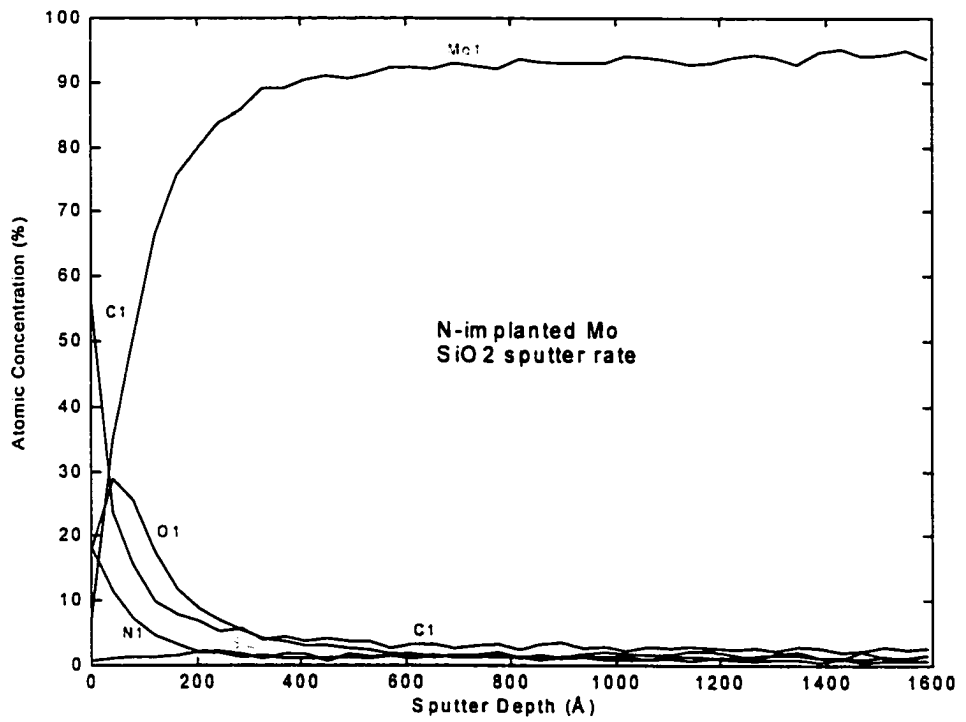
Figure 7.37. AES depth profile of a nitrogen implanted Mo substrate.
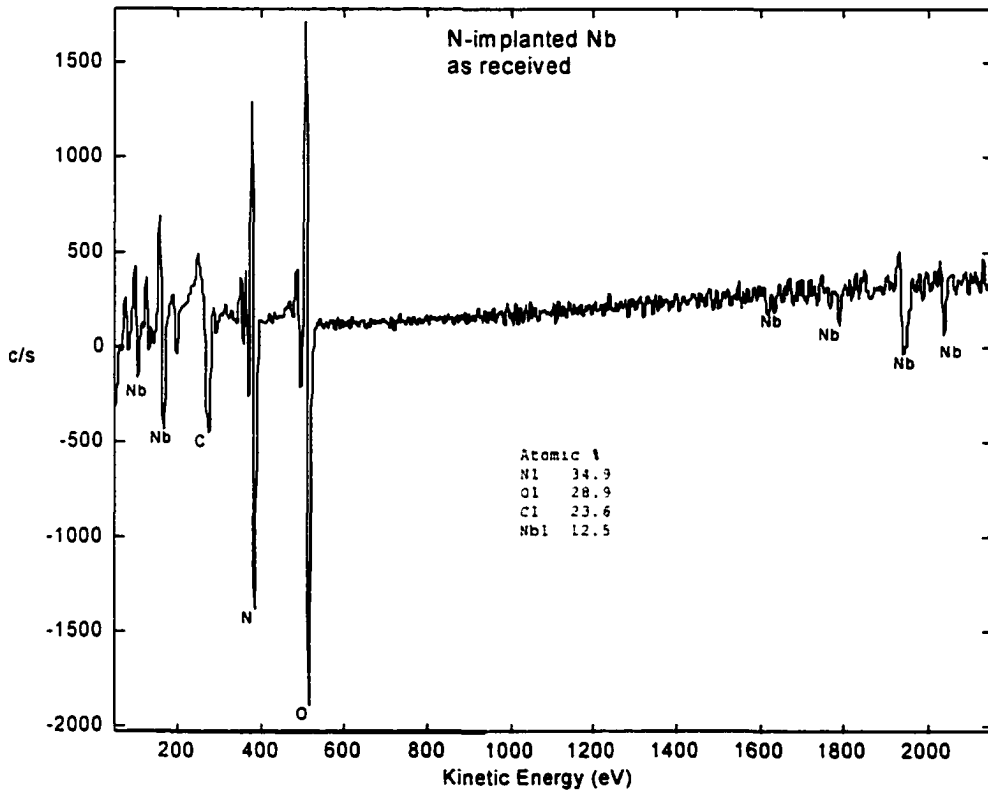
Figure 7.38. AES spectrum of a nitrogen implanted Nb substrate surface.
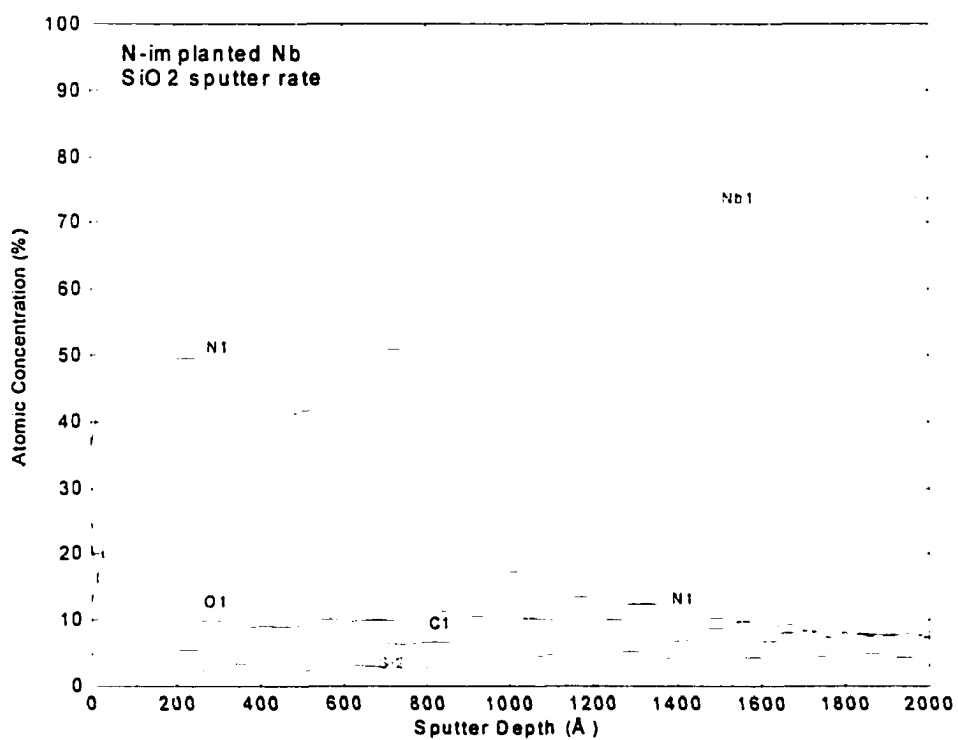
Figure 7.39. AES depth profile of a nitrogen implanted Nb substrate.

8% and the Cr increases slowly to around 20% level. Oxygen concentration decreases from 42% at the top to about 2% at 500Å depth. Higher silicon concentration is also found in the top 100Å range, which may have been introduced from polishing and processing. The nitrogen peak around 200 Å is probably due to the combined effects of implantation parameters, peaked Ni, and Cr concentrations for the 0-700 Å range, and the high surface oxide concentration.

Compared to the nitrogen implanted Ta and Nb, which were implanted with the same experimental parameters, and having maximum nitrogen concentration of 42% and 50% respectively, the nitrogen concentration of the stainless steel is much lower (<20%). However, the penetrated depth is deeper than that of Ta and Nb, which decreases to below 10% at 1000 Å and at 1500 Å respectively. Except for the top 300 Å layer, the nitrogen concentration curve is much flatter, staying around the 10% level for a range of about 2000 Å. To obtain higher dose for stainless steel, a longer implantation time must be used.

Among the implanted samples, the largest hardness increase was found on the nitrogen implanted Ti substrates (Fig. 7.25), which was also the one having the highest nitrogen concentration and the largest implanted layer thickness, according to AES depth profiling. Under the same implantation conditions as used for Ti substrates, Mo and SS samples have lower retained doses, which caused insignificant hardness increases compared to bare substrates. The implanted layer shape is similar for nitrogen implanted Ta and Nb samples, with Nb having slightly higher N concentration (Fig. 7.35 and Fig. 7.39). However, both showed very little hardness increase compared to bare substrates.
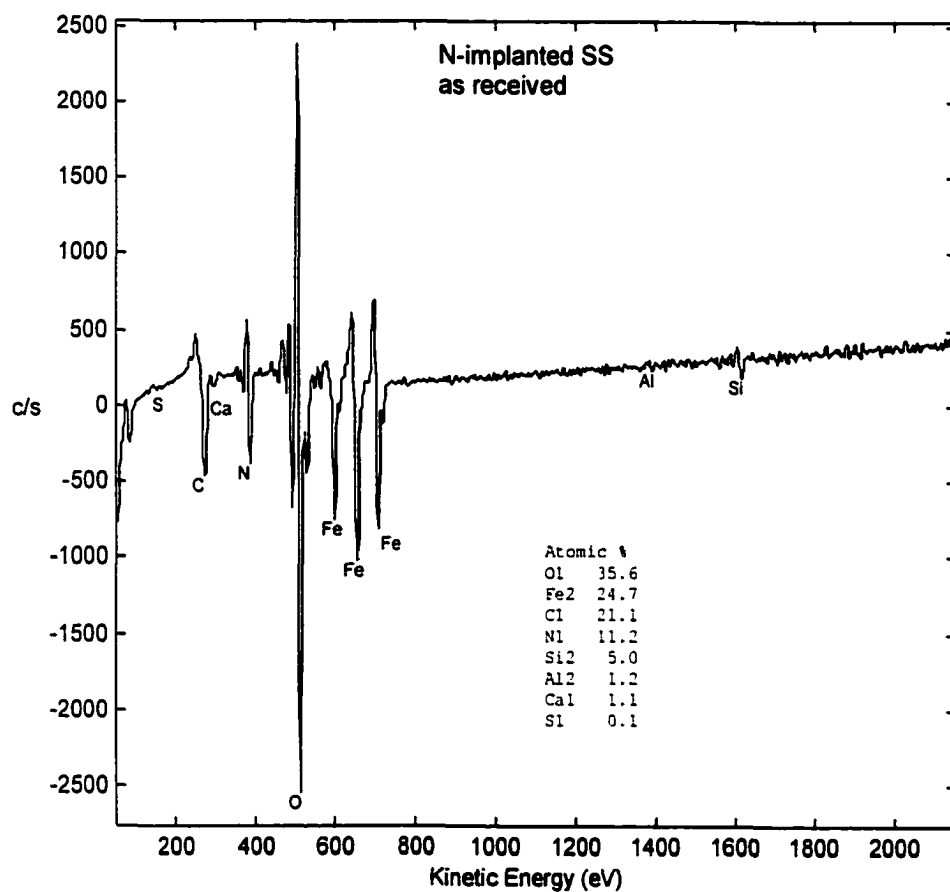
Figure 7.40. AES spectrum of a nitrogen implanted stainless steel substrate surface.
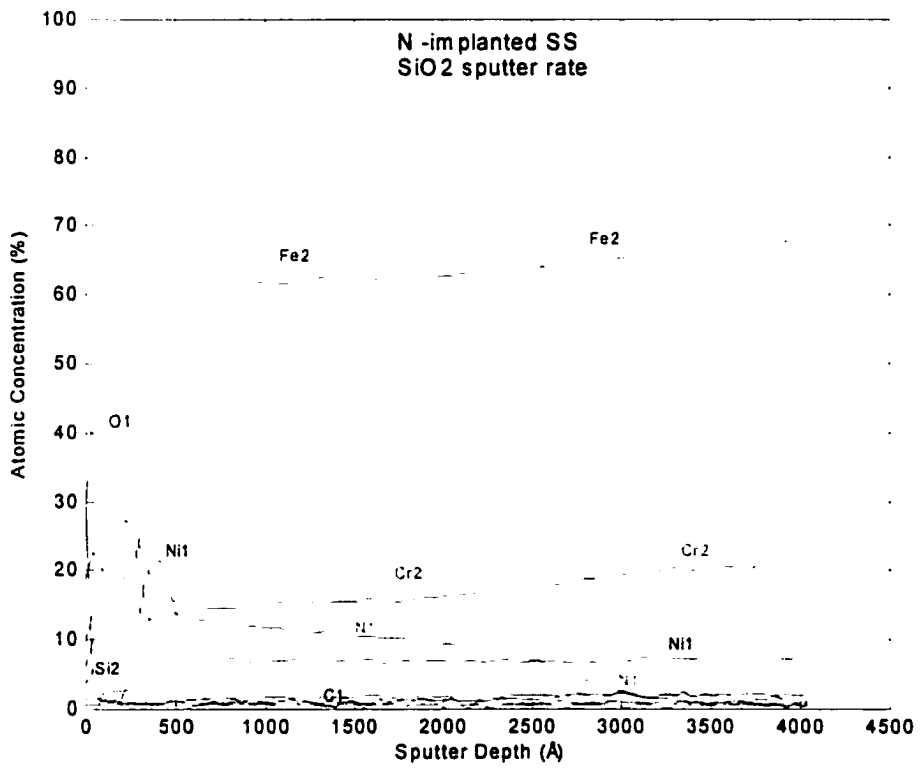
Figure 7.41. AES depth profile of a nitrogen implanted stainless steel substrate.

AES study of the implanted Ti substrates confirmed that the RFI was operating in the inductive mode, since there are no signs of SiO_2 film deposition on the Ti substrates. The very low concentration ($< 3\%$) of Si throughout the sputtered depth was believed to be residual impurity in the Ti substrate, which was found at the same level and with similar distribution in the AES depth profile for un-processed Ti substrate (Fig. 6.4).

It was concluded that the retained implantation dose varied depending on the type of substrate material, its micro-structure, and the existence of surface carbide and oxide layers under the same implantation conditions. Surface cleaning may be necessary to remove surface layers for certain applications, so that desirable implantation depth profile can be obtained with better prediction and control.

Nitrogen Implanted FEL Stainless Steel Electrode

Traditional plasma nitriding of stainless steel is usually done at elevated temperature to facilitate nitrogen diffusion, to increase nitride layer thickness, and to decrease treating time [118, 125]. Stainless steels have excellent corrosion resistance due to the native passivation layer, resulting from chromium enhancement at the surface, but they do not have high surface hardness. High dose nitridation is said to be effective in enhancing the SS surface hardness. However, higher temperature causes the formation of CrN and a drop of corrosion resistance of the stainless steel surface.

PSII is advantageous in perform nitriding of the stainless steel surface because it can be operated below the critical temperature of 673K for CrN formation [118]. Low temperature is also important for keeping the original target dimension and shape, and

retaining desirable bulk material microstructure. In addition to being a low-temperature process, PSII is capable of 3-D uniform dosing, which is important for the surface treatment of FEL stainless steel electrode for suppressing field emission.

Nitrogen implantation of large FEL electrodes may be useful in suppressing field emission and in enhancing the performance of FEL electron injection gun. Preliminary study showed PSII treatment on small cm scale polished stainless steel test samples reduced field emission [2]. However, the results were obtained at narrow gaps and low voltages, so more research, especially tests of large area implanted electrodes, is needed to study the effectiveness of nitrogen PSII. In addition, our previous PSII system used hot filament or DC glow plasmas, which produced low ion plasma densities, large-spatial non-uniformities, and were possible sources of contamination. These features are unsuitable for large-area 3-D FEL electrode implantation. RFI PSII makes high voltage breakdown tests of full-size 3-D electrodes possible. Highly polished 3-D electrodes have a surface finish of from 1 μm to 9 μm. For polished large area FEL electrodes without nitrogen implantation, turn-on voltages can vary by factors of 2 or more for similarly prepared electrodes. Anomalous field emission from the electrodes is unpredictable in nature. PSII nitriding can help to increase surface hardness, and to remove (condition) surface protrusions, which are the sites of strong field emission. Higher surface hardness values may not be the reason for reduced field emission.

A 1/3-scale FEL test electrode was successfully nitrogen implanted during these studies using the large-scale CWM RFI PSII. As shown in Fig. 7.42, the test electrode has special 3-D structure and is highly polished. The implanted area shows very uniform color,

without any signs of arcing or other kind of damage, indicating very uniform ion implantation.

The PSII system also offers other exciting possibilities for alternative 3-D treatments of FEL electrodes. High quality SiO_2 films have been deposited on 0.15 m ID electrode with Rogowski surface profile, with constant nitrogen concentration depth profile in the films. This is discussed at length in Chapter 6. The PSII system makes it possible to control the spatial distribution of nitrogen in the deposited films. Nitrogen sputtering of the electrode surface can also be performed for surface oxide/carbide cleaning. Nitrogen implantation at the surface can be performed prior to film deposition for interface adhesion promotion. The large-scale RFI source can also be used to excite large uniform plasmas of other gas species to perform chemical vapor deposition on large FEL electrodes. With uniformly elevated target surface temperature of around $400°C$, high quality DLC films can also be deposited on FEL electrodes (see Chapter 2 on DLC deposition for applicability to turbine engine applications). These prospects will be discussed in Chapter 8.

7.4 Summary

Nitrogen ion implantation has been successfully performed using the CWM large-scale RFI PSII onto a variety of substrates, including Ti, Ta, Mo, Nb and stainless steel sheets, and three dimensional highly polished stainless steel FEL test electrode. To help to understand surface analysis results, target temperature rise due to implantation pulses was calculated for different implantation repetition rate, target surface conditions, and stage setup. Implan-
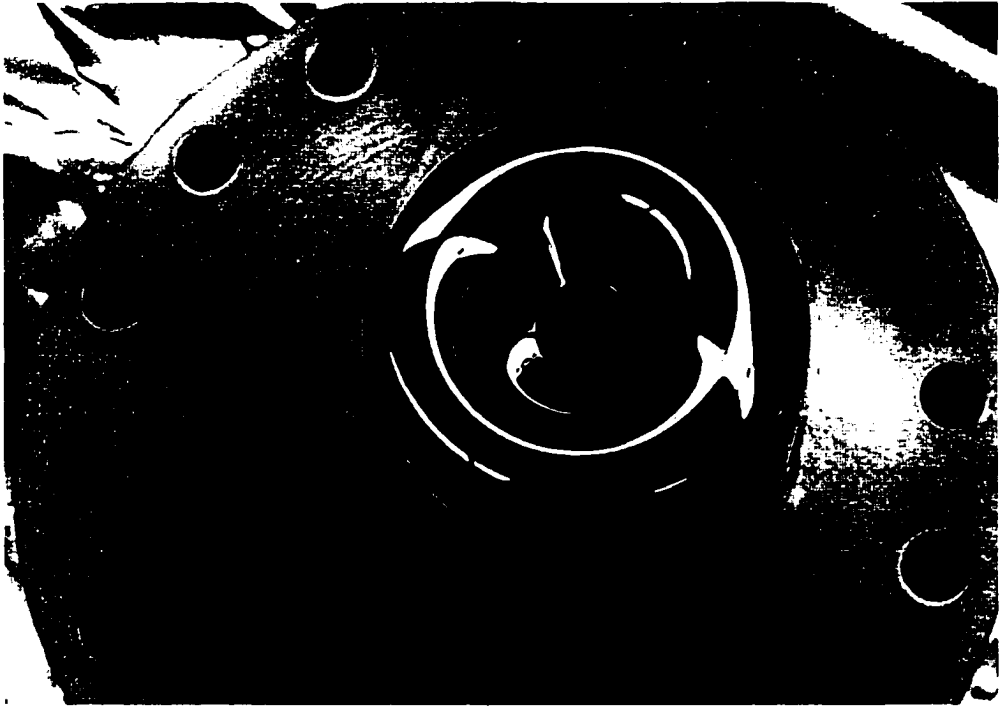
Figure 7.42. Nitrogen implanted FEL test electrode sitting on a support flange. It is 2.5 in. ID. The highly polished stainless steel surface shows uniform color. Its surface is also free of arcing or any other kind of damage.

tation depth profiles for different materials were calculated by Profile Code. The surface morphology of the implanted and un-implanted metal sheets were studied by optical microscopy for comparison. These studies showed that nitrogen PSII can help to smooth the Ti and Mo substrate surface. Surface hardness of implanted samples were studied using different load values and compared to that of bare substrates. Nitrogen implanted Ti substrate showed the largest hardness increases. Hardness increases were lower for other metal surfaces. AES was used for implanted substrate elemental composition study and surface depth profiling. AES depth profiling of the implanted and un-processed Ti substrates confirmed that there is no SiO_2 contamination from the PSII system. The nitrogen implanted Ti substrate has the highest retained dose and highest maximum nitrogen concentration, which also has the highest hardness increase compared to the bare substrate. Surface oxide and carbide layers caused low nitrogen concentration and shallow implantation layer for Mo substrate. Under the same implantation parameters, the nitrogen concentration for the implanted layer varied because of the substrate structure, atomic number, and existence of surface oxide and carbide layers.

Nitrogen ion implantation of 3-D FEL test electrode was also successfully performed. The implanted electrode shows very uniform color, without any signs of arcing or other damage. The ability to perform large-area, 3-D implantation makes it possible to test the surface treatment effects on large-area, real size FEL electrodes. Correlated with surface analysis results, this information can help the search for the best surface treatment recipe to suppress field emission, and lead to an understanding of the mechanism of field emission from these highly polished high voltage electrodes.

Chapter 8

Conclusions and Future Work

8.1   Conclusions

A planar RFI PECVD system was designed and built for large-area, uniform DLC films deposition. Ti-6Al-4V substrates have been coated with DLC films without surface pretreatment and with Ti/MoS$_2$ films with only a simple surface pre-cleaning. Both kinds of films exhibited much better tribological properties than the plasma sprayed Cu-Ni-In coating that is currently used to protect Ti-6Al-4V substrate against fretting and wear in turbine engine applications. Optical investigation was found to be valuable for tribological coating characterizations. Variable angle spectroscopic ellipsometry was used to measure optical properties and thickness of the PECVD DLC films. The optical properties of DLC film helped to quickly evaluate the film quality and to indicate whether further destructive and time-consuming tests were warranted. These measurements were also correlated with interference color and visible appearance of the films to provide a fast assessment of thickness and smoothness.

219

A large-scale planar RFI plasma source was successfully designed and built, to fully realize the large-area uniform plasma generating capability of RFI source and the potential of PSII for large scale, 3-D, uniform surface processing. The design and materials problem in the scale-up process have been successfully solved. The generated plasma was characterized by Langmuir probe and OES in detail. The large-scale RFI source is very stable, producing plasma density higher than that of the previous hot filament plasma or DC glow discharge, with greatly improved spatial uniformity. The successful operation of large-scale RFI makes 3-D, large size, uniform, contamination-free plasma source immersion ion implantation possible.

The AFOSR MAGIC code was also for the first time used to model plasma source ion implantation process. Taking advantage of the many successfully integrated PIC techniques of MAGIC Code, the PSII modeling presented in this dissertation addressed different target geometries and boundaries, materials, plasma parameters, illustrated sheath formation and evolution, field distribution, ion and electron trajectories, ion incident angles, and dose distributions, which are critical information for PSII experiment design and understanding of PSII process. MAGIC modeling of PSII is advantageous compared to 1-D or pseudo 2-D analytical models, for its 3-D and multiple information output capability. It is also more efficient and convenient to perform than working on low level PIC code development or modification of legacy codes of plasma physics modeling.

Large-scale PSII pattern writing has been successfully performed using the large-scale PSII as a mask-based surface layer property conversion technique, as an alternative to current deposition-based and ink-based direct write technologies. High dose implantation

was found to produce thin-film-like structure in the substrate surface, which enables the optical characterization of implantation dose distribution. Compared to AES or SIMS depth profiling, which require high vacuum environment and are limited to small area analysis, ellipsometry is fast, convenient, and non-destructive, which is highly desirable for large 3-D dose distribution studies. It is also suitable for 3-D dose characterization whenever cutting the target into small AES or SIMS samples is not an option. Small 2 μm features were also implanted and capped with nitrogen doped SiO_2 layer. TEM study shows that PSII direct write can be performed to faithfully write μm feature sizes. Smaller features may be possible if mask and experimental conditions are carefully designed. To our knowledge, this is the first comprehensive study along these lines.

The PSII system can also be operated in a novel PSII/PVD mode, which produces large-area, high quality nitrogen-doped SiO_2 films on a variety of substrates with good adhesion. SiO_2 films are important optical coating and insulating layer. It is also a hard protecting and passivating material. Hydrogen-free and low temperature deposited SiO_2 are strongly recommended for inter-insulating layers in ULSIs and for gate insulators in thin-film transistors [23]. Oxynitride multilayers have been found to enhance the ULSI device performance and reliability [22]. Doping of the SiO_2 layers with other elements can produce different layer dielectric constants. The PSII/PVD process offers the ability of coating sensitive or low-melting point substrates at low temperatures. So far, we have used nitrogen gas for doping, which is safe to handle, easy to pump, and benign to the vacuum system. This also eliminated the source of hydrogen incorporation into the deposited film. With the PSII capability of PSII/PVD, in situ surface cleaning and interface modifica-

tion, spatial control of nitrogen incorporation, pre- and post-deposition implantation are all easy to realize. The deposited films were studied by AES depth profiling to study the distribution of nitrogen in the film and the interface. Ellipsometry was also used to find that the deposited SiO_2 layers have excellent optical quality that is very close to that of fused quartz.

High dose nitrogen ion implantation was performed on a group of transition metals that are possible candidates for anti-diffusion layers for microelectronics applications. Ti and stainless steel were given special attention because they are used to make test electrode for FEL electron injection gun. Implantation depth profiles were studied in detail and correlated with Profile Code calculations and target temperature estimation. Surface morphology study using optical microscope showed that the highly polished stainless steel substrate surface did not show any deterioration of surface finish, the surface of Ti and Mo were "conditioned" and made smoother. It was found that surface oxide/carbide layer, and the substrate material and structure play an important role in determining implantation depth profile. AES study of implanted and un-processed Ti substrates also confirmed that the RFI was operated in a pure inductive mode at the implantation pressure used. There was no sputtered material from the dielectric window detected by OES or collected on the Ti substrates processed for several hours by PSII.

Successful implantation of an FEL test electrode was also performed, yielding a uniform coating, as indicated by surface color, without any sign of arcing or other kind of surface imperfection, which are believed to be the sites of strong field emission.

The successful operation of the large-scale RFI PSII and the surface analysis results of implanted samples are important for the effort of suppressing field emission from the electrodes for FEL electron injection gun. Previous study indicated that nitrogen ion implantation of 1 cm ID test samples reduced field emission [2]. However, it is important to have the capability of processing large FEL electrode, so that HV breakdown test can be performed on full-scale electrodes to investigate the effect of nitrogen ion implantation on field emission. The non-linear relationship between breakdown field and gap voltage, the Total Voltage Effect, requires such extreme testing [2]. HV breakdown test in large-scale would provide confidence in successful operation under higher voltage for FEL electron injection gun.

The PSII/PVD system also provides other possibilities of processing electrode surface, such as coating the electrode surface with nitrogen-doped SiO_2. A large-scale electrode processed by this method has already been tested at TJNAF HV breakdown test facility, showing reduced field emission. The test results showed that the processed electrode could be operated with a field gradient of 24 MV/m, with a dark current of merely 160 pA; compared to the applied field gradient of 3−6 MV/m and dark current of a fraction of micro amps for the unprocessed electrode. The conditioning time for the processed electrode was also much shorter. Another possibility is to operate the PSII facility as a PSII/CVD system, with PSII pulse heating and possibly another supplementary heating source, depositing DLC films on electrode surface with or without implanting the DLC with nitrogen, to produce DLC, nitrogen-doped DLC, or carbon nitride films on electrode surface. DLC has

many superior properties compared to SiO_2. DLC and carbon nitride films are promising candidates for field emission suppressing because of their extreme hardness.

8.2   Future Work

The CWM RFI PECVD was quite successful in producing high quality DLC films on semiconductor and metal substrates. DLC films deposited at a substrate temperature of $400°C$ were found to have mechanical and optical properties comparable with that of DLC deposited around 800°C. DLC deposition at even lower temperature is highly desirable when sensitive substrates need to be coated. Preliminary study also found that the DLC films deposited have very smooth surfaces and excellent optical properties. Best of all, AFM study found that the DLC on un-scratched mirror polished Si and as-received Ti-6Al-4V were highly oriented. The crystalline size is of nanometer range. Oriented DLC is highly sought after for its better micro-electronic and optical properties. Recently, the research group at Argonne National Lab also found nanocrystal diamond film ideal for MEMS device manufacturing [126]. Further study is desirable to optimize the deposition conditions and to understand the physical and chemical mechanism of oriented DLC CVD. The PECVD system is also ready for carbon nitride films deposition with its heated stage and gas feed system.

The successful operation of PSII/PVD/CVD system makes several things possible:

First, a vigorous search for best recipe to use on FEL electrode surface treatment to suppress field emission. As mentioned above, nitrogen ion implantation of FEL test

electrode was successful to produce uniform and arc-free surface nitridation. With the collaboration of TJNAF scientists, a full-scale implanted electrode can be tested, and data be correlated with surface analysis results and implantation parameters, so that the best implantation recipe can be obtained.

Second, doped SiO_2 films deposition on FEL electrodes. HV breakdown test at TJ-NAF showed that the nitrogen-doped SiO_2 film on a 6 in. FEL electrode has helped to greatly suppress field emission. Further study should be carried out to optimize the deposition parameters to enhance this electrode performance. Extending the life, reducing the conditioning time, and increasing the maximum field will all add great value to the \$25M Laser facility. It will also be an enabling technology for small particle accelerators and other high-voltage applications.

Third, spatial control of implanted species concentration in the films deposited by PVD or CVD, to produce novel multilayer structures for surface modification.

Fourth, DLC films deposition in the PSII system, by feeding methane and hydrogen gas mixture to the chamber and possibly adding active sample stage heating. PSII can also be used to perform pre- or post-deposition nitrogen ion implantation, heat the substrate, optimize film/substrate interface properties, and to modify the deposited DLC film. With its superior properties compared to SiO_2, DLC could be another promising candidate for FEL electrode surface treatment to reduce field emission.

Fifth, SiO_2 films can also be deposited on a larger variety of substrates. In addition to Si, Ti, stainless steel substrates, doped SiO_2 films have also been deposited onto copper, silver, tungsten, carbon tape and glass substrates with good adhesion. Possible applications

include optical coatings, insulating layers, and hard protective coatings, which all require

further investigation of deposition conditions, film properties, and interface properties.

Sixth, to enable a remotely actionable, automatic switch from pure PSII mode to

PSII/PVD mode for multi-step, multi-layer surface treatment, an (electro-) mechanical

Faraday shield positioning system needs to be designed and built, to control the RF plasma

source to be operated in an inductive mode, or capacitive/inductive mix mode. This patentable

set of innovations will be of great field utility.

Seventh, PSII can be used to perform low-temperature surface modification of poly-

mers, rubbers, and other low melting point materials. Preliminary results in our laboratory

showed that nitrogen ion implantation can "write" three dimensional features in glass and in

transparent polymer sheets. These kinds of features can be used for optical signal process-

ing. The addition of a cooling stage can further decrease the substrate temperature, protect

the sensitive substrate, and control lateral diffusion of written features.

Eighth, preliminary tests of the use of PSII for "direct-write" device developments

have been performed and reported in this dissertation. Such use may be of importance in the

production of sensors, electronic devices, and MEMS structures. This option has been in

preparation for the use of the JLAB FEL as a major "direct-write" tool in the areas outlined

above. Drilling, cutting, photolithography, RTP, and other applications, which have been

sufficiently elaborated in prior FEL-IAB meetings, may benefit greatly from pre-laser or

post-laser PSII treatments. One aspect, for example, is in the control of "stiction" for mov-

ing members in microscopic gear and cantilever applications. Numerous other examples

exist and are well known to JLAB personnel involved in the use of the FEL. Specifically,

continuing investigations are highly recommended for study the means of using PSII to process non-metals, to create compound layers with specific mechanical, optical, and electrical properties suitable for MEMS, sensors, and electrical devices, and to pursue detailed particle-in-cell (MAGIC) modeling of the effects and capabilities of PSII on microscopic scales.

References

[1] J. P. A. M. Driessen. *Low-Temperature Chemical Vapor Deposition of Titanium Nitride*. PhD thesis, Technische Universiteit Delft, 1999.

[2] T. J. Venhaus. *Plasma Source Ion Implantation of High Voltage Electrodes*. PhD thesis, College of William and Mary, 1999.

[3] M. L. Green, D. Brasen, K. W. Evans-Lutterodt, L. C. Feldman, K. Krisch, W. Lennard, H. T. Tang, L. Manchanda, and M. T. Tang. *Applied Physics Letters*, 65(7):848–850, 1994.

[4] Ronald E. Loehman. *Characterization of Ceramics*. Manning Publications Co., 3 Lewis Street, Greenwich, CT 06830, 1993.

[5] S. C. Sharma, C. A. Dark, R. C. Hyer, M. Green, T. D. Black, A. R. Chourasia, D. R. Chopra, and K. K. Mishra. *Appl. Phys. Lett.*, 56(18):1781–1783, 1990.

[6] S. H. Kim, Y. S. Park, J-W. Lee, H. J. Park, H. K. Jang, I. S. Yang, and W. S. Yun. *Materials Science and Engineering*, A209:68–73, 1996.

[7] Kazuhiro Suzuki, Atsuhito Sawabe, Hiroaki Yasuda, and Tadao Inuzuka. *Appl. Phys. Lett.*, 50(12):728–729, 1997.

[8] S. Belkouch, D. Landheer, R. Taylor, K. Rajesh, and G. I. Sproule. *Materials Research Society Proceedings, Amorphous and Crystalline Insulating Thin Films-1996*, pages 151–156, 1997.

[9] Steven K. Brierley and Lan Nguyen. *Materials Research Society Proceedings, Amorphous and Crystalline Insulating Thin Films-1996.*, pages 145–150, 1997.

228

[10] J. R. Conrad, J. L. Radtke, R. A. Dodd, Frank J. Worzala, and Ngoc C. Tran. *Journal of Applied Physics*, 62(11):4591–4596, 1987.

[11] S. M. Malik, K. Sridharan, R. P. Fetherston, A. Chen, and J. R. Conrad. *J. Vac. Sci. Technol. B*, 12(2):843–849, 1994.

[12] Michael A. Lieberman and Allan J. Lichtenberg. *Principles of Plasma Discharges and Materials Processing*. John Wiley and Sons, Inc., 1994.

[13] J. N. Matossian. *J. Vac. Sci. Technol. B*, 12(2):850, 1994.

[14] M. Tuszewski, J. T. Scheuer, I. H. Campbell, and B. K. Laurich. *J. Vac. Sci. Technol.*, 12(2):973–976, 1994.

[15] B. P. Wood, I. Henins, R. J. Gribble, W. A. Reass, R. J. Faehl, M. A. Nastasi, and D. J. Rej. *J. Vac. Sci. Technol. B*, 12(2):870, 1994.

[16] S. Qin and C. Chan. *J. Vac. Sci. Technol. B*, 12(2):962, 1994.

[17] J. Hopwood. *Plasma Source Science and Technology*, 1:109–116, 1992.

[18] S. P. Bozeman, D. A. Tucker, B. R. Stoner, J. T. Glass, and W. M. Hooke. *Appl. Phys. Lett.*, 66(26):3579–3581, 1995.

[19] T. Munsat, W. M. Hooke, S. P. Bozeman, and S. Washburn. *Appl. Phys. Lett.*, 66(17):2180–2182, 1995.

[20] D. L. Pappas and J. Hopwood. *J. Vac. Sci. Technol. A*, 12(4):1576–1582, 1994.

[21] William L. Warren. *Materials Research Society Symposium Proceedings - Materials Development for Direct Write Technologies*, 624, 2000.

[22] G. Lucovsky. *Materials Research Society Symposium Proceedings, Amorphous and Crystalline Insulating Thin Films-1996*, 446:67–78, 1997.

[23] Y. Uchida, S. Takei, and M. Matsumura. *Materials Research Society Symposium Proceedings*, 446:21–26, 1997.

[24] B. W. Buchholtz and F. M. Kustas. *Tribology Transactions*, 39(2):330–337, 1996.

[25] Fretting and wear resistance coatings for turbine engine applications. Technical Report Report No. ASM-R74-98-01, Analytical Services and Materials, Inc., 1998.

[26] F. P. Bowden and D. Tabor. *Friction and Lubrication.* Methuen and CO. LTD, 11 New Fetter Lane, London EC4, 1967.

[27] T. Spalvins. Lubrication with sputtered MoS2 films: Principles, operation, limitations. Technical Report NASA Technical Memorandum 105292, Lewis Research Center, 1991.

[28] George L Trigg. *Encyclopedia of Applied Physics.* VCH Publishers, Inc., 220 East 23rd Street, Suite 909, New York, NY 10010, 1993.

[29] David R. Lide. *CRC Handbook of Chemistry and Physics.* CRC Press, Inc., 2000 Corporate Blvd., N. W., Boca Raton, Florida, 33431, 1992-1993.

[30] R. F. Davis. *Diamond Films and Coatings.* Noyes Publications, 1993.

[31] K. Komvopoulos, N. Saka, and N. P. Suh. *Journal of Tribology*, 109:223–231, 1987.

[32] E. Cappelli, F. Pinzari, P. Ascarelli, and G. Righini. *Diamond and Related Materials*, 5:292–298, 1996.

[33] S. Christiansen, M. Albrecht, H. P. Strunk, H. Hornberger, P. M. Marquis, and J. Franks. *J. Mater. Res.*, 11(8):1934–1942, 1996.

[34] C. V. Deshpandey and R. F. Bunshah. *J. Vac. Sci. Technol.*, A7(3):2294–2302, 1989.

[35] M. L. Hartsell and L. S. Plano. *J. Mater. Res.*, 9(4):921–926, 1994.

[36] W. Zhu, P.C. Yang, J. T. Glass, and F. Arezzo. *J. Mater.Res.*, 10(6):1455–1460, 1995.

[37] W. Zhu, F. R. Silvazlian, B. R. Stoner, and J. T. Glass. *J. Mater. Res.*, 10(2):425–430, 1995.

[38] E. I. Meletis, A. Erdemir, and G. R. Fenske. *Surface and Coatings Technology*, 73:39–45, 1995.

[39] Y. Liu, A. Erdemir, and E. I. Meletis. *Surface and Coatings Technology*, 82:48 – 56, 1996.

[40] F. M. Kustas, M. S. Misra, R. Wei, and P. J. Wilbur. *Tribology Transactions*, 36(1):113–119, 1993.

[41] Soon-Cheon Seo, David C. Ingram, and Hugh H. Richardson. *J. Vac. Sci. Technol. A*, 13(6):2856–2862, 1995.

[42] M. Basu S.N. Kund and, K. K. Chattopadhyay, A. B. Maity, S. Chaudhuri, and A. K. Pal. *Vacuum*, 48(5):435–441, 1997.

[43] F. Davanloo, H. Park, and C. B. Collins. *J. Mater. Res.*, 11(8):2042–2050, 1996.

[44] C. P. Munson, R. J. Faehl, I. Henins, M. Nastasi, W. A. Reass, D. J. Rej, J. T. Scheuer, K. C. Walter, and B. P. Wood. *Surface and Coatings Technology*, 84:528–536, 1996.

[45] F. Alonso, J. J. Ugarte, D. Sansom, J. L. Viviente, and J. I. Onate. *Surface and Coatings Technology*, 83:301 –306, 1996.

[46] E. W. Roberts. *Proceedings of 20th Aerospace Mechanisms Symposium, Lewis Research Center, Cleveland, Ohio*, pages 103–119, 1986.

[47] L. E. Seitzman and I. L. Singer. *Light weight alloys for aerospace applications*, 3:371–378, 1995.

[48] L. E. Seitzman, R. N. Bolster, and I. L. Singer. *Surface and Coatings Technology*, 78(1):10–13, 1996.

[49] Purtech Inc., Progress St., East Stroudsburg, PA 18301, USA (1-570-424-1669).

[50] J. A. Woollam Co. Inc., 650 J St., Suite 39, Lincoln, NE 68508, USA (1-402-477-7501).

[51] *Guide to Using WVASE32*. J. A. Woollam Company, 650 J. St., Suite 39, Lincoln, NE 68508, 1997.

[52] S. Wolf and R.N. Tauber. *Silicon Processing for the VLSI Era, Volume1: Process Technology*. Lattice Press, Sunset Beach, California, 1986.

[53] O. S. Heavens. *Optical Properties of Thin Solid Films*. Dover Publications, 1991.

[54] Quad Group, 1815-TS Lewis, Spokane, WA 99224, USA (1-509-458-4558).

[55] *ASTM G99-95ae1 Standard Test Method for Wear Testing with a Pin-on-Disk Apparatus, Copyright 2000*. American Society for Testing and Materials, West Conshohocken, PA.

[56] *ASTM G77-98 Standard Test Method for Ranking Resistance of Materials to Sliding Wear Using Block-on-Ring Wear Test, Copyright 2000.* American Society for Testing and Materials, West Conshohocken, PA.

[57] V. P. Godbole, K. Jagannadham, and J. Narayan. *Appl. Phys. Lett.*, 67(9):1322–1324, 1995.

[58] B. R. Stoner, G. H. M. Ma, S. D. Wolter, and J. T. Glass. *Physical Review B*, 45(19):11067–84, 1992.

[59] S. D. Wolter, B. R. Stoner, J. T. Glass, P. J. Ellis, D. S. Buhaenko, C. E. Jenkins, and P. Southworth. *Appl. Phys. Lett.*, 62(11):1215–1217, 1993.

[60] F. Arezzo, N. Zacchetti, and W. Zhu. *J. Appl. Phys.*, 75(10):5375–5381, 1994.

[61] J. Mencik, D. Munz, E. Quandt, E. R. Weppelmann, and M. V. Swain. *J. Mater. Res.*, 12(9):2475–2484, 1997.

[62] M. Filonenko-Borodich. *Theory of Elasticity.* Dover Publications, Inc., 180 Varick Street, NY, N. Y. 10014, 1965.

[63] Jung-Hun Kim, Ho-Jun Lee, Youn-Taeg Kim, Ki-Woong Whang, and Jung-Hoon Joo. *J. Vac. Sci. Technol. A*, 15(3):564–567, 1997.

[64] Hideo Sugai, Kenji Nakamura, and Keiji Suzuki. *Jpn. J. Appl. Phys.*, 33(4B):2189–2193, 1994.

[65] Yukinobu Hikosaka, Moritaka Nakamura, and Hideo Sugai. *Jpn. J. Appl. Phys.*, 33(4B):2157–2163, 1994.

[66] D. F. Beale, A. E. Wendt, and L. J. Mahoney. *J. Vac. Sci. Technol. A*, 12(5):2775–2779, 1994.

[67] J. Hopwood. *Plasms Source Science and Technology*, 3:460–464, 1994.

[68] Ho-Jun Lee, Il-Dong Yang, and Ki-Woong Whang. *Plasma Source Science and Technology*, 5:383–388, 1996.

[69] Xianmin Tang and Dennis M. Manos. *Plasma Sources Science and Technology*, 8:594–602, 1999.

[70] Xianmin Tang. *Low Damage Processing and Process Characterization.* PhD thesis, College of William and Mary, 2000.

[71] J. Hopwood, C. R. Guarnieri, S. J. Whitehair, and J. J. Cuomo. *J. Vac. Sci. Technol. A*, 11(1):152–156, 1993.

[72] Sune Svanberg. *Atomic and Molecular Spectroscopy.* Springer-Verlag, Berlin, 1992.

[73] Peter F. Bernath. *Spectra of Atoms and Molecules.* Oxford University Press, New York, 1995.

[74] F. Debal, M. Wautelet, J. Bretagne, J. P. Dauchot, and M. Hecq. *Plasma Source Science and Technology*, 9:152–160, 2000.

[75] Tomoaki Hino, Ichiro Fujita, and Masana Nishikawa. *Plasma Source Science and Technology*, 5:424–428, 1996.

[76] V. Scherentz and G. Henrion. *Plasma Source Science and Technology*, 9:32–36, 2000.

[77] R. W. B. Pearse and A. G. Gaydon. *The Identification of Molecular Spectra.* Chapman and Hall Ltd, 733 Third Avenue, NY, NY 10017, 4th edition, 1984.

[78] A. V. Blant, O. H. Hughes, T. S. Cheng, S. V. Novikov, and C. T. Foxon. *Plasma Source Science and Technology*, 9:12–17, 2000.

[79] T. E. Sheridan and A. J. Alport. Ion-matrix sheath around a square bar. *J. Vac. Sci. Technol. B*, 12(2):897–900, 1994.

[80] R. Faehl, B. De Volder, and B. Wood. Application of particle-in-cell simulation to plasma source ion implantation. *J. Vac. Sci. Technol. B*, 12(2):884–888, 1994.

[81] S. Mandl, J. Brutscher, R. Gunzel, and W. Moller. *J. Vac. Sci. Technol. B*, 14(4):2701–2706, 1996.

[82] S. M. Malik, D. E. Muller, K. Sridharan, R. P. Fetherston, Ngoc Tran, and J. R. Conrad. *Journal of Applied Physics*, 77(3):1015–1019, 1995.

[83] M. Shamim, J. T. Scheuer, and J. R. Conrad. *Journal of Applied Physics*, 69(5):2904–2908, 1991.

[84]   J. T. Scheuer, M. Shamim, and J. R. Conrad. *Journal of Applied Physics*, 87(3):1241–1245, 1990.

[85]   Shu Qin, Yuanshong Zhou, and Chung Chan. *IEEE Transaction on Plasma Science*, 27(3):766–771, 1999.

[86]   Zhaoming Zeng, Xiubo Tian, Baoyin Tang Dixon Tai-Kun Kwok, and Paul K. Chu. *IEEE Transaction on Plasma Science*, 27(4):1203–1209, 1999.

[87]   Dezhen Wang, Tengcai Ma, and Xinlu Deng. *J. Vac. Sci. Technol. B*, 12(2):905–909, 1994.

[88]   M. Paulus, L. Stals, U. Rude, and B. Rauschenbach. *Journal of Applied Physics*, 85(2):761–766, 1999.

[89]   Jorg Brutscher, Reinhard Gunzel, and Wolfhard Moller. *Plasma Source Science and Technology*, 5:54–60, 1996.

[90]   J. P. Verboncoeur, A. B. Langdon, and N. T. Gladd. *Computer physics Communications*, 87:199–211, 1995.

[91]   Bruce Goplen, Larry Ludeking, and David Smithe. *Magic User's Manual*. Mission Research Corporation, 1997.

[92]   Bruce Goplen, Larry Ludeking, David Smithe, and Gary Warren. *Computer Physics Communications*, 87:54–86, 1995.

[93]   Kenneth H. Church. *Materials Research Society Symposim Proceedings - Materials Development for Direct Write Technologies*, 624, 2000.

[94]   Herbert Herman, Sanjay Sampath, Richard Gambino, Ashish Patel, and Andrew Dent. *Materials Research Society Symposium Proceedings - Materials Development for Direct Write Technology*, 624, 2000.

[95]   S. Y. Tan, R. J. Gambino, R. Goswami, S. Sampath, and H. Herman. *Materials Research Society Symposium Proceedings - Materials Development for Direct Write Technologies*, 624, 2000.

[96]   Melissa Orme, Qingbin Liu, Jun Zhu, and Robert Smith. *Materials Research Society Symposium Proceedings - Materials Development for Direct Write Technologies*, 624, 2000.

[97] Duane Dimos, Paul G. Glem, Nelson S. Bell, Terry J. Garino, Pin Yang, and Mark A. Rodriguez. *Materials Research Society Symposium Proceedings - Materials Development for Direct Write Technologies*, 624, 2000.

[98] David Longo and Robert Hill. *Materials Research Society Symposium Proceedings - Materials Development for Direct Write Technologies*, 624, 2000.

[99] D. B. Chrisey, A. Pique, J. M. Fitz-Gerald, R. C. Y. Auyeung, H. D. Wu, S. Lakeou, and R. Chung. *Materials Research Society Symposium Proceedings - Materials Development for Direct Write Technologies*, 624, 2000.

[100] N. Reis and B. Derby. *Materials Research Society Symposium Proceedings - Materials Development for Direct Write Technologies*, 624, 2000.

[101] A. Chen, J. Firmiss, and J. R. Conrad. *J. Vac. Sci. Technol. B*, 12(2):918, 1994.

[102] *Profile Code Software Instruction Manual*. Implant Sciences Corporation, 107 Audubon Road, No. 5, Wakefield, Massachusetts 01880, 3.20 edition.

[103] Sorab K. Ghandhi. *VLSI Fabrication Principles, Silicon and Gallium Arsenide*. John Wiley and Sons, INC., New York, NY 10158-0012, second edition, 1994.

[104] N. Hatzopoulos, D. I. Siapkas, P. L. F. Hemment, and W. Skorupa. *Journal of Applied Physics*, 80:4960–4970, 1996.

[105] Y. Ma, T. Yasuda, and G. Lucovsky. *Applied Physics Letters*, 64(17):2226–2228, 1994.

[106] S. V. Hattangady, H. Niimi, and G. Lucovsky. *J. Vac. Sci. Technol. A*, 14(6):3017–3023, 1996.

[107] V. A. C. Haanappel, H. D. Van Corbach, T. Fransen, and P. J. Gelings. *Materials Science and Engineering*, A167:179–185, 1993.

[108] V. V. Afanas'ev, A. Stesmans, A. G. Revesz, and H. L. Hughes. *Journal of Applied Physics*, 82(5):2184–2199, 1997.

[109] C. Vautey, M. Burgos, and M. Langlet. *Thin Solid Films*, 347:184–194, 1999.

[110] S. D. Kovaleski, R. M. Gilgenbach, L. K. Ang, and Y. Y. Lau. *Journal of Applied Physics*, 86:7129–7138, 1999.

[111] E. N. Glezer and E. Mazu. *Applied Physics Letters*, 71:882, 1997.

[112] P. Baeri, R. Reitano, and N. Marino. *Applied Surface Science*, 86:128–133, 1995.

[113] Sang Woo Lim, Yukihiro Shimogaki, Yoshiaki Nakano, Kunio Tada, and Hiroshi Komiyama. *Applied Physics Letters*, 68(6):832–834, 1996.

[114] L. Wu and D. M. Manos. *Materials Research Society Symposium Proceedings-Materials Development for Direct Write Technologies*, 624, 2000.

[115] K. Suzuki, K Konishi, K. Nakamura, and H. Sugai. *Plasma Source Science and Technology*, 9(2):199–204, 2000.

[116] L. Wu, B. C. Holloway, D. Prasad Beesabathina, C. Kalil, and D. M. Manos. *Surface and Coatings Technology*, 130:207–217, 2000.

[117] R. Gunzel, M. Betzl, I. Alphonsa, B. Ganguly, P. I. John, and S. Mukherjee. *Surface and Coatings Technology*, 112:307–309, 1999.

[118] C. Blawert and B. L. Mordike. *Surface and Coatings Technology*, 116-119:352–360, 1999.

[119] Z. M. Zeng, T. Zhang, B. Y. Tang, X. B. Tian, and P. K. Chu. *Surface and Coatings Technology*, 115:234–238, 1999.

[120] W. Wang, J. H. Booske, H. L. Liu, S. S. Gearhart, and J. L. Shohet. *Journal of Materials Research*, 13(3):726–730, 1998.

[121] J. P. Blanchard. *Journal of Vacuum Science and Technology*, 12(2):910–917, 1994.

[122] J. P. Holman. *Heat Transfer*. McGraw-Hill Book Company, New York, 1986.

[123] Saul Dushman. *Scientific Foundation of Vacuum Technique*. John Wiley and Sons, Inc., New York, 1962.

[124] David H. Holkeboer, Donald W. Jones, Frank Pagano, and Donald J. Santeler. *Vacuum Technology and Space Simulation*. American Institute of Physics, 335 East 45th Street, New York, NY 10017-3483, 1993.

[125] B. Larisch, U. Brusky, and H. J Spies. *Surface and Coatings Technology*, 116-119:205–211, 1999.

[126] A. R. Krauss D. M. Gruen A. Jayatissa S. Bhattacharya J. Tucek. A. Sumant T. D. Corrigan, O. Auciello and R. P. H. Chang. *Materials Research Society Symposium Proceedings - Electron-Emissive Materials and Vacuum Microelectronics*, 621, 2000.

Vita

Lingling Wu

Lingling was born in Pingwu, Sichuan Province, China on Oct. 27, 1970. She went to Beijing University to study in Electronics Department in Sept 1986 and received her bachelor's degree in Electronics and Information System in July 1990. She also received her first master's degree from Beijing University, in July 1993, in Surface and Thin Films Physics. She entered the Applied Science Department of the College of William and Mary in Virginia in August 1994 and received her second master's degree in science in 1996. Lingling will continue her research in the Physics Division of Candescent Technologies Corporation in San Jose, California, where she will work on a novel field emission based fiat panel display.